NOISE SUPPRESSION USING PRECONDITIONED LEAST-SQUARES PRESTACK TIME MIGRATION AND IMAGING OF MISSISSIPPIAN LIMESTONE

A THESIS

SUBMITTED TO THE GRADUATE FACULTY

in partial fulfillment of the requirements for the

Degree of

MASTER OF SCIENCE

By

SHIGUANG GUO
Norman, Oklahoma
2012
UNIVERSITY OF OKLAHOMA
GRADUATE COLLEGE

NOISE SUPPRESSION USING PRECONDITIONED LEAST-SQUARES PRESTACK TIME MIGRATION AND IMAGING OF MISSISSIPPIAN LIMESTONE

A THESIS APPROVED FOR THE
CONOCOPHILLIPS SCHOOL OF GEOLOGY AND GEOPHYSICS

BY

Dr. Kurt J. Marfurt, Chair

Dr. G. Randy Keller

Dr. J. Timothy Kwiatkowski

Acknowledgement

First, I would like to give my sincere thanks to my advisor Dr. Kurt J. Marfurt, for his guidance during my graduate study, it’s him that gave me so much encouragement to stretch my potential, and whenever there were difficulties, there he was ready to help. Also, his insight of geophysics enabled me to develop innovative problem solving ideas.

I want to extend my gratitude to my committee member Dr. Randy Keller and Dr. J. Tim Kwiatkowski. Thanks for their comments and suggestions for my graduate research. Whenever I have questions, they are kind to help. I particularly thank Dr. J. Tim Kwiatkowski’s guidance in extending my programming ability.

I also would like to thank my friends on our AASPI team. My work is built on earlier work by Alejandro Cabrales, who provided me many ideas on how to further my research. In addition, I appreciate the help from Dr. Kui Zhang, Bo Zhang and Yanxia Guo. Dr. Kui Zhang not only helped me with studies, but also with adapting to life in America along with our fellow student and his wife Yanxia Guo. Whenever I have problems, Bo Zhang is the one who is there to help me find the solution.

Table of Contents

List of Figures

iterations of CLSM, and (d) three iterations of CLSM. White block arrows indicate aliasing artifacts in (a) and (b). These artifacts are significantly attenuated in (c) and (d).

Figure 4.3. Change of residue as iterations increase for (a) unpreconditioned and (b) preconditioned least-squares migration for the decimated Dickman dataset. Change of gradient with increasing iteration for the decimated Dickman dataset (c) unpreconditioned, and (d) preconditioned LSM. The initial, preconditioned solution converges faster (smaller value of $|\mathbf{r}|$), but then levels out. Without constraints, aliases that appear in the subsurface image provide a better fit to the surface data, regardless as to whether that component of the data is signal or noise.

Figure 4.4. (a) Time-structure map of the top of the Gilmore City horizon, (b) source and receiver pair map, (c) the vertical slice through the line AA'. White arrows show collapse features, red arrow shows noise.

Figure 4.5. Vertical slice through seismic amplitude along profiles AA' as shown in Figure 4.4a: (a) using conventional migration, and after (b) two, and (c) three iteration of CLSM. (d) Vertical slice through noise difference amplitude between the original modeled data $\boldsymbol{m_1}$ and structure-oriented filtered model $\widetilde{\boldsymbol{m}}_{\boldsymbol{1}}$ along profiles AA'. The red block arrows in (a) indicate noise. White block arrows indicate the collapse features.

Figure 4.6. Vertical slice through seismic amplitude along profiles BB' as shown in Figure 4.4a: (a) using conventional migration, and after (b) two, and (c) three iteration of CLSM. Red block arrows indicate the fault. After CLSM, the fault is better imaged.

Figure 4.7. Time slice at t=0.406s through stacked amplitude volumes after (a) conventional migration and after (b) two, and (c) three iterations of CLSM. The white

block arrow in (a) indicates footprint, which impedes interpretation. CLSM attenuates these footprint artifacts after (b) two, and (c) three iterations.

Figure 4.8. Horizon slices along the Gilmore City through coherence volumes computed from seismic amplitude: (a) using conventional migration, and (b) two, and (c) three iterations of CLSM. Red block arrows indicate the karst collapse features.

Figure 4.9. Horizon slices along the Gilmore City through inline gradient co-rendered with the coherent energy volumes computed from seismic amplitude: (a) using conventional migration, and (b) two and (c) three iterations of CLSM. The white block arrows in (c) indicate the collapse features.

Figure 4.10. Horizon slices along the Gilmore City through K2 curvature volume computed from seismic amplitude: (a) using conventional migration, and (b) two and (c) three iterations of CLSM. The white block arrows in (b), (c) indicate the collapse features.

Figure 4.11. Representative traces from seismic shot gathers: (a) Original data which was input to both conventional and the first iteration of CLSM migration. (b) Predicted (demigrated) gathers after (b) conventional migration, (c) one, (d) two, and (e) three iterations of CLSM. Note the scale bar for the demigrated conventional gathers are different from the original input data. In contrast, CLSM better approximates the original data, allowing us to construct the residual $\mathbf{r}$ at each iteration. Random noise in the demigrated image of the conventionally migrated data indicates that such noise has leaked into the subsurface image. In contrast, the demigrated reflectors become increasingly coherent with the number of iterations in CLSM (white block arrows), indicating that only signal (or noise consistent with signal) remains in the subsurface images, $\mathbf{m_n}$.

List of Symbols

The seismic migration literature now has a 50 years history, using many different notations. The table below summarizes the notation used in this thesis:

Symbols	meaning
$\mathbf{m}$	migrated CRP gathers
$\mathbf{q}$	midpoint vector between source and receiver
t	two way travel time
$\mathbf{w}$	migration weight
$\mathbf{o}$	offset vector
$\mathbf{d}$	seismic data vector
Ω	migration aperture
Q	demigration aperture
ξ	The (x,y,z) coordinate information
$\mathbf{L}$	forward modeling operator (prestack Kirchhoff time demigration)
$\mathbf{L}^{T}$	adjoint operator (prestack Kirchhoff time migration)
ε	misfit function
$\mathbf{r}$	residual vector
$\mathbf{g}$	gradient vector
$\mathbf{h}$	conjugate direction vector
α	weighting coefficient
β	weighting coefficient
$\boldsymbol{u}$	a specific trace within the migration analysis window
$\mathbf{XY}_{\xi}$	the horizontal projection of the image-coordinates vector

Abstract

Conventional Kirchhoff migration often suffers from artifacts such as aliasing and acquisition footprint, which come from sub-optimal seismic acquisition. The footprint can masks faults and fractures, while aliased noise can focus into false coherent events which affect interpretation and contaminate AVO, AVAz and elastic inversion. Preconditioned least-squares migration minimizes these artifacts.

I implement least-squares migration by minimizing the difference between the original data and the modeled demigrated data using an iterative conjugate gradient scheme. Unpreconditioned least-squares migration better estimates the subsurface amplitude, but doesn't suppressing aliasing. In this thesis, I precondition the results by applying a 3D prestack structure-oriented LUM filter to each common offset and common azimuth gather at each iteration. The preconditioning algorithm not only suppresses aliasing of both signal and noise, but also improves the convergence rate.

I apply the new preconditioned least-squares migration to two surveys acquired over a new resource play in the Mid-Continent, USA. Acquisition footprint in shallow targets is attenuated and the signal to noise ratio is enhanced. To demonstrate the impact on interpretation, I generate a suite of seismic attributes to image the Mississippian limestone, and show that karst-enhanced fractures in the Mississippian limestone can be better illuminated.

Motivation

Aliasing comes from the incomplete spatial sampling of the surface seismic wave field and often presents major problems in seismic interpretation. For reasons of efficiency, almost all land seismic data are acquired on a regular grid, which is “rolled along” as the survey progresses. In this situation, the aliasing is no longer random but becomes organized into acquisition footprint. Footprint can mask faults and fracture and contaminate AVO, AVAz, and elastic inversion analysis. Geometric attributes enhance footprint artifacts. When acquisition obstacles are encountered, the change from regular to irregular surface coverage gives rise to migration ellipses, which “swing in” to fill the gap.

Post stack seismic attributes can enhance subtle geological features. Curvature and coherence are routinely used to delineate fractures and faults, while spectral decomposition illuminates channels, fans, and stratigraphic features. Seismic attributes often enhance subtle geological features such as fractures, karst, and tripolite sweet spots in the Mississippian limestone. Seismic attributes also “enhance” the appearance of acquisition footprint (Figure 0.1). Falconer and Marfurt (2008) used this ‘negative’ feature of geometric attributes as a means of characterizing short-wavelength footprint components on migrated data after stack. The goal of this thesis is to use constrained least-squares migration to suppress such artifacts and thereby improve the interpretation on prestack migrated gathers.

The Mississippian limestone is one of the most recent resource plays made economical by horizontal drilling and hydraulic fracturing. Natural fractures provide conduits for hydrocarbon and fluid movement. Diagenetically-altered chert (tripolite) provides sweet spots for production. Karst features in the deeper Cambro-Ordovician Arbuckle Limestone provide excellent well locations needed to deposit the large volumes (up to 95%) of water produced. Since the targets in the two surveys are shallow (< 5000 ft), acquisition footprint is particularly strong. I use constrained least-squares migration to suppress artifacts and improve lateral resolution of the underlying geology.

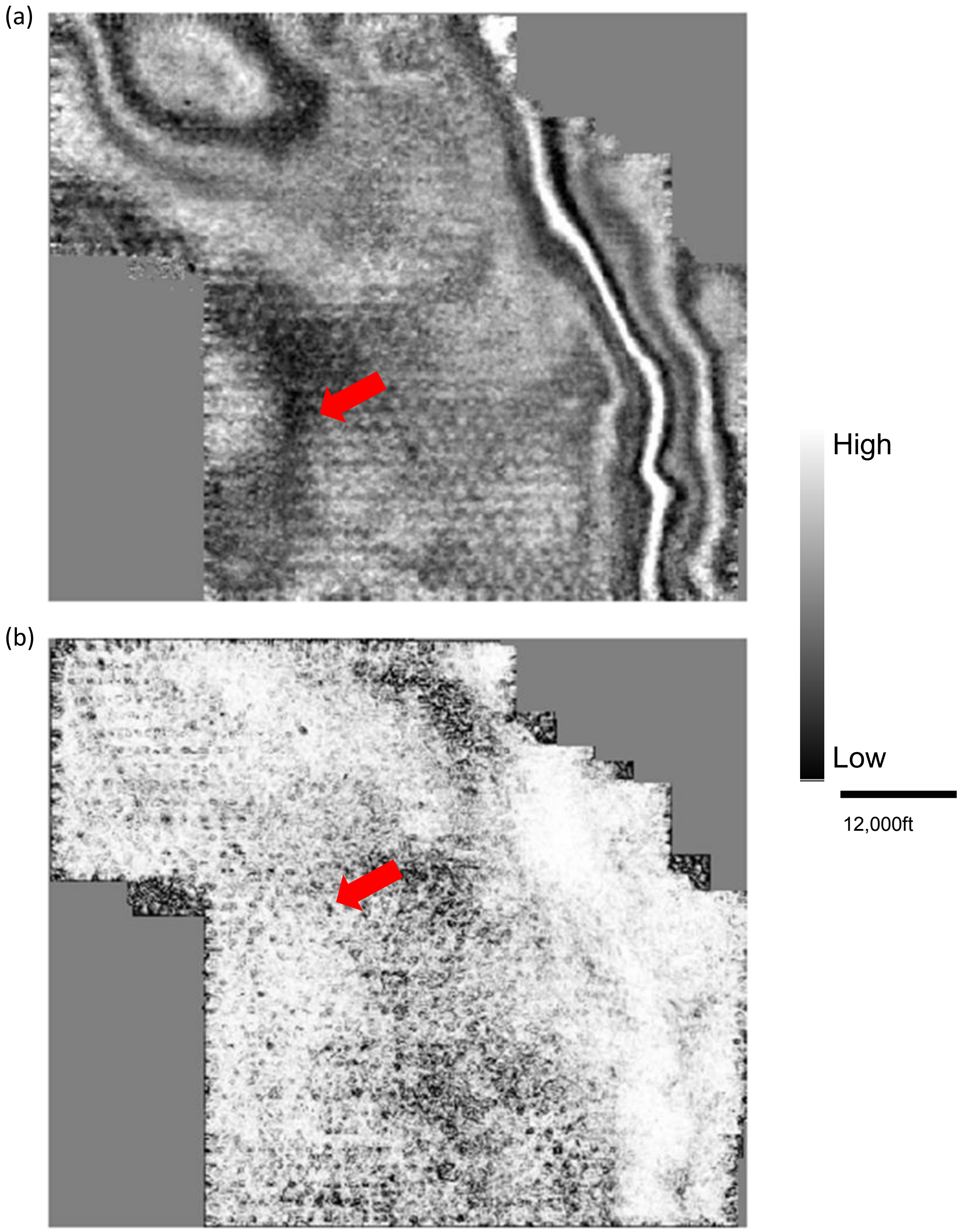

Figure 0.1. (a) Time slice at 500ms through seismic amplitude and (b) coherence volumes from a survey acquired through from Central Basin Platform. Acquisition footprint gives rise to a regular grid of circular artifacts on the coherence image that masks circular to elliptical anomalies associated with karst features at this time level. (After Falconer and Marfurt, 2008).

Chapter 1

Introduction

Prestack Kirchhoff time migration is still the most popular migration algorithm due to its high efficiency and flexibility, especially in imaging relatively flat-lying faulted and fractured plays in the Mid-Continent of the USA. Unfortunately, suboptimal surface seismic acquisition patterns usually give rise to both data and migration operator aliasing and footprint, both of which hinder subsequent interpretation. The most common means of suppressing aliasing is to apply an antialias filter within the migration algorithm (Figure 1.1). While such a filter removes the aliasing overprint, it also reduces the high-frequency content of more steeply dipping events, including lateral discontinuities. One of the goals of PLSM is to suppress aliasing yet retain the full frequency bandwidth in the resulting image.

Conventional Kirchhoff migration can be regarded as the adjoint of the seismic forward modeling operator (Claerbout, 1992). Chavent and Plessix (1996) used standard migration as the zeroth iteration, and then used a conjugate gradient scheme to compute the Hessian matrix. They then used a least-squares formulation to obtain an optimized image. Schuster (1993) added constraints to the objective function. Following Nemeth (1996), he used least-squares migration to overcome uncompensated migration artifacts due to incomplete data, which can give rise to acquisition footprint.

Least-squares migration may require many iterations to reach convergence, consuming significant computer resources. For this reason, significant effort has focused on preconditioning the input data to decrease the number of iterations. Wei and Schuster

(2009) and Aoki and Schuster (2009) preconditioned the data by using a deblurring filter, thereby reducing the number of iterations needed. Wang and Sacchi (2009) evaluated running average and prediction filter constraints to improve the convergence rate of a 2D least-squares migration algorithm. Cabrales Vargas (2011) used mean and median filters as constraints in 3D constrained least-squares migration in his master thesis.

Post-stack structure-oriented filtering is commonly used in conditioning stacked volumes after migration to facilitate interpretation (Fehmers and Höecker, 2003). Luo et al. (2002) extended Kuwahara et al. (1976) algorithm to 3D seismic data as an alternative edge-preserving smoothing algorithm. Marfurt (2006) proposed a modification of Luo et al.'s (2002) technique. First, he used coherence rather than the standard deviation to choose the most homogeneous window. Then, instead of using the mean, median or the α-trimmed mean, he used a principal component (or Karhunen-Loeve) filter to that more fully uses trends in the analysis window to replace the amplitude at the analysis point. Corrao et al. (2011) showed how an LUM-based structure-oriented filter can reject outliers, yet better retain the original character of the seismic data. Kwiatkowski and Marfurt (2011) showed how such filters can be applied to prestack time-migrated common-offset-azimuth gathers. To suppress aliasing within the conjugate gradient PLSM algorithm, I apply structure-oriented filters to the common-offset-azimuth gathers, which reduces the number of iterations needed by PLSM.

In this thesis, I begin my discussion by a review of Kirchhoff migration and demigration. Specifically, I examine the role of Kirchhoff migration as the adjoint of the seismic modeling operator and demigration as the seismic modeling operator in a PLSM algorithm. Next, I will introduce the mathematics of the PLSM algorithm, and its solution using the conjugate gradient method. Then, I show how Kwiatkowski and Marfurt's (2011) prestack structure-oriented filter serves as constraint that increases PLSM convergence. I demonstrate the value of my PLSM algorithm and workflow to two prestack Mississippian Lime data volumes –from Ness Co., KS and Osage Co., OK and illustrate the effectiveness by analyzing seismic attributes computed along the Gilmore City and Mississippian Chert horizons. I conclude with a summary of computational advantages and disadvantages of PLSM.

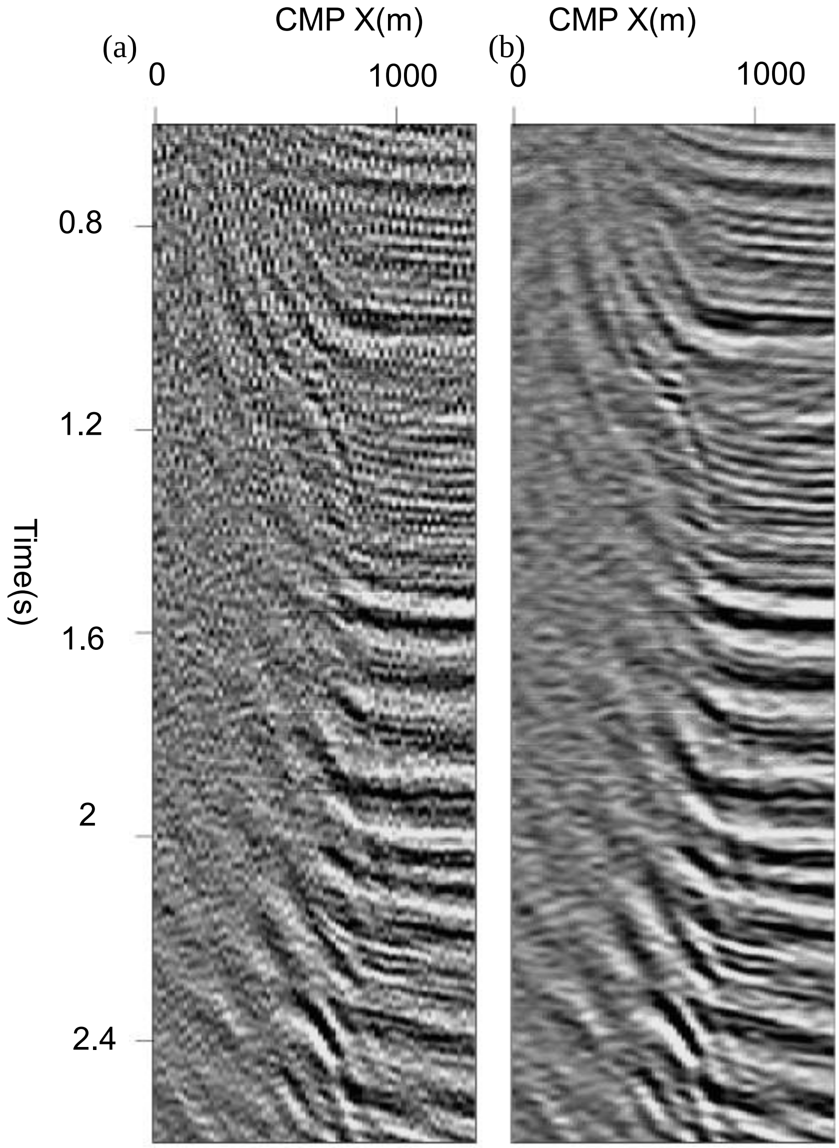

Figure 1.1. (3-D) migration of salt-dome flanks in the Gulf of Mexico obtained (a) without and (b) with the application of an antialiasing filter that limits the frequency of steeply dipping events. (After Biondi, 2001).

Chapter 2

Kirchhoff migration and demigration

2.1 Kirchhoff migration

Kirchhoff migration is the adjoint operator of Kirchhoff modeling (Nemeth et al., 1999). Biondi (2006) represents prestack 3D Kirchhoff migration using Green's function

$$\mathbf{m}(\xi) = \int_{\Omega_\xi} W(\xi, \mathbf{q}, \mathbf{h}) \frac{\partial}{\mathrm{d}t} d[t = t_D(\xi, \mathbf{q}, \mathbf{o}), \mathbf{q}, \mathbf{o}] \mathrm{d}\mathbf{q}\mathrm{d}\mathbf{o}, \tag{2-1}$$

where $\mathbf{m}(\xi)$ are the migrated CRP gathers,

$\mathbf{d}(t, \mathbf{q}, \mathbf{o})$ are the surface seismic data,

$\mathbf{W}(\xi, \mathbf{q}, \mathbf{o})$ is the weighing function,

$\frac{\partial}{dt}$ represents the first time derivative,

Ω_ξ is the migration aperture,

$\mathbf{q}$ is the midpoint vector, and

o is the offset position vector.

Equation 2-1 migrates $d(t, \mathbf{q}, \mathbf{o})$ when the midpoint, $\mathbf{q}$, falls in the migration aperture Ω_ξ. $t_D(\xi, \mathbf{q}, \mathbf{o})$ is the time that the reflection travels from the source position to image position,t_s, plus the time from the image point back to the receiver, t_g:

$$t_D = t_s + t_g = \sqrt{\frac{Z_\xi^2 + |\mathbf{XY}_\xi - \mathbf{q} + \mathbf{o}|^2}{V}} + \sqrt{\frac{Z_\xi^2 + |\mathbf{XY}_\xi - \mathbf{q} - \mathbf{o}|^2}{V}}. \tag{2-2}$$

where $\mathbf{XY}_\xi$ represents the horizontal projection of the image-coordinate vector, and v is the migration velocity.

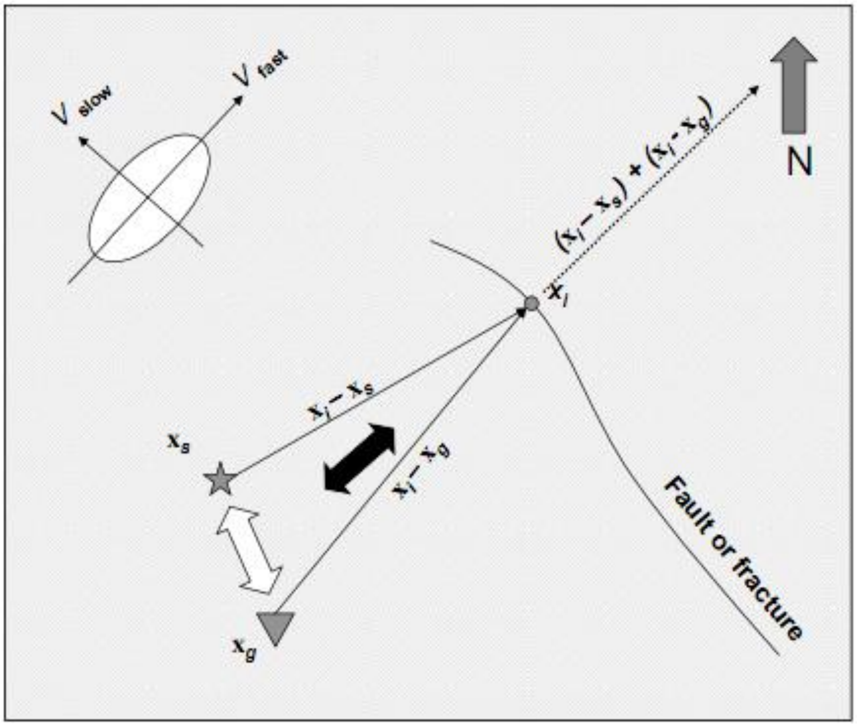

Figure 2.1. New azimuthal binning (after Perez and Marfurt, 2008).

Perez and Marfurt (2008) proposed a new azimuthal binning approach to Kirchhoff prestack migration that sorts output by the azimuth of the average travel path from surface midpoint to subsurface image point, rather than the azimuth between source and receiver (Figure 2.1). This new binning allows us to identify the image contribution from out-of-the-plane steeply dipping reflectors, fractures, and faults. I will use this algorithm as my migration operator. For ‘conventional migration’, I will leave the antialias operator ‘on’. For PLSM, I will remove the antialias operator and instead use the constraints to reduce aliasing after the first iteration.

2.2 Kirchhoff demigration

Demigration is the adjoint of migration, and constitutes the modeling operator during least-squares migration (Zhang, et al 2002; Biondi, 2006)

$$\mathbf{D}(t,\mathbf{q},\mathbf{o}) = \int_Q W(\xi,\mathbf{q},\mathbf{o})\frac{\partial}{\mathrm{d}t}\mathbf{m}(t_\xi,\mathbf{x}_\xi,\mathbf{y}_\xi)\mathrm{d}\mathbf{x}\mathrm{d}\mathbf{y}, \tag{2-3}$$

where

$\mathbf{D}(\mathbf{t},\mathbf{q},\mathbf{o})$ denotes the 3D modeled common-shot gathers,

$\mathbf{m}(x_\xi,y_\xi,z_\xi)$ are the 3D migrated common-reflection point gathers,

$(\mathrm{x}_\xi,\mathrm{y}_\xi)$ represents the horizontal projection of the image point,

$\mathbf{W}(\xi,\mathbf{q},\mathbf{o})$ are the demigration weights,

$\frac{\partial}{dt}$ is the time derivative applied to the migrated common-reflection point gathers, and

Q denotes the demigration aperture.

t_ξ is the total time the reflection travels from the source position to image position, plus the time from the image point back to the receiver:

$$t_\xi = t_s + t_g = \sqrt{\frac{Z_\xi^2+|\mathbf{XY}_\xi-\mathbf{q}+\mathbf{o}|^2}{V}}+\sqrt{\frac{Z_\xi^2+|\mathbf{XY}_\xi-\mathbf{q}-\mathbf{o}|^2}{V}}. \tag{2-4}$$

The demigration program I developed in thesis is based on the Kirchhoff prestack migration, and it constitutes the forward modeling operator used in the least-squares migration workflow described below.

Chapter 3

Preconditioned least-squares migration

3.1 Least-squares migration

I can express modeling (demigration) in matrix notation as:

$$\mathbf{d} = \mathbf{L}\mathbf{m}, \tag{3-1}$$

where **L** constitutes the forward modeling operator (in this thesis prestack time demigration),

m is the reflectivity model, and

d is the modeled data.

I define migration as

$$\mathbf{m}' = \mathbf{L}^{\mathrm{T}}\mathbf{d}, \tag{3-2}$$

where

$\mathbf{L}^{\mathrm{T}}$ is the adjoint operator of **L**, (in this thesis is prestack time migration), and

$\mathbf{m}'$ is the migration approximation to the Earth's reflectivity.

Standard migration $\mathbf{L}^{\mathrm{T}}$ is the adjoint of the forward modeling operator **L**.

Substituting equation 3-1 into equation 3-2, I obtain

$$\mathbf{m}' = \mathbf{L}^{\mathrm{T}}\mathbf{L}\mathbf{m}. \tag{3-3}$$

I can regard the matrix $\mathbf{L}^{\mathbf{T}}\mathbf{L}$ as a linear filter applied to **m**. If $\mathbf{L}^{\mathbf{T}}\mathbf{L}$ approximates the identity matrix, the migration $\mathbf{m}'$ will be a scaled version of the reflectivity $\mathbf{m}$.

Unfortunately, due to sparse surface acquisition, $\mathbf{L^T L}$ is almost never diagonal such that $\mathbf{m}'$ has migration artifacts (Nemeth, 1996).

Schuster (1997) attenuated these artifacts by making $\mathbf{L^T L}$ closer to the identity matrix. In this thesis, I add constraints to obtain:

$$\varepsilon = \left|\left|\mathbf{Lm} - \mathbf{d}\right|\right|^{\mathbf{2}} + ||\mathbf{Cm}||^{\mathbf{2}}, \tag{3-4}$$

where ε is the objective function to be minimized, the first term on the right-hand side of the equation is the misfit function, and **C** is the constraint matrix. Multiplying both sides of equation 3-4 by $\mathbf{L^T}$, the model **m** that minimizes equation 3-4 can be found by a gradient type optimization method (Wei and Schuster, 2011).

$$\mathbf{m_{n+1}} = \mathbf{m_n} - \alpha\mathbf{F}(\mathbf{L^T}(\mathbf{Lm_n} - \mathbf{d}) + \mathbf{Cm_n}) \tag{3-5}$$

where $\mathbf{L^T}(\mathbf{Lm_n} - \mathbf{d}) + \mathbf{Cm_n}$ is the gradient, F is a preconditioning matrix, here I use prestack structural-oriented filter, α is the step length. I will solve equation 3-5 for **m** using a conjugate gradient scheme, giving rise to an iterative method constitutes preconditioned least-squares migration algorithm (Schuster, 1997).

3.2 The conjugate gradient method

The conjugate gradient method is perhaps the most popular iterative algorithm for solving sparse systems of linear equations.

First, initialize the model **m** to be 0:

$$\mathbf{m_0} = 0, \tag{3-7}$$

Next, compute the residual vector $\mathbf{r_0}$ associated with the model $\mathbf{m_0}$:

$$\mathbf{r_0} = \mathbf{d_0} - \mathbf{Lm_0}, \tag{3-8}$$

where $\mathbf{d_0}$ represent the original data. Since $\mathbf{m}_0 = 0$, I obtain:

$$\mathbf{r_0} = \mathbf{d_0}, \tag{3-9}$$

The residual vector $\mathbf{r_0}$ constitutes the initial search direction, allowing me to compute the zeroth iteration gradient vector:

$$\mathbf{g_0} = \mathbf{L^T r_0}, \tag{3-10}$$

where $\mathbf{g_0}$ can be regarded as the conventional (unconditional, non-least-squares) migration result, and defines the search direction of the first $n = 1$ iteration in the conjugate gradient scheme. Following Jovanovic (2004), I create a set of orthogonal conjugate direction vectors $\mathbf{h_n}$,

$$\mathbf{h_n} = \mathbf{g_n} + \textstyle\sum_{k=0}^{n-1} \beta_k \mathbf{h_k}, \tag{3-11}$$

where β_k is the k^{th} weighting coefficient. For the $n = 0$ iteration, $\mathbf{h_0}$ is identical to $\mathbf{g_0}$, resulting in an updated model vector $\mathbf{m}_{\boldsymbol{n+1}}$:

$$\mathbf{m_{n+1}} = \mathbf{m_n} + \alpha_n \mathbf{h_n}, \tag{3-12}$$

Where α_n is the weighting coefficient at the n^{th} iteration. Next, I update the residual (direction) vector $\mathbf{r_{n+1}}$ and gradient $\mathbf{g_{n+1}}$:

$$\mathbf{r_{n+1}} = \mathbf{r_n} - \alpha_n \mathbf{Lh_n}, \text{ and} \tag{3-13}$$

$$\mathbf{g_{n+1}} = \mathbf{L^T r_{n+1}}. \tag{3-14}$$

Since $\mathbf{L^T}$ is the migration, the gradient vector $\mathbf{g_{n+1}}$ is the migration of the residual $\mathbf{r}_{\boldsymbol{n+1}}$.

I define the optimum values of the weighting coefficients α_n and β_n to be:

$$\alpha_n = \frac{\langle \mathbf{g_n}, \mathbf{g_n} \rangle}{\langle \mathbf{Lh_n}, \mathbf{Lh_n} \rangle}, \text{ and} \tag{3-15}$$

$$\beta_n = \frac{\langle \mathbf{g_{n+1}}, \mathbf{g_{n+1}} \rangle}{\langle \mathbf{g_n}, \mathbf{g_n} \rangle}, \tag{3-16}$$

where the notation <,> indicates the inner product. To enhance the specular reflection energy and attenuate the aliased noise, I will apply α-trim median filter along reflection dip to $\mathbf{m}$:

$$\widetilde{\boldsymbol{m}}_{\mathbf{n+1}} = \mathbf{F}(\mathbf{m_{n+1}}), \tag{3-17}$$

prior to updating **h**

$$\tilde{\mathbf{h}}_{\mathbf{n}} = \frac{\widetilde{\boldsymbol{m}}_{\mathbf{n+1}} - \mathbf{m_n}}{\boldsymbol{\alpha}_{\mathbf{n}}}. \tag{3-18}$$

Substituting the updated $\tilde{\mathbf{h}}_{\mathbf{n}}$ for $\mathbf{h_n}$ in equation 3-11 results in preconditioned least-squares migration. To obtain an accurate representation of Earth's reflectivity model, the conjugate gradient scheme needs to run a number of times, with the number of iterations depending on the convergence rate and the desired level of accuracy. In my applications, I will limit myself to no more than three iterations, which will provide the bulk of the image improvement.

3.3 Structure-oriented filtering

Structure-oriented filtering utilizes filters along local estimates of seismic of dip and azimuth. To remove random noise and enhance lateral continuity, popular filters include mean, median, α-trim mean, LUM, and principle component filters. Given the need to suppress strong, non-Gaussian aliased noise in least-squares migration, I will use the α-trim median filter to each common-offset gathers.

The α-trim mean filter

The first step in the α-trim mean filter is to first sort a suite of seismic samples in ascending order. Then, the lowest and highest α fraction of the data are trimmed away, or rejected. Finally, we compute the mean of the remaining 1-2α fraction of the data. Thus, a value of α =0.0 results in the conventional median filter. Ideally, rejection of α fraction of the largest and smallest data will reject strong positive and negative spikes, while the mean filter improves the statistics of the “better behaved” data that remain.

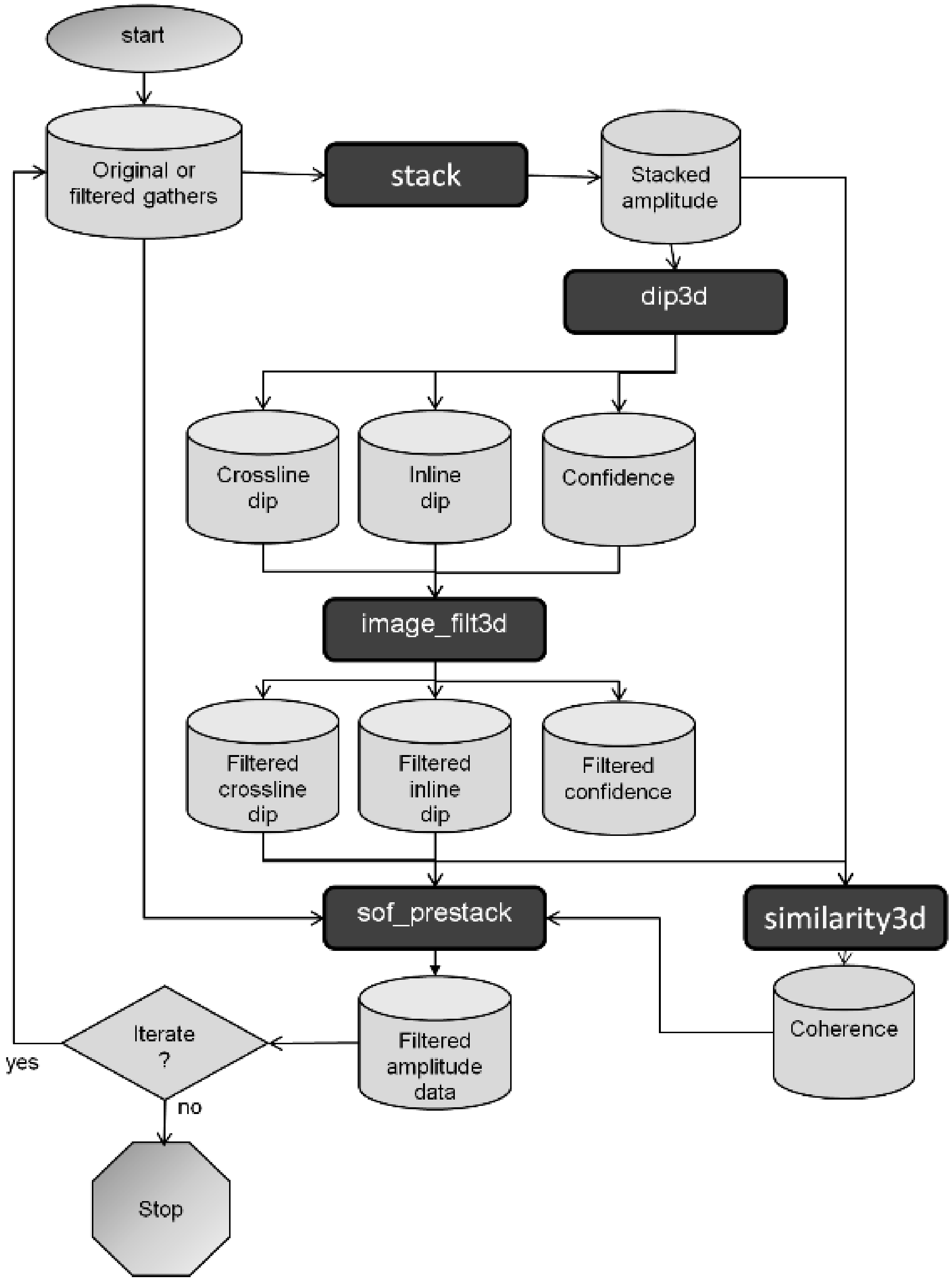

Figure 3.1. Prestack structure-oriented filtering workflow. (After Davogustto, 2011).

3.4 Algorithm description

My Preconditioned least-squares migration starts with prestack Kirchhoff time migration. The first prestack time migration constitutes the zeroth iteration, or $\mathbf{L}^{\mathbf{T}}\mathbf{d}_{\mathbf{0}}$ in equation 3-10. After the first migration, I set the first model $\mathbf{m}_{\mathbf{0}}$ to be zero, and obtain the migrated gather $\mathbf{g}_{\mathbf{0}}$ and $\mathbf{h}_{\mathbf{0}}$ as shown Figure 3-2.

After the initial migration (program **azim_offset_mig**), the program enters the preconditioned least-squares migration loop. The first step in the loop is to perform prestack demigration, which outputs $\mathbf{r}_{\mathbf{n}}$, $\mathbf{m}_{\mathbf{n}}$, and the updated $\mathbf{g}_{\mathbf{n}}$.

The constraints are applied to $\mathbf{m}_{\mathbf{n}}$, which is implemented using structure-oriented filtering (program **sof_prestack**). In our implementation at OU, structure-oriented filtering requires previously computed estimates of volumetric dip and azimuth (program **dip3d**). By using an α-trimmed mean filter, I am able to reject strong, cross-cutting noise associated with both data and operator aliasing. The result is a filtered version of the subsurface reflectivity model $\widetilde{\boldsymbol{m}}_{\boldsymbol{n}}$. Following equation 3-17 and equation 3-18, I calculate the updated search direction $\widetilde{\boldsymbol{h}}_{\boldsymbol{n}}$using the filtered $\widetilde{\boldsymbol{m}}_{\boldsymbol{n}}$.

The second migration will migrate the residua. The second and all subsequent migration will be run with the antialias filter (Biondi, 2000) turned off. When the iteration count, *n,* reaches the maximum number of iterations *N*, I end the loop, where the final value of $\mathbf{m}_{\mathbf{n}}$ represent the PLSM image.

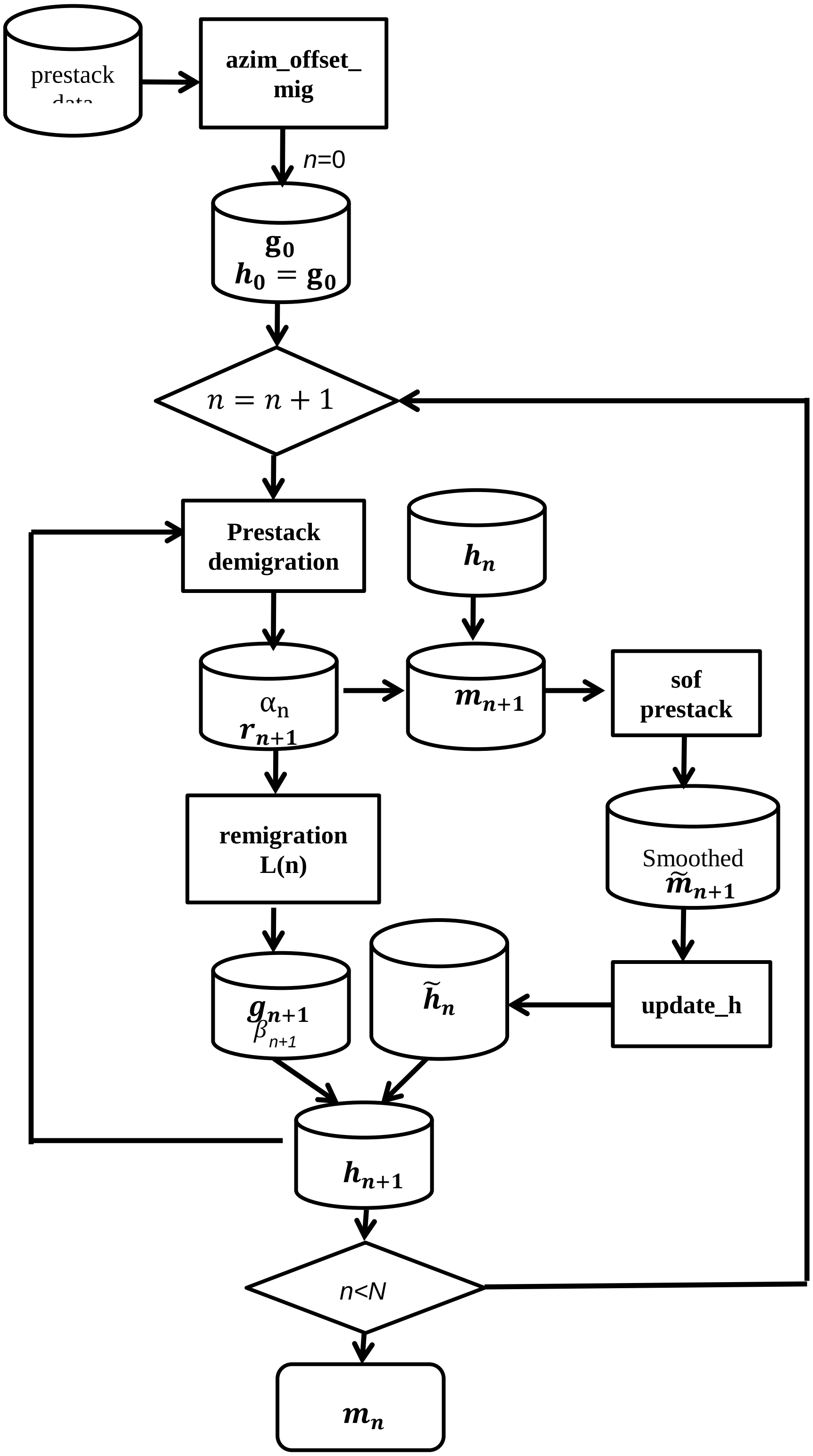

Figure 3.2. Here is workflow of PLSM. Some programs from the AASPI utilities, I will explain each in table 3-1.

Program Name	**Description (Programs I have written are in red)**
azim_offset_mig	AASPI prestack Kirchhoff time migration
prestack demigration	Prestack Kirchhoff time demigration
remigration	nth iteration (n>1) of prestack Kirchhoff time migration, that updates the gradient, **g**, based **azim_offset_mig**
dip3d	AASPI utility program, it can calculate the inline and crossline dip components
sof_prestack	AASPI_prestack utility, structure-oriented filter for prestack gathers
stack	AASPI utility stack the prestack gathers to post stack volume
update_h	The Program that updates conjugate direction vector **h**

Table 3.1. Component programs that together with shell scripts and graphical user interfaces, comprise my implementation of preconditioned least-squares migration. Pre-existing software at OU are in black, while routines I have written as part of this thesis are in red.

Chapter 4

PLSM of 3D data acquired over Dickman Field, Ness Co., KS

4.1 Field introduction

Dickman field, located in Northern County, Kansas, is a typical super mature Mississippian reservoir, which has produced approximately 1.7 million barrels of oil. In the field, Pennsylvanian strata unconformably overlie the Mississippian reservoir rocks of the Meramecian Spergen and Warsaw limestone. The Mississippian reservoir in Dickman field is composed of shallow-shelf carbonates. Karst-enhanced fractures have been documented to extend several meters below the regional unconformity surface. The Western Interior Plains aquifer system acts as a very strong bottom water drive for the reservoir, which in turn is underlain by the low porosity and low permeability Gilmore City limestone, which acts as a flow barrier.

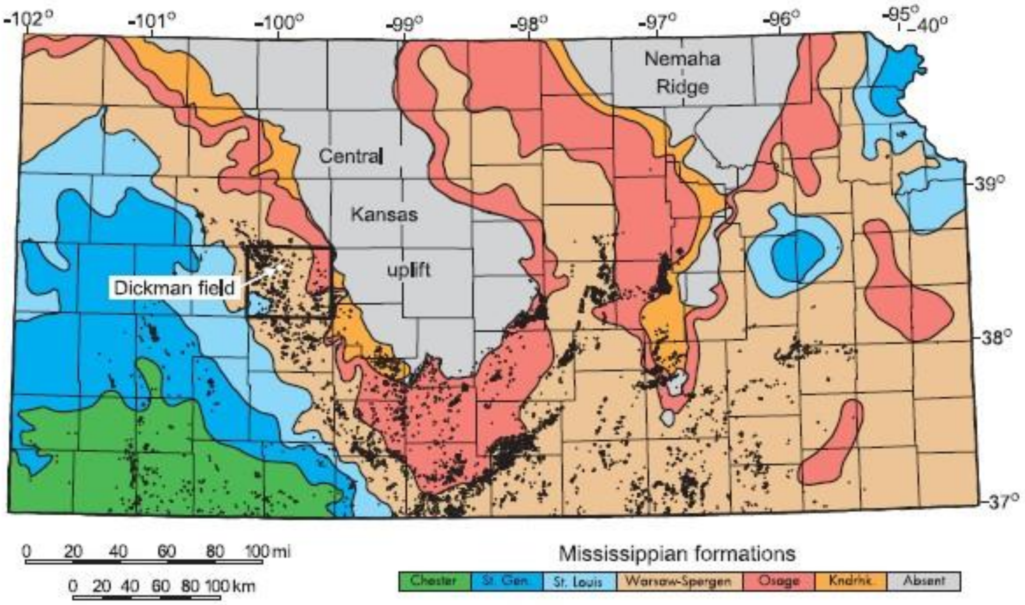

Figure 4.1. Map of the Mississippian subcrop in Kansas. Black box outlines Ness County, and the white block arrow indicates the location of Dickman Field. Black dots represent oil production. Colors represent different Mississipian-Age formations (After Nissen et al., 2009).

4.2 Application to a decimated dataset

Sparse sampling will give rise to aliasing artifacts in the stacked volume. To demonstrate the effectiveness of the preconditioned least-squares migration, I applied PLSM to the Dickman dataset after removing almost 80% of the data.

Figure 4.2a shows the stacked volume after conventional migration. The block white arrow indicates an aliasing artifact giving rise to a low signal-to-noise ratio. The stacked volume after one iteration of PLSM in Figure 4.2b is nearly identical in appearance to conventional migration in Figure 4.2a, since constraints have not yet been applied, with only differences in scale due to the scale factor α_n as described by equation 3-10 through 3-12. After two iterations of PLSM in Figure 4.2c, the stacked volume shows significant improvement, with aliasing artifact attenuated, and deeper reflectors exhibiting greater continuity. After three iterations (Figure 4.2d), the aliasing artifacts are removed and the data quality is sufficiently improved such that no further iterations are required.

Figures 4.3a and c show the change in the magnitude of the residue and gradient with increasing iteration for least-squares migration without constraints for the decimated Dickman dataset. Figures 4.3b and d show analogous figures for preconditioned least-squares migration. Note that the residue convergence performance of PLSM is better than LSM, but there is not much change in the gradient change as iterations increase.

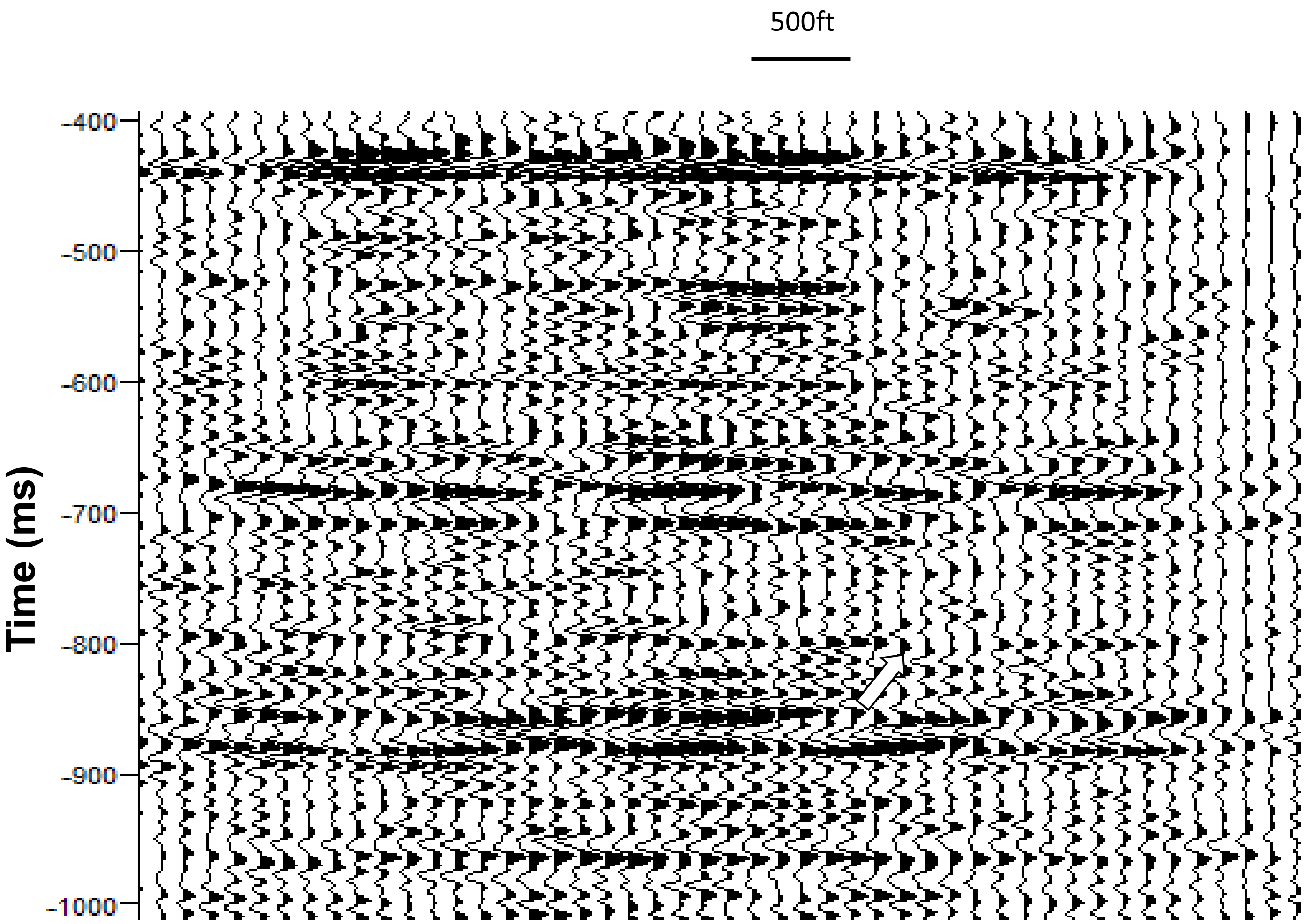

Figure 4.2. Vertical slice through stacked volume after prestack time migration of the decimated data using conventional migration of the decimated data. Constant gain of 1.5E6.

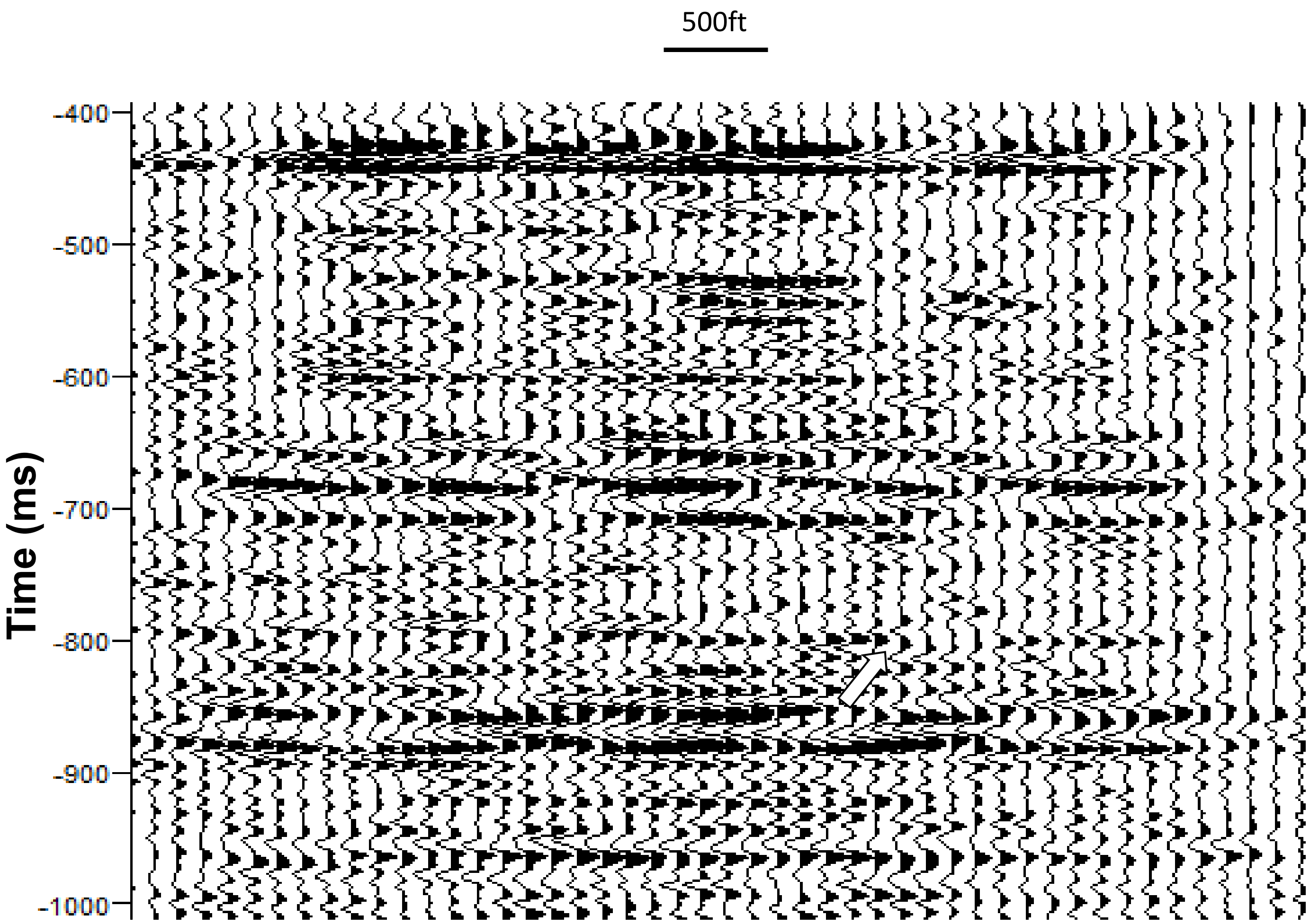

Figure 4.3. Vertical slice through stacked volume after prestack time migration of the decimated data after one iterations of PLSM of the decimated data. Constant gain of 1.5E8.

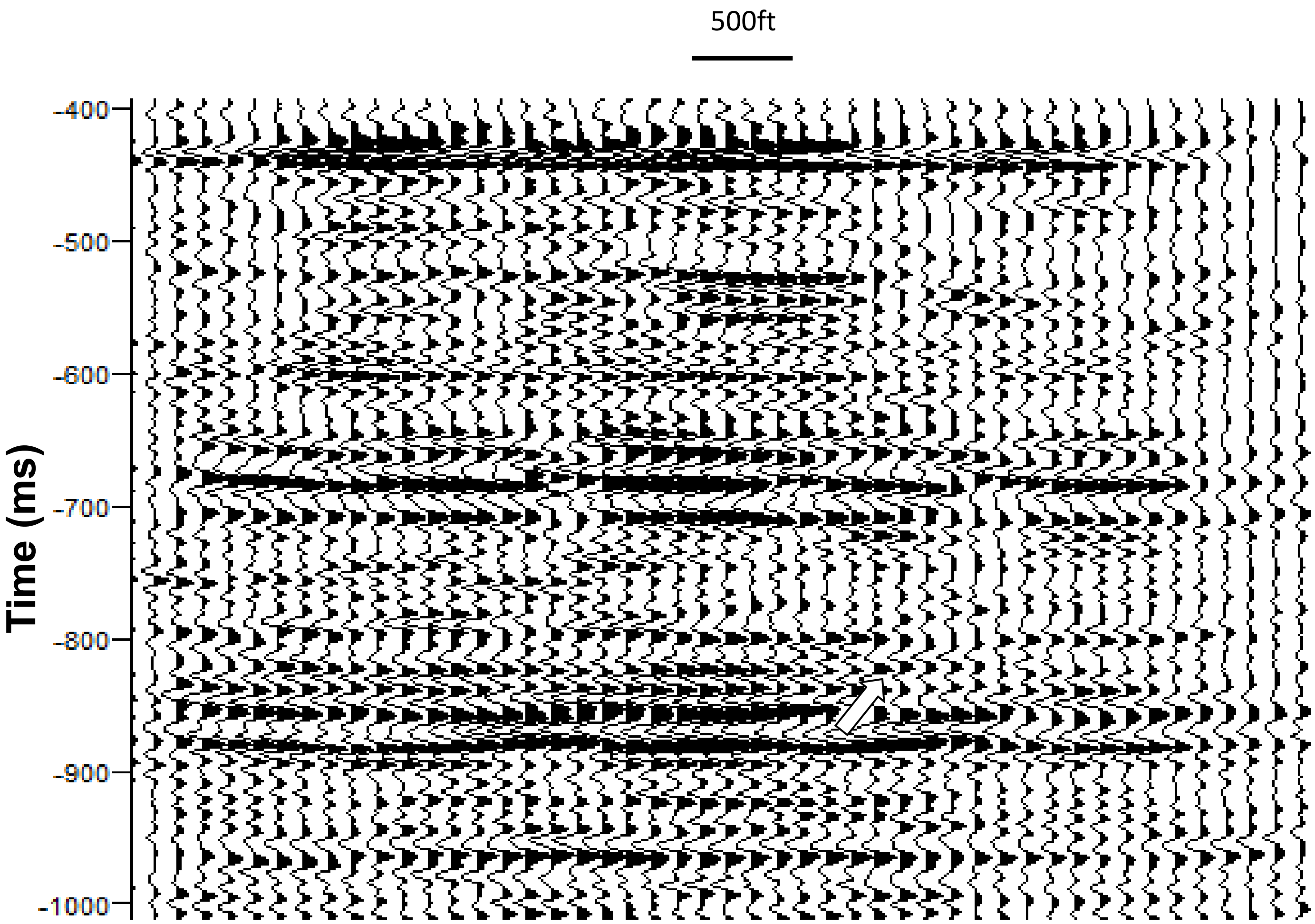

Figure 4.4. Vertical slice through stacked volume after prestack time migration of the decimated data after two iterations of PLSM of the decimated data. Constant gain of 1.5E8.

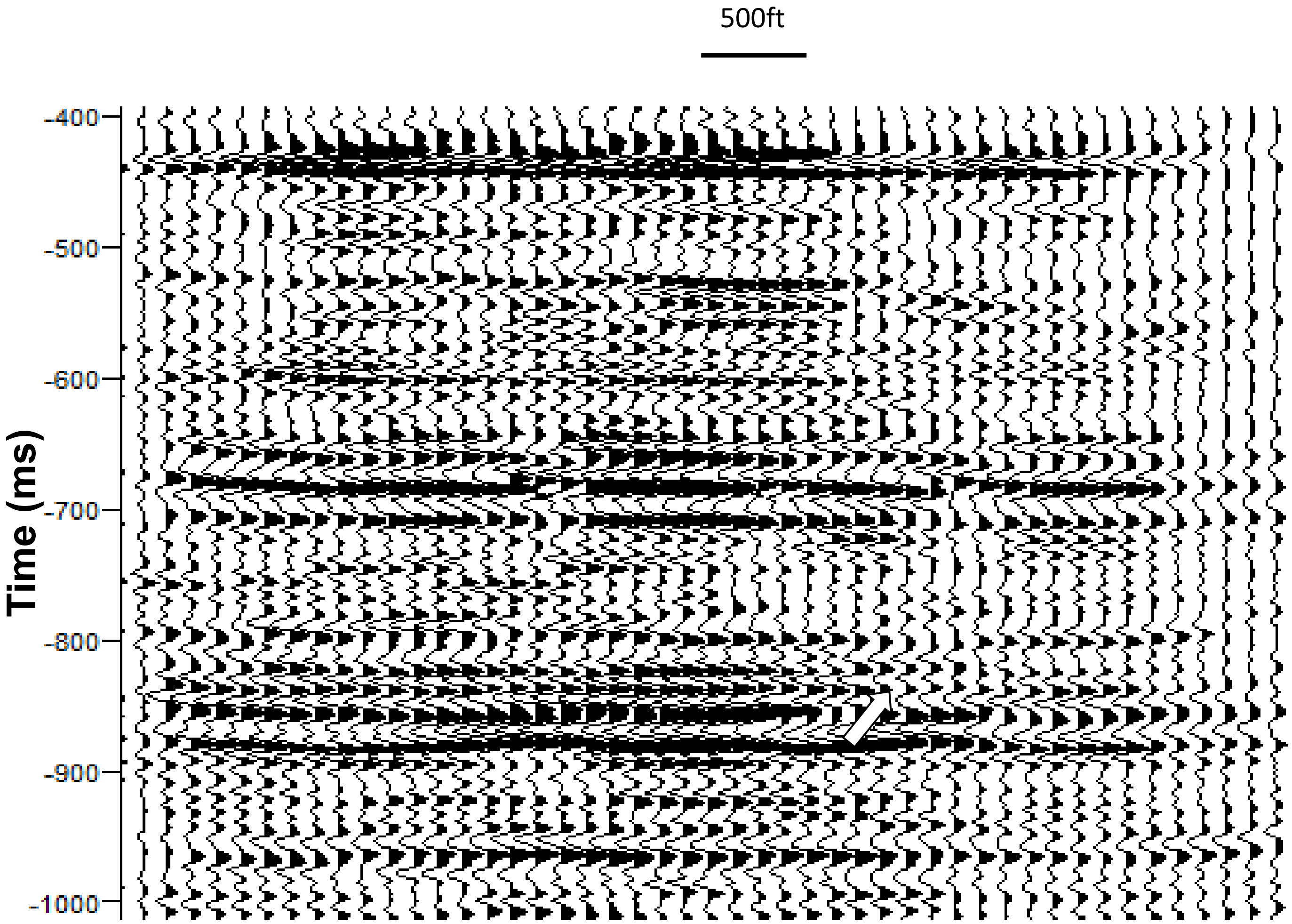

Figure 4.5. Vertical slice through stacked volume after prestack time migration of the decimated data after three iterations of PLSM of the decimated data. Constant gain of 1.5E8.

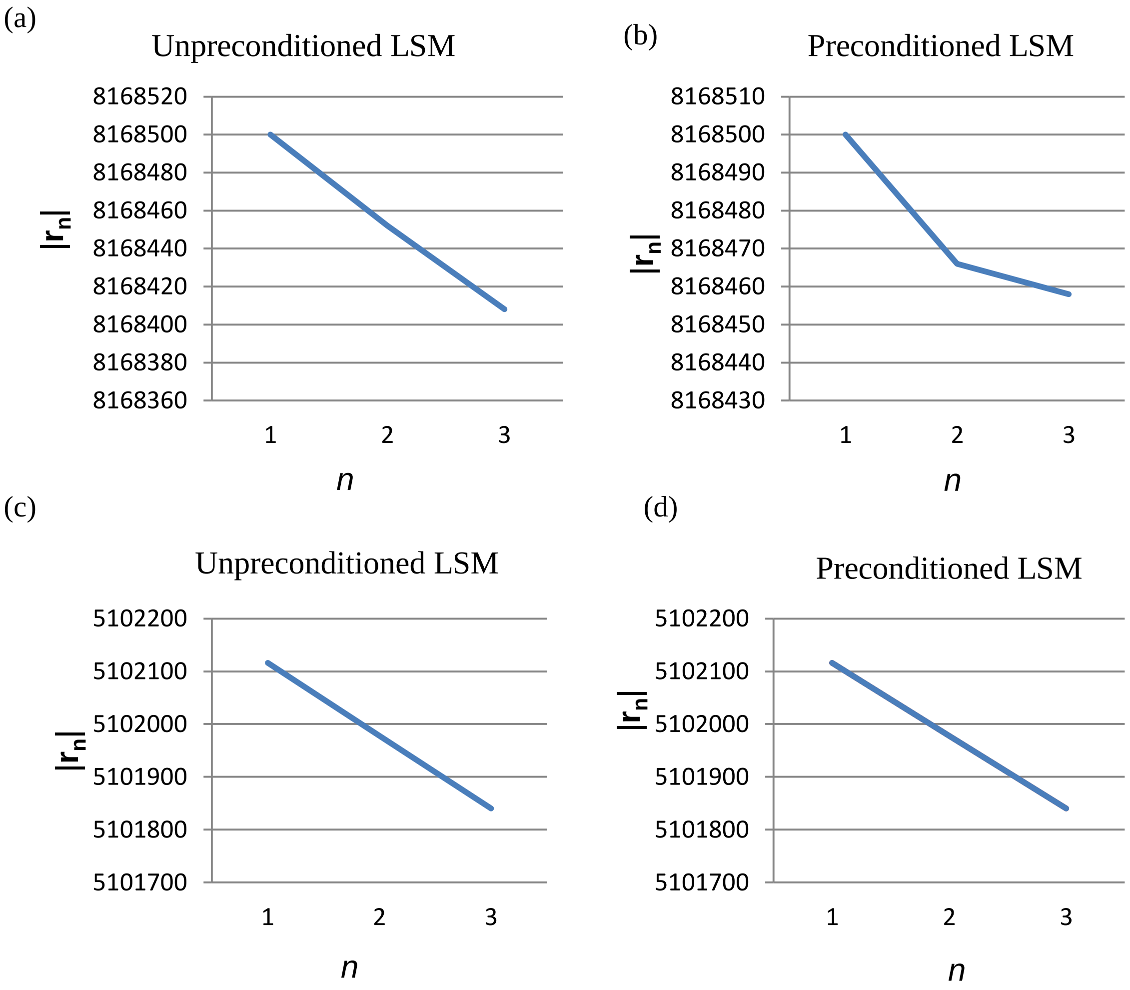

Figure 4.6. Change of residue as iterations increase for (a) unpreconditioned and (b) preconditioned least-squares migration for the decimated Dickman dataset. Change of gradient with increasing iteration for the decimated Dickman dataset (c) unpreconditioned, and (d) preconditioned LSM. The initial, preconditioned solution converges faster (smaller value of $|\mathbf{r}|$), but then levels out. Without constraints, aliases that appear in the subsurface image provide a better fit to the surface data, regardless as to whether that component of the data is signal or noise.

4.3 PLSM of the undecimated Dickman data volume

Figure 4.7a shows the time-structure map of the top of the Gilmore City horizon interpreted from the conventional migrated seismic data volume. Figures 4.7b shows source and receiver pair map, which allows us predict the footprint pattern. Vertical slices through seismic amplitude along profiles AA’ and BB’ are shown in Figures 4.7c and Figures 4.8, 4.9 and 4.10. White block arrows show collapse features near the top of the Gilmore City horizon which underlies the Mississippian reservoir. Red block arrows indicate noise.

Figure 4.8 shows vertical slices through seismic amplitude along profiles AA’ of conventional migration, the low signal-to-noise ratio causes the poor illumination for the layers, and random noise masks subtle geological features. After two and three iterations of PLSM in Figurers 4.9 and 4.10, the signal-to-noise ratio is enhanced and there is less noise contamination, which interferes with the main reflected energy from conventional migration. Figure 4.11 shows Vertical slice through noise difference amplitude between the original modeled data $\boldsymbol{m_1}$and structure-oriented filtered model $\widetilde{\boldsymbol{m}}_{\boldsymbol{1}}$along profiles AA’, note the noise rejected after structure-oriented filter applied.

Figure 4.12 shows vertical slices through seismic amplitude along profiles BB’ of conventional migration, the low signal-to-noise ratio causes the poor illumination for the interpretation of fault denoted by white block arrow. After two and three iterations after PLSM in Figurers 4.13 and 4.14, the signal-to-noise ratio is highly enhanced and there is less noise contamination, better showing the fault.

Figure 4.15 shows a time slice at *t*=0.406s of the stacked volume after conventional migration. The red block arrow indicates footprint, its contamination interferes with the interpretation of subtle geological features. After two and three iterations of PLSM in Figure 4.16 and Figure 4.17, the footprint is almost eliminated and the structural features are retained.

Figure 4.18 shows coherence horizon slices through coherence volumes along the Gilmore City after conventional migration. The red block arrow denotes the contamination of random noise on the coherence attribute. After two iterations of PLSM in Figure 4.19, contaminating noise is suppressed. After three iterations of PLSM in Figure 4.20, most random noise is gone. The red block arrows highlight the karst features in form of collapse character.

Figure 4.21 shows co-rendered horizon slices along the Gilmore city through the inline coherent energy gradient (the derivative of the energy along local dip and azimuth) co-rendered with coherent energy volumes after conventional migration. While this image highlights the karst collapse features, the presence of footprint and other noise contaminates the image. Figures 4.22 and 4.23 show the same two attributes after two and three iterations of PLSM. The resulting co-rendered attribute illumination of the karst collapse features is significantly improved.

Figure 4.24 shows a horizon slice along the Gilmore City through the most negative principal curvature computed from conventional migration volume. The presence of footprint masks the karst-enhanced fracture. Figure 4.25 and 4.26 show the improvement (white arrow) after two and three iterations of PLSM. Note the strike of *k2* curvature trends NE-SW.

Figure 4.27 shows representative unmigrated traces from the middle of the survey (trace numbers 100000 to 10050). Figure 4.28 shows the corresponding demigrated gathers from conventional migration. Note that the demigrated gathers contain mainly coherent reflected events compared with the original gathers. Unfortunately, these demigrated data has a very different scale of α. Figure 4.29 and d display demigrated gathers after two and three iterations of PLSM, the random noise is significantly attenuated and coherent reflections are enhanced. In contrast, PLSM better approximates the original data, allowing us to construct the residual $\mathbf{r}$ at each iteration. Random noise in the demigrated image of the conventionally migrated data indicates that such noise has leaked into the subsurface image. In contrast, the demigrated reflectors become increasingly coherent with the number of iterations in PLSM (white block arrows), indicating that only signal (or noise consistent with signal) remains in the subsurface images, $\mathbf{m_n}$.

Figure 4.31 shows the common reflection point (CPR) prestack gathers from conventional migration. The red block arrow indicates hockey sticks at longer offsets. Figure 4.32 shows same result but new after muting to remove the hockey sticks, the noise as white block arrow shown can interfere the AVO gradient implement and elastic inversion. After the two iterations and three iterations after PLSM in Figure 4.33 and Figure 4.34 these events show more continuation and less noise contamination, so the application of PLSM can make the AVO analysis and elastic inversion more accurate.

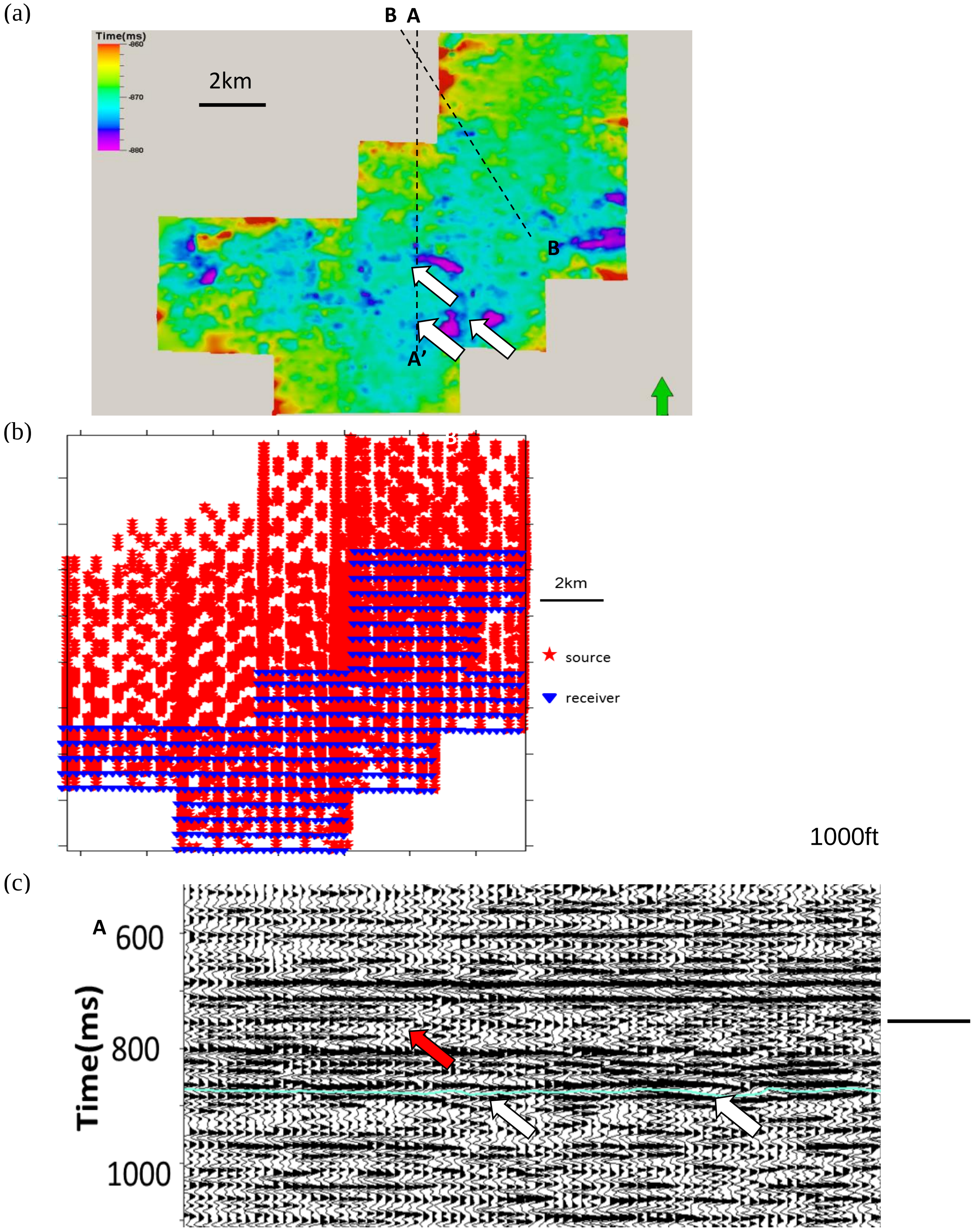

Figure 4.7. (a) Time-structure map of the top of the Gilmore City horizon, (b) source and receiver pair map, (c)the vertical slice through the line AA'. White arrows show collapse features, red arrow shows noise.

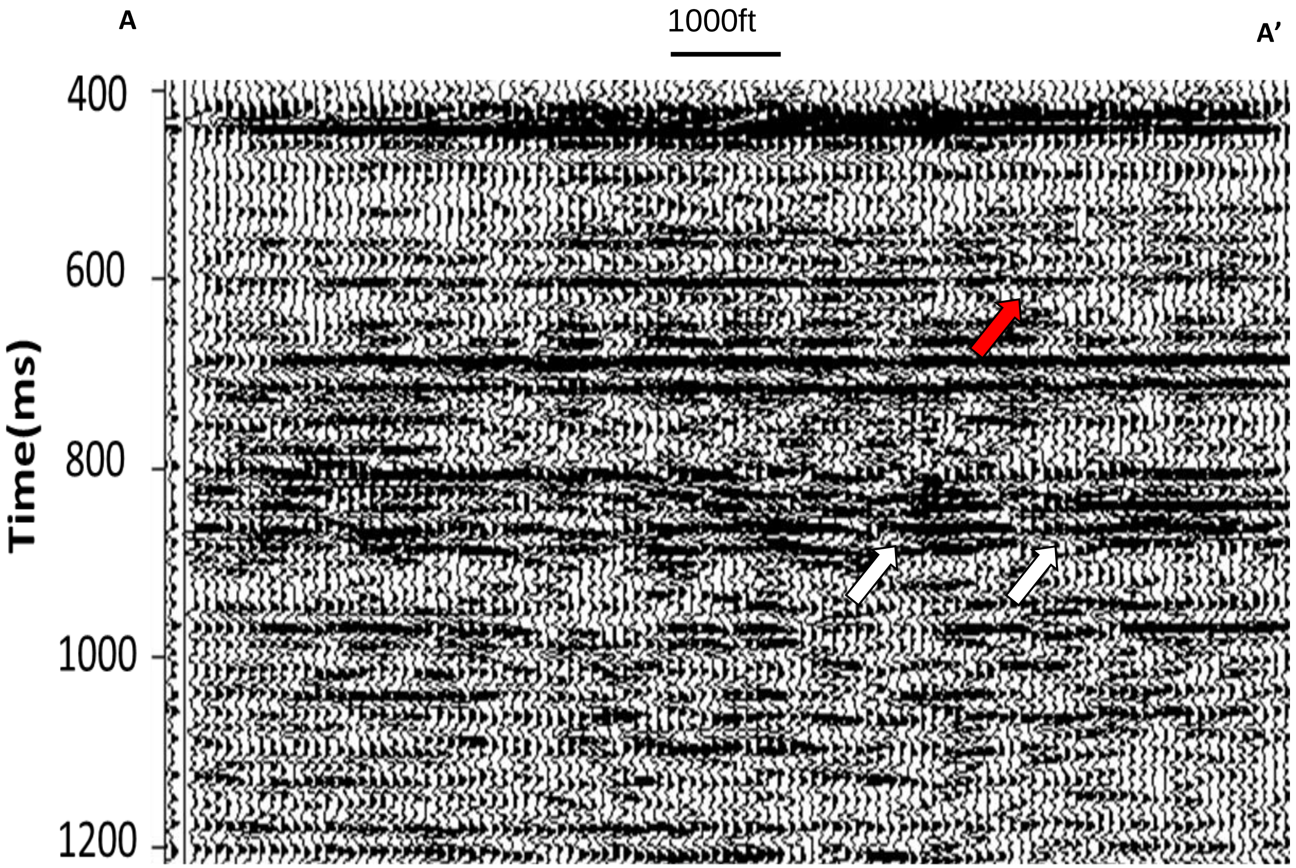

Figure 4.8. Vertical slice through seismic amplitude along profile AA' as shown in Figure 4.4a: (a) using conventional migration. White block arrows indicate the collapse features. Red arrow denote noise.

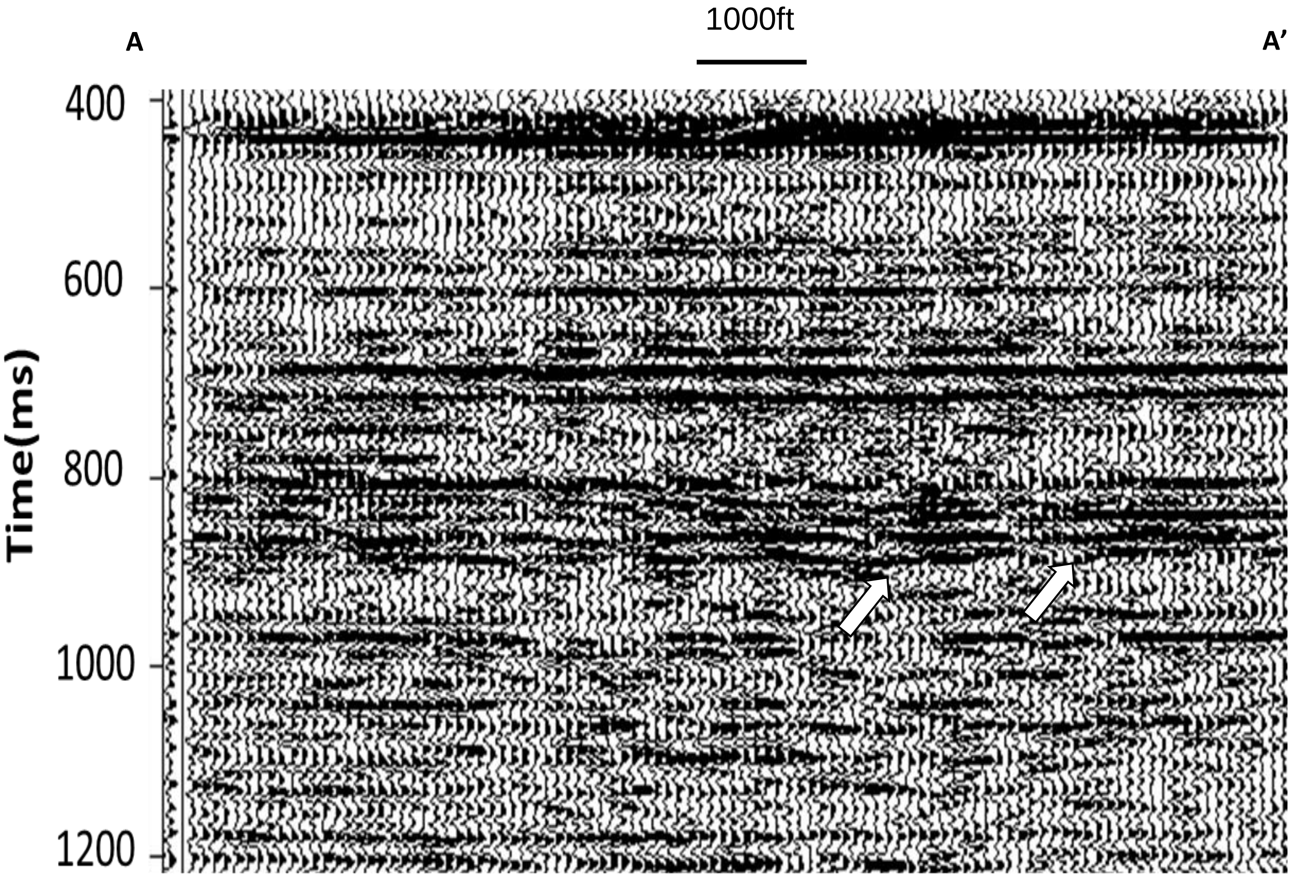

Figure 4.9 Vertical slice through seismic amplitude along profile AA’ as shown in Figure 4.4a after 2 iterations of PLSM. White block arrows indicate the collapse features.

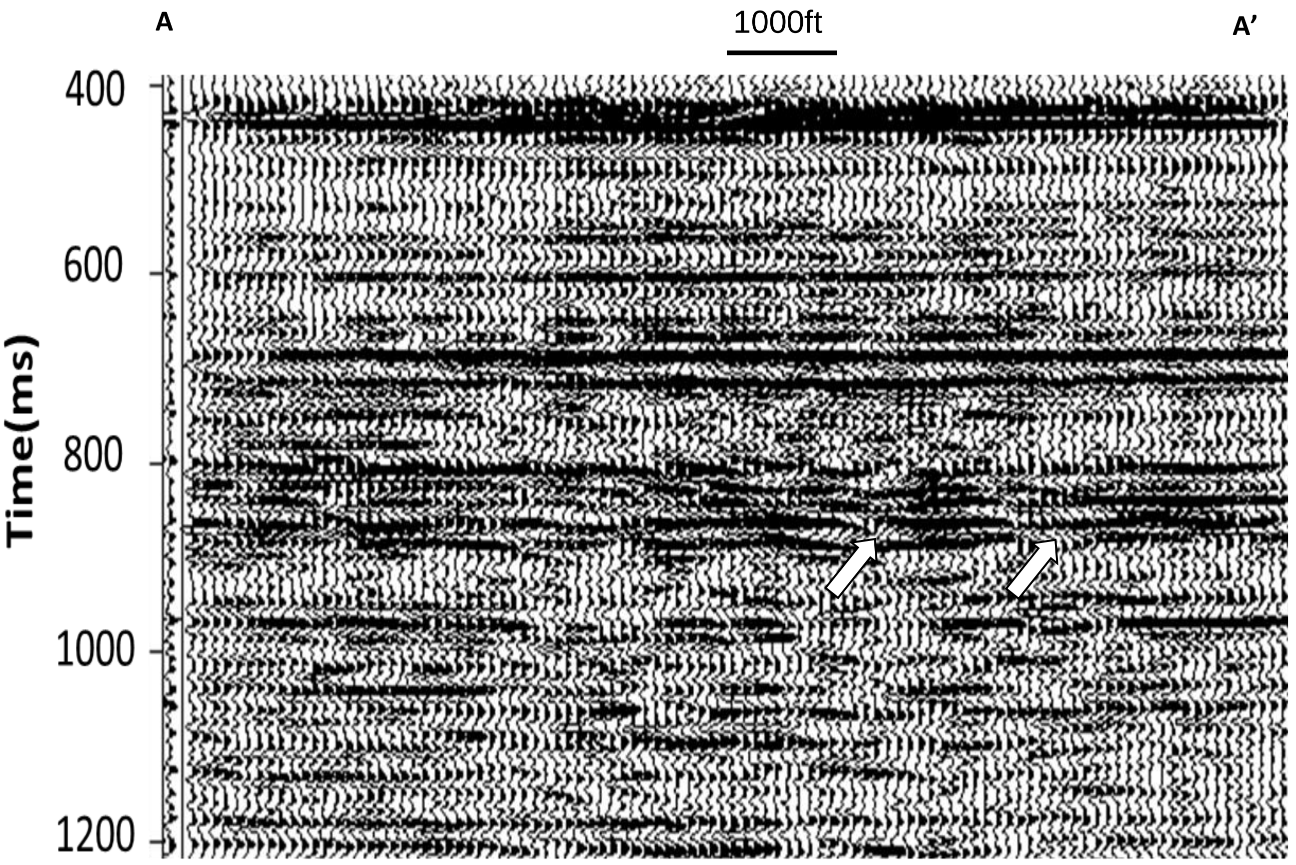

Figure 4.10 Vertical slice through seismic amplitude along profile AA’ as shown in Figure 4.4a after 3 iterations of PLSM. White block arrows indicate the collapse features.

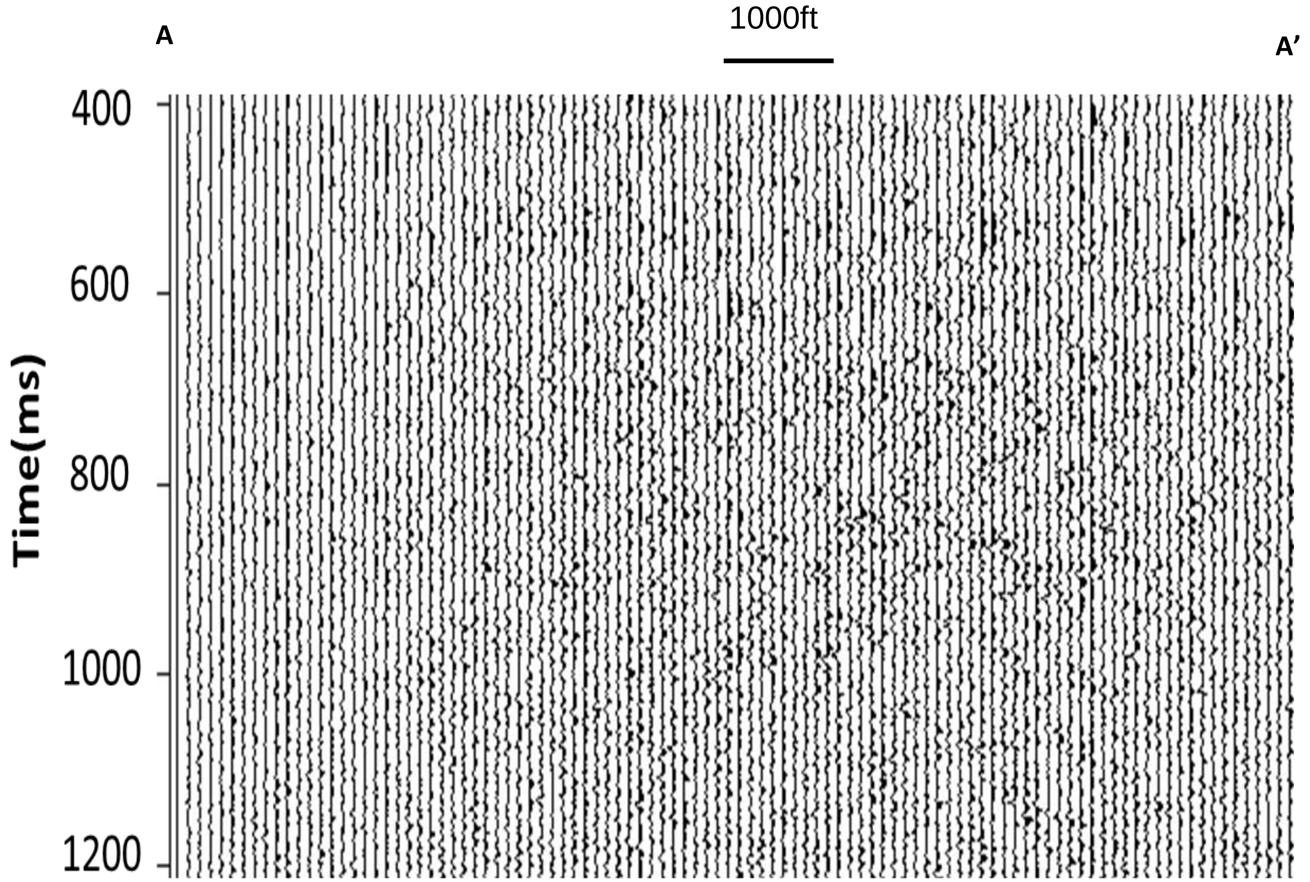

Figure 4.11. Vertical slice through the difference between the original modeled data $\boldsymbol{m_1}$and structure-oriented filtered model$\widetilde{\boldsymbol{m}}_{\boldsymbol{1}}$along profile AA’.

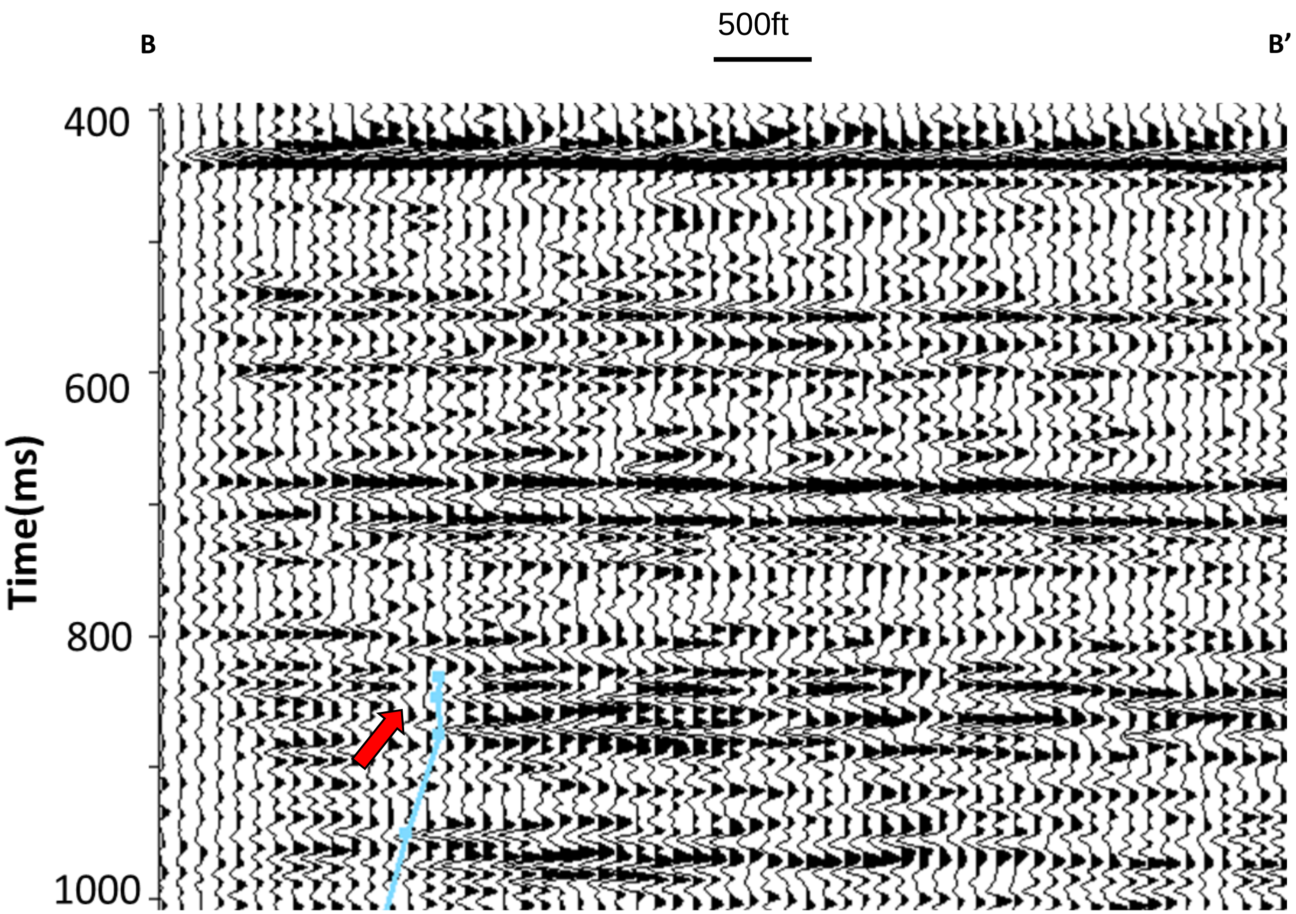

Figure 4.12 Vertical slice through seismic amplitude along profile BB’ as shown in Figure 4.4a after conventional migration. Red block arrows indicate the fault. After PLSM, the fault is better imaged.

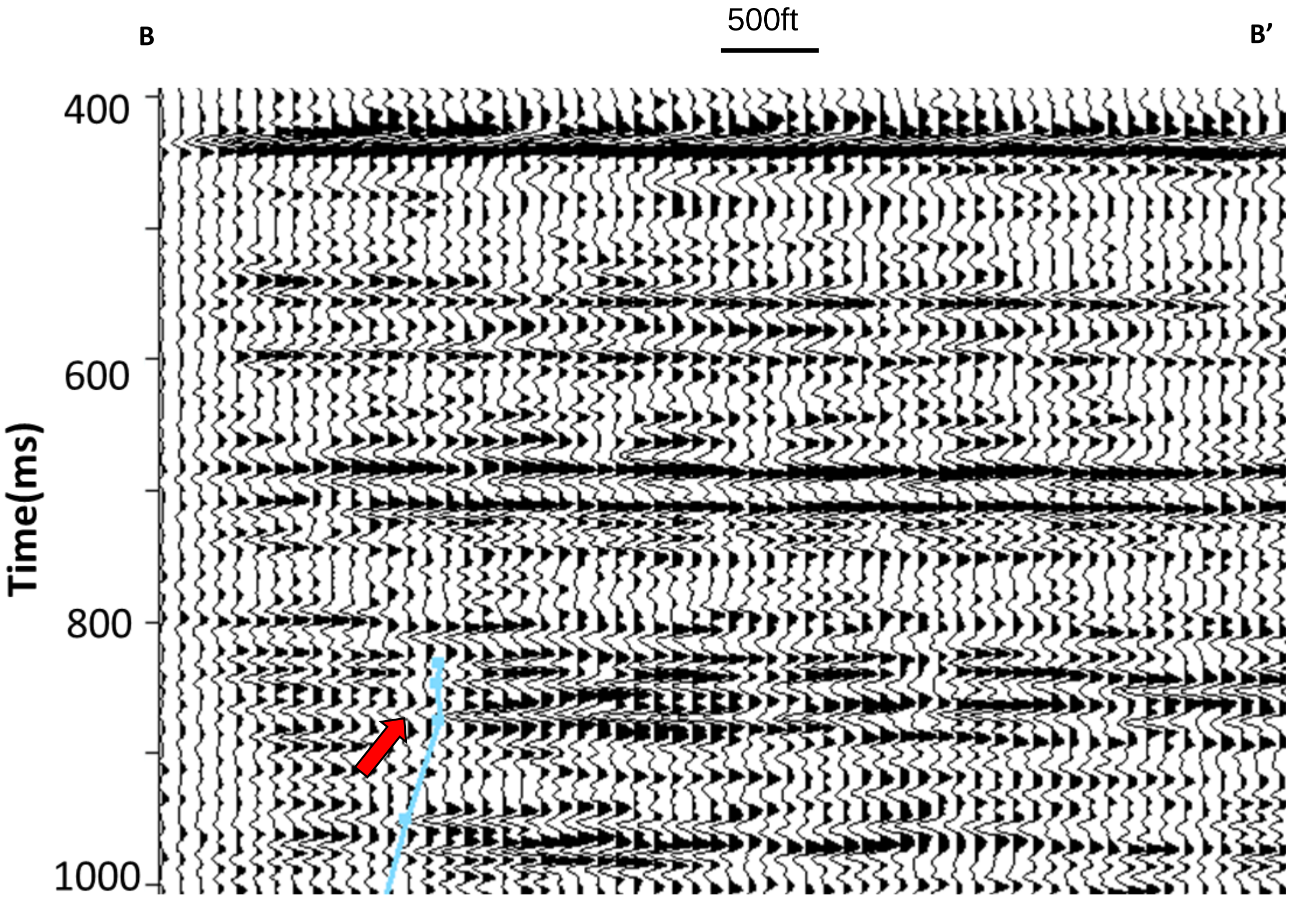

Figure 4.13. Vertical slice through seismic amplitude along profile BB’ as shown in Figure 4.4a after) two iterations of PLSM. Red block arrows indicate the fault. After PLSM, the fault is better imaged.

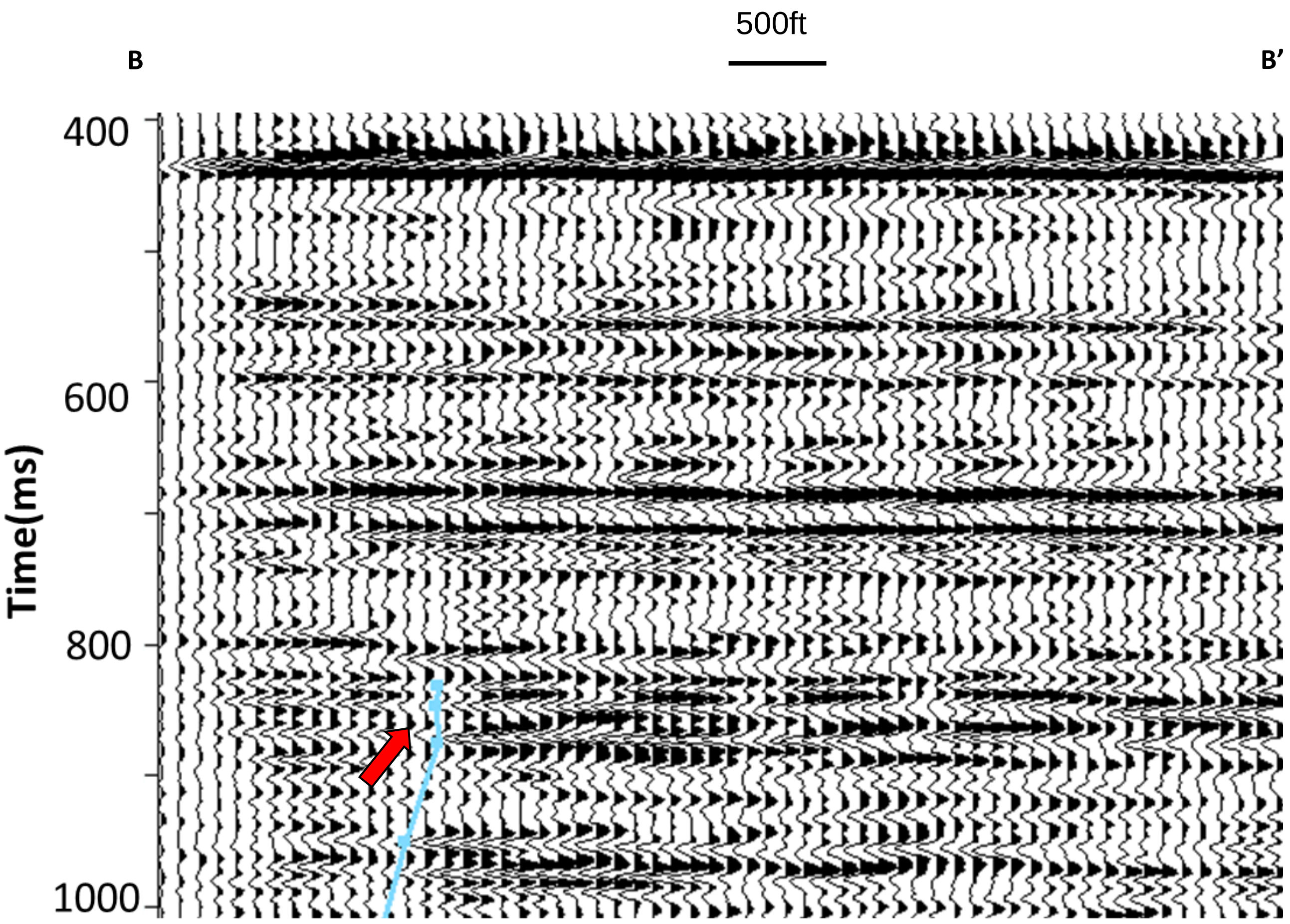

Figure 4.14. Vertical slice through seismic amplitude along profile BB’ as shown in Figure 4.4a after) three iteration of PLSM. Red block arrows indicate the fault. After PLSM, the fault is better imaged.

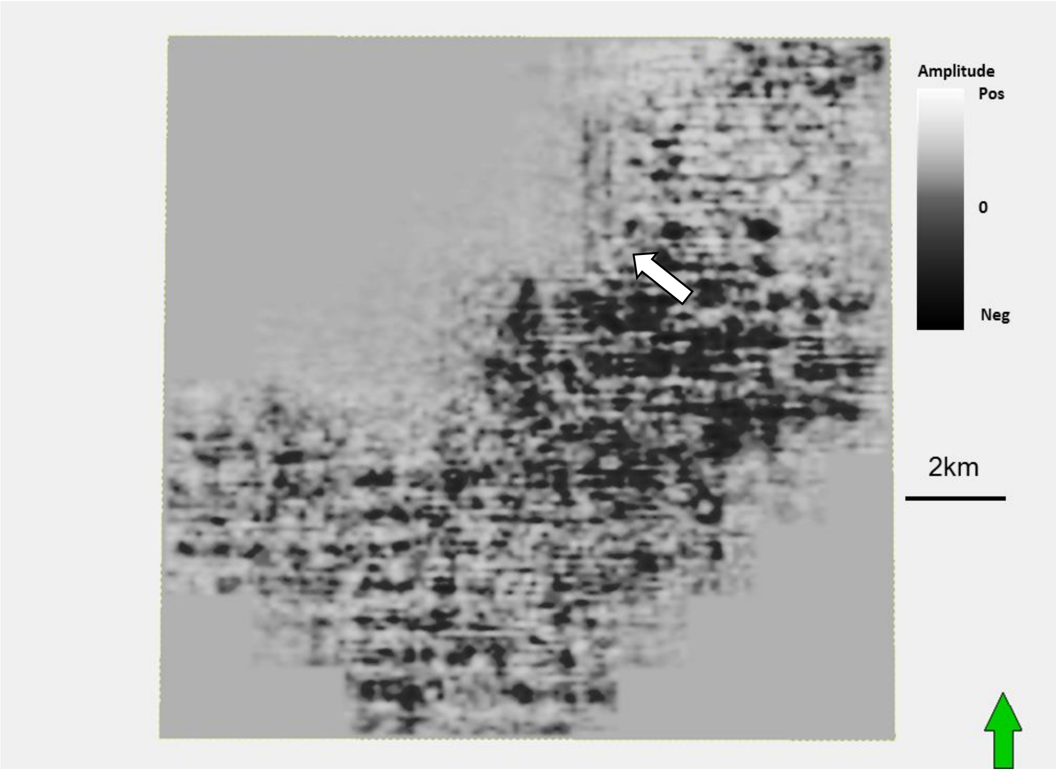

Figure 4.15. Time slice at *t*=0.406s through stacked amplitude volumes after conventional migration, the white block arrow in it indicates E-W and N-S footprint, which impedes interpretation.

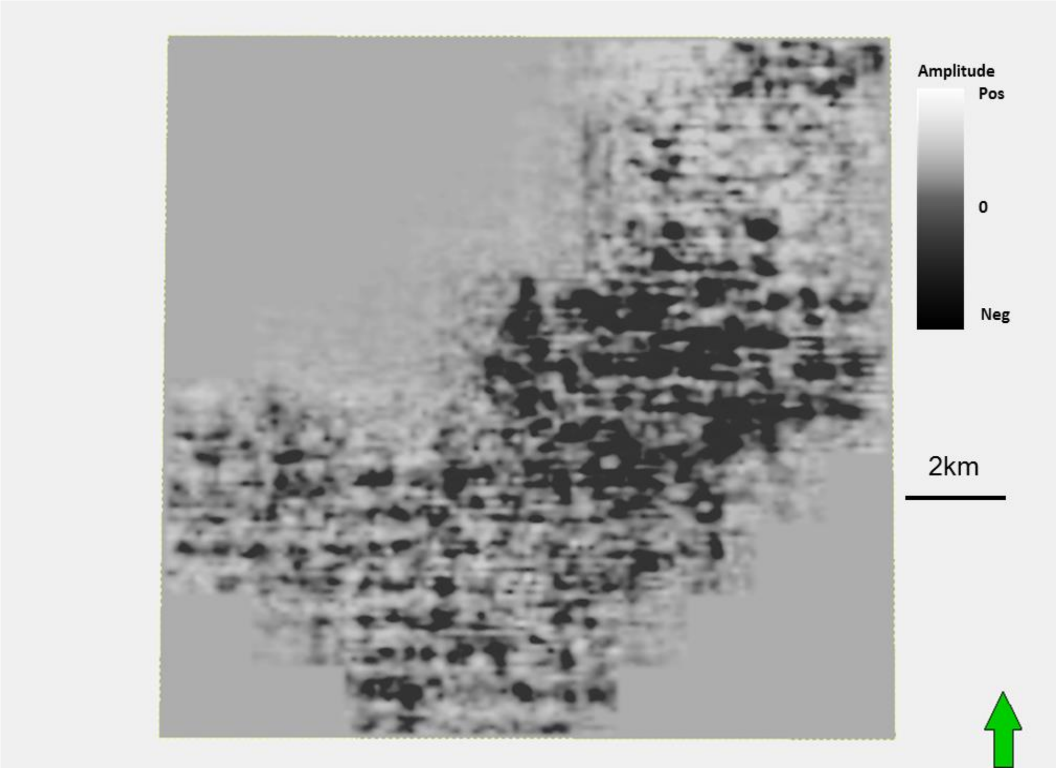

Figure 4.16. Time slice at *t*=0.406s through stacked amplitude volumes after two iterations of PLSM, PLSM attenuates the slow wavenumber footprint artifacts

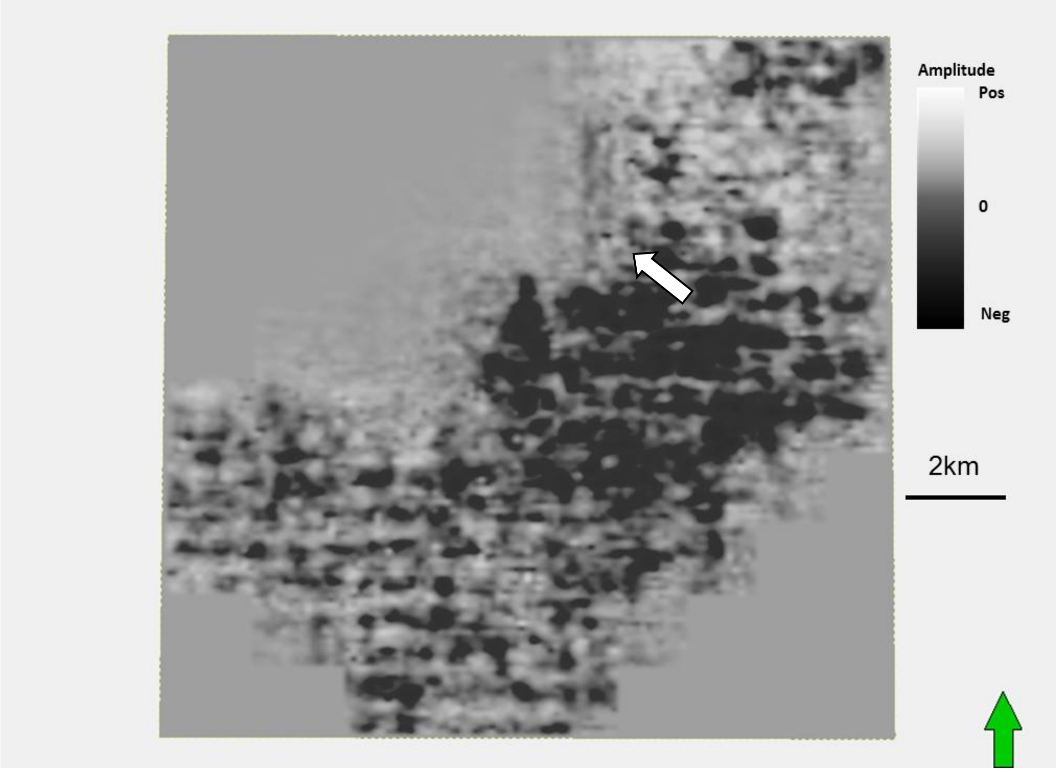

Figure 4.17. Time slice at *t*=0.406s through stacked amplitude volumes after three iterations of PLSM. The white block arrow indicates area where footprint is deeply attenuated.

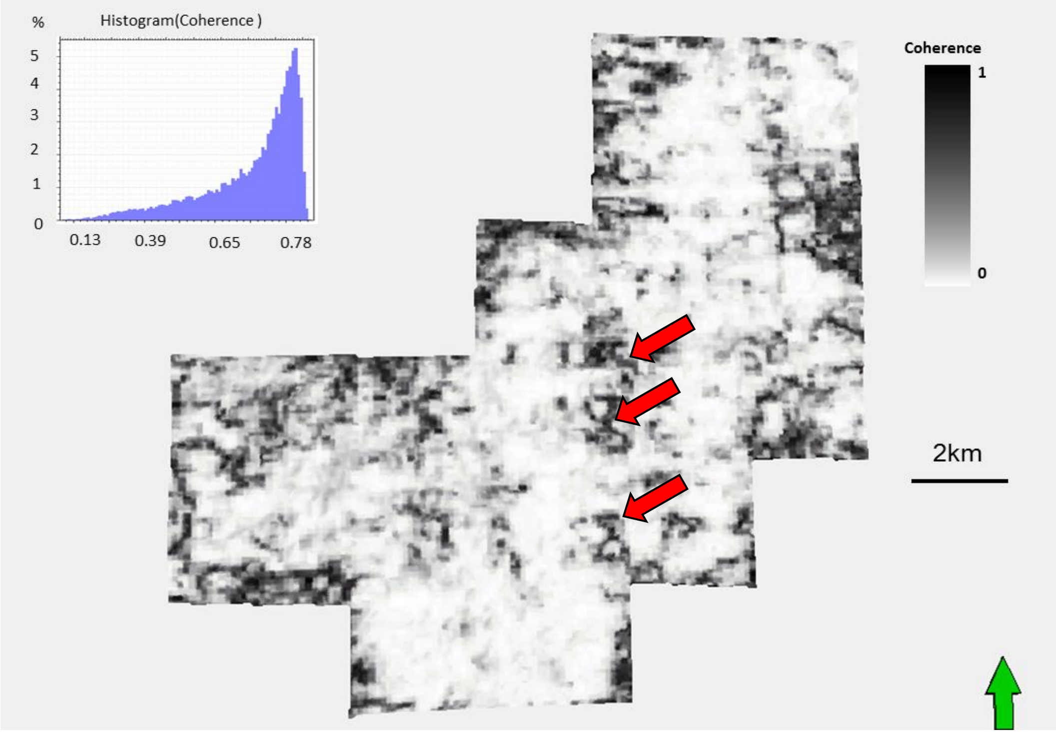

Figure 4.18. Horizon slices along the Gilmore City through coherence volumes computed from seismic amplitude using conventional migration, red block arrows indicate the karst collapse features.

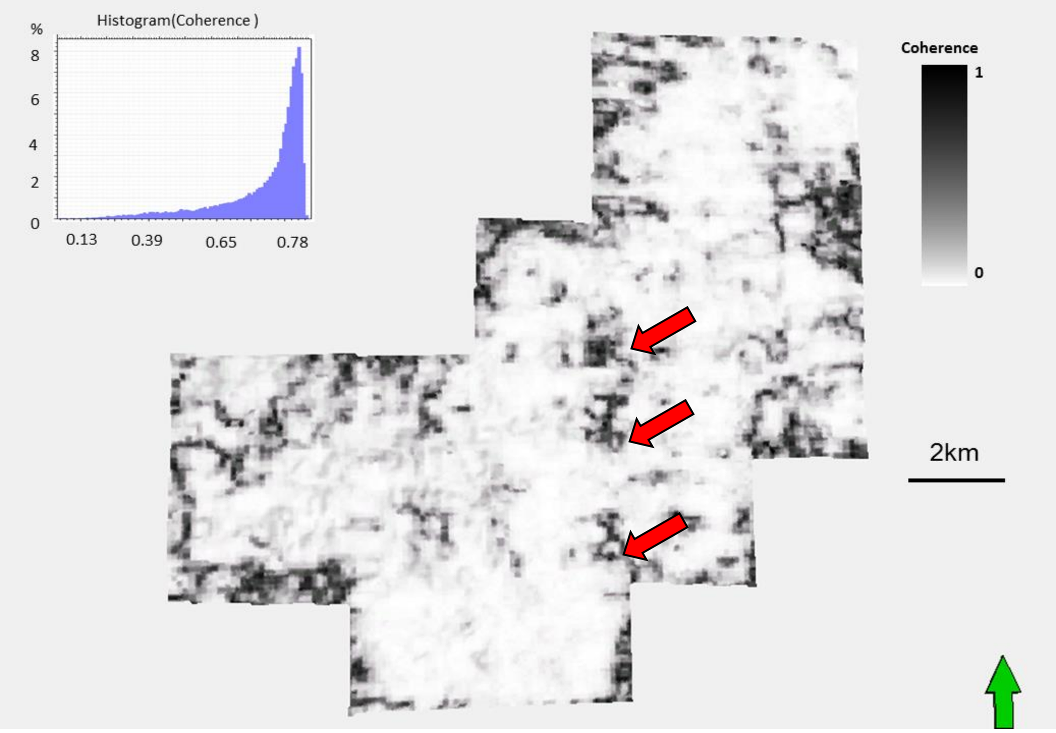

Figure 4.19. Horizon slices along the Gilmore City through coherence volumes computed from seismic amplitude after two iterations of PLSM. Red block arrows indicate the karst collapse features.

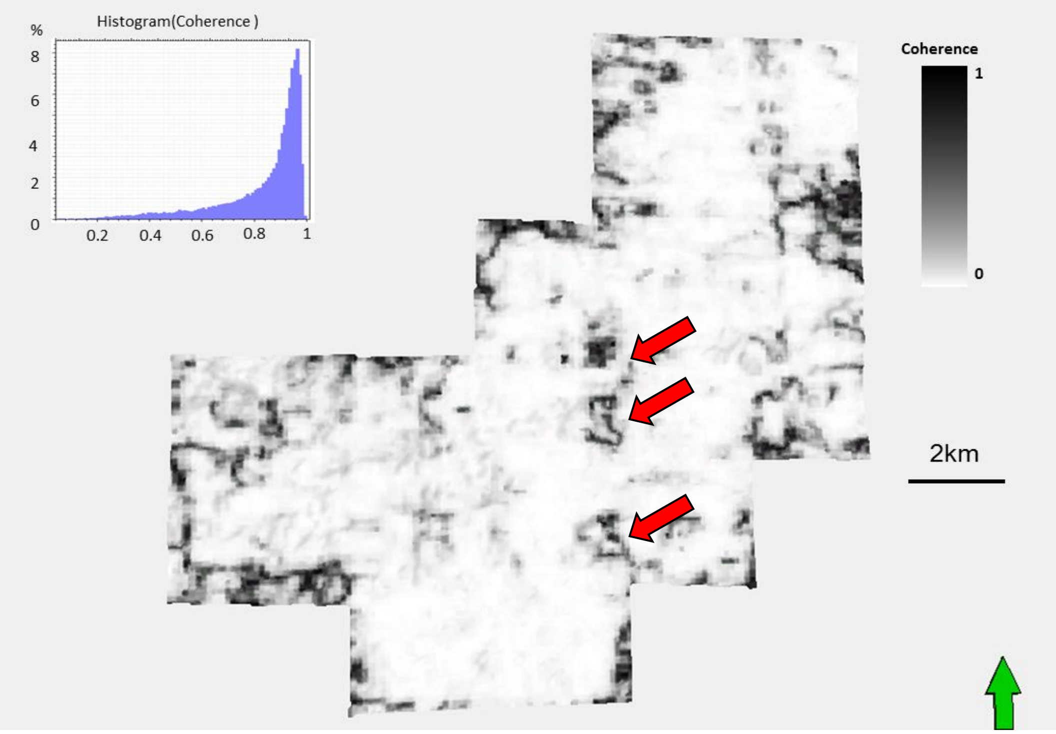

Figure 4.20. Horizon slices along the Gilmore City through coherence volumes computed from seismic amplitude after three iterations of PLSM. Red block arrows indicate the karst collapse features.

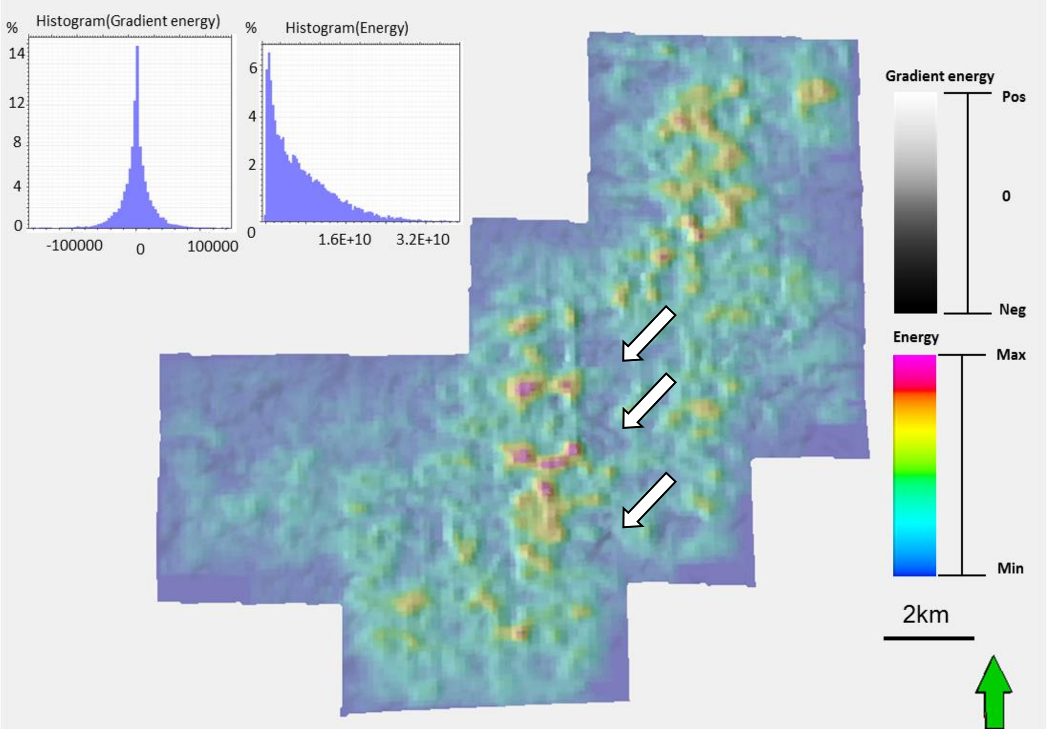

Figure 4.21. Horizon slices along the Gilmore City through inline gradient co-rendered with the coherent energy volumes computed from seismic amplitude using conventional migration. The white block arrows in indicate the collapse features.

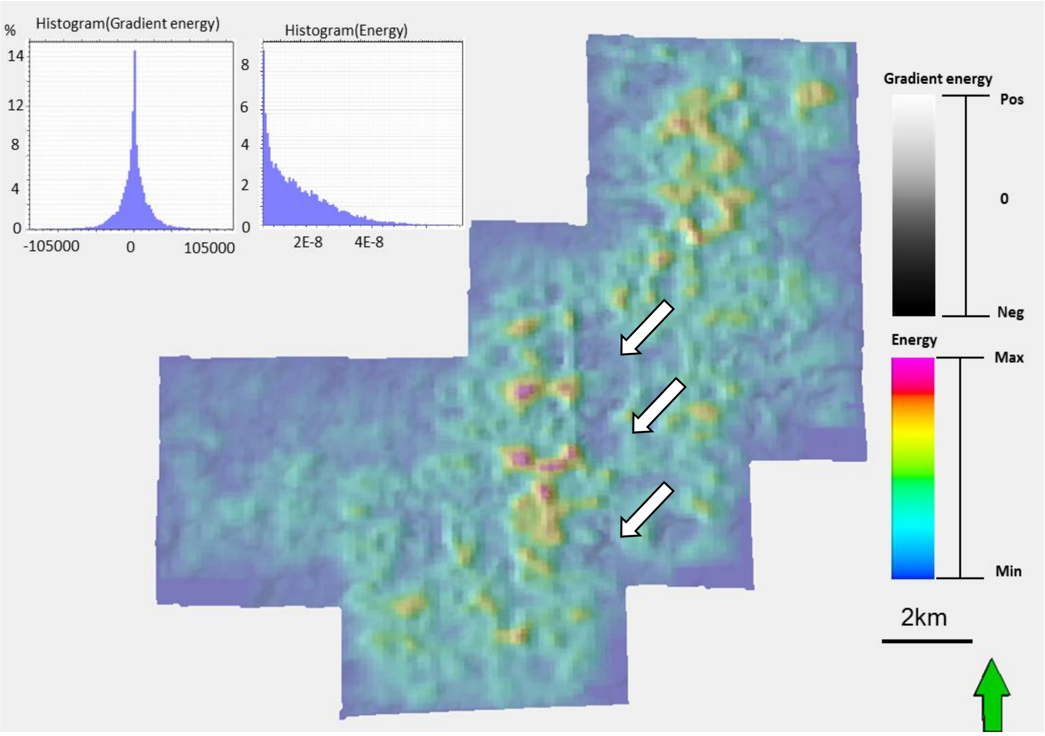

Figure 4.22. Horizon slices along the Gilmore City through inline gradient co-rendered with the coherent energy volumes computed from seismic amplitude after two iterations of PLSM, the white block arrows indicate the collapse features.

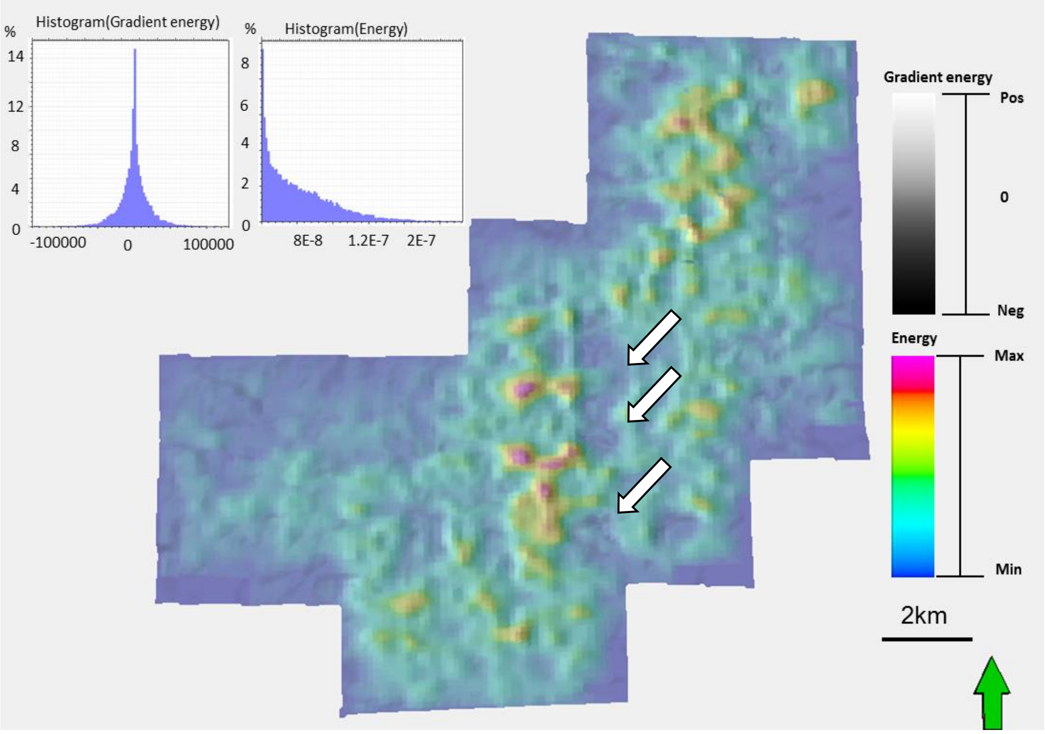

Figure 4.23. Horizon slices along the Gilmore City through inline gradient co-rendered with the coherent energy volumes computed from seismic amplitude after three iterations of PLSM, the white block arrows indicate the collapse features.

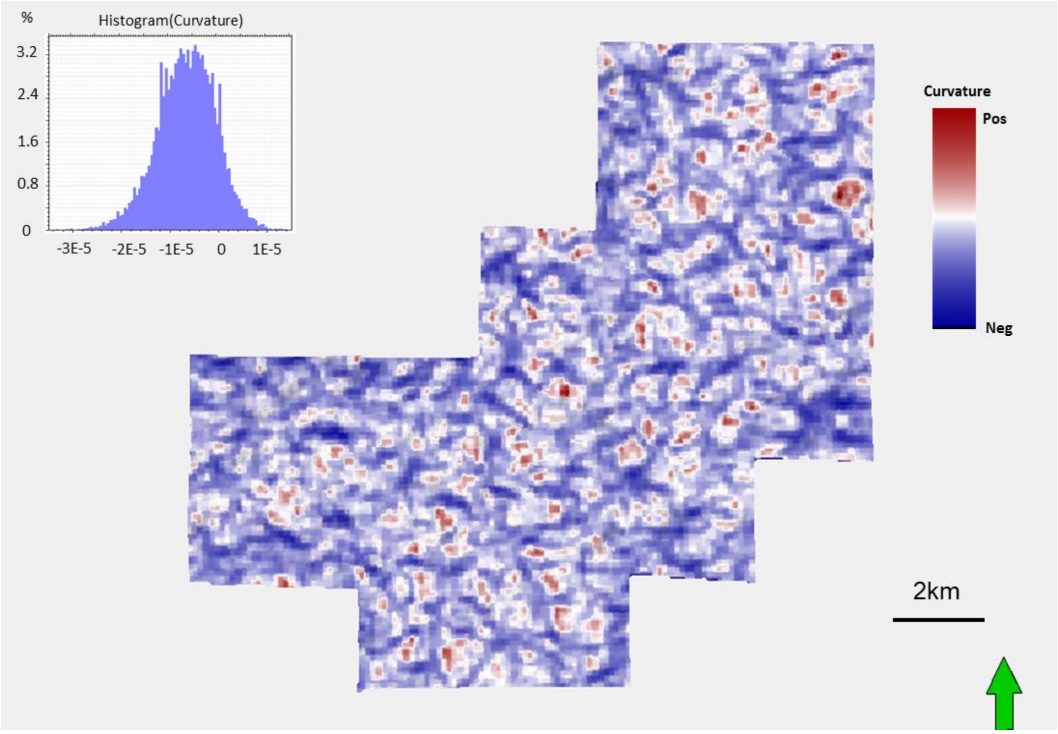

Figure 4.24. Horizon slices along the Gilmore City through K2 curvature volume computed from seismic amplitude: (a) using conventional migration.

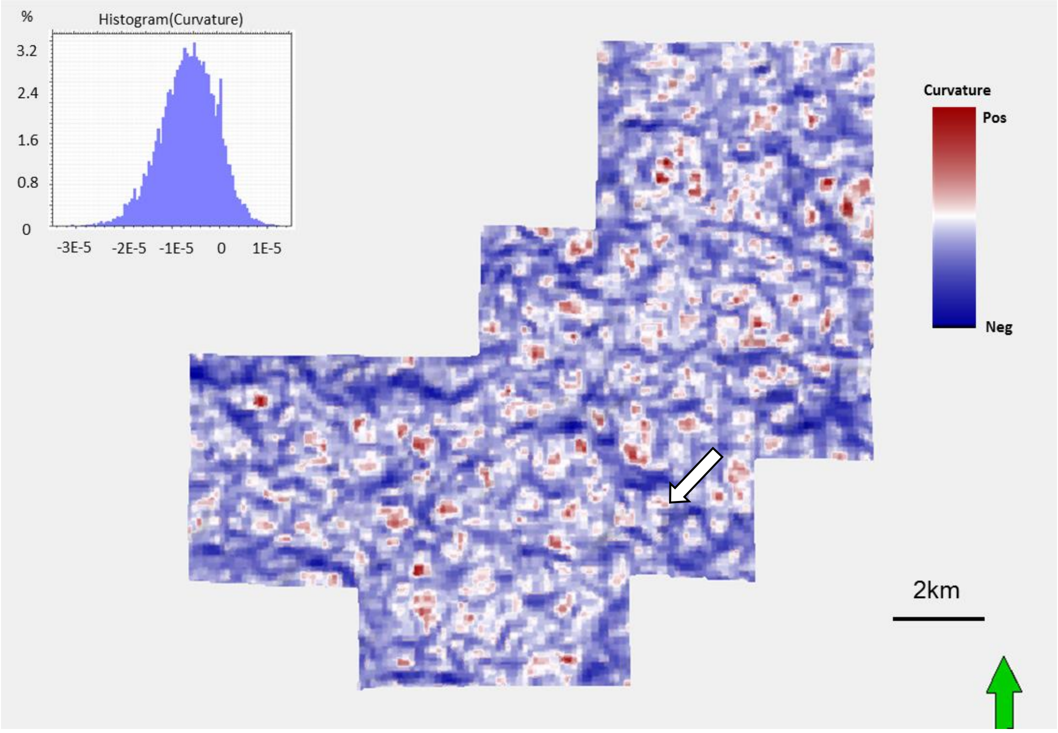

Figure 4.25. Horizon slices along the Gilmore City through K2 curvature volume computed from seismic amplitude after two iterations of PLSM. The white block arrow indicates the collapse features.

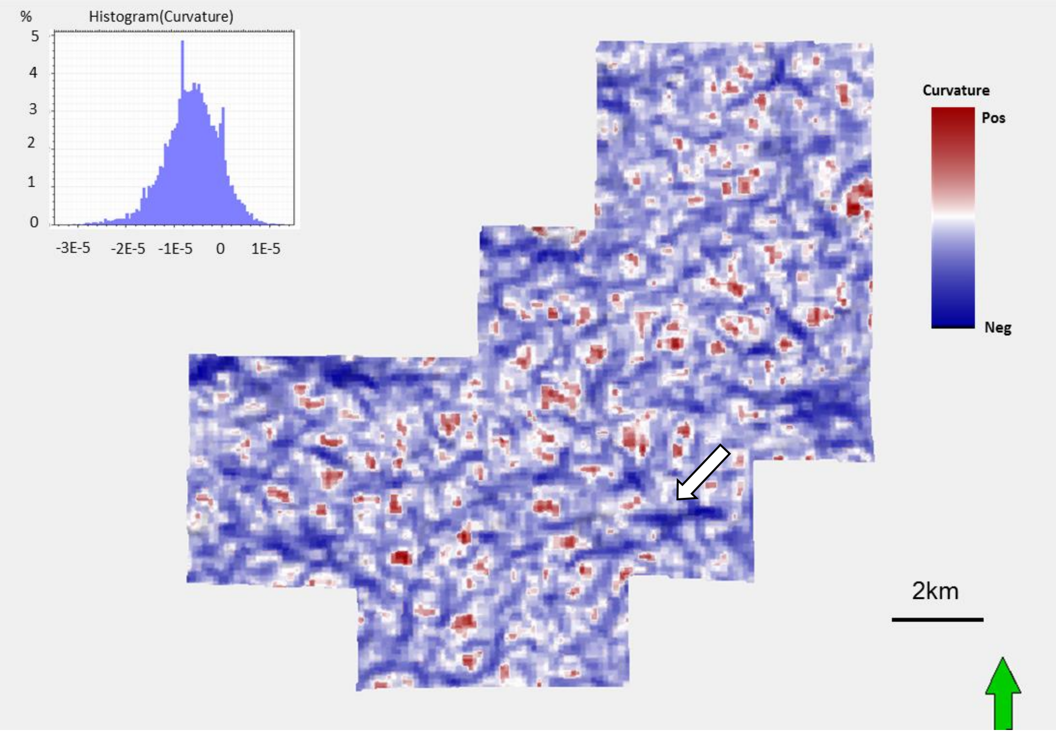

Figure 4.26. Horizon slices along the Gilmore City through K2 curvature volume computed from seismic amplitude after three iterations of PLSM. The white block arrow indicates the collapse features.

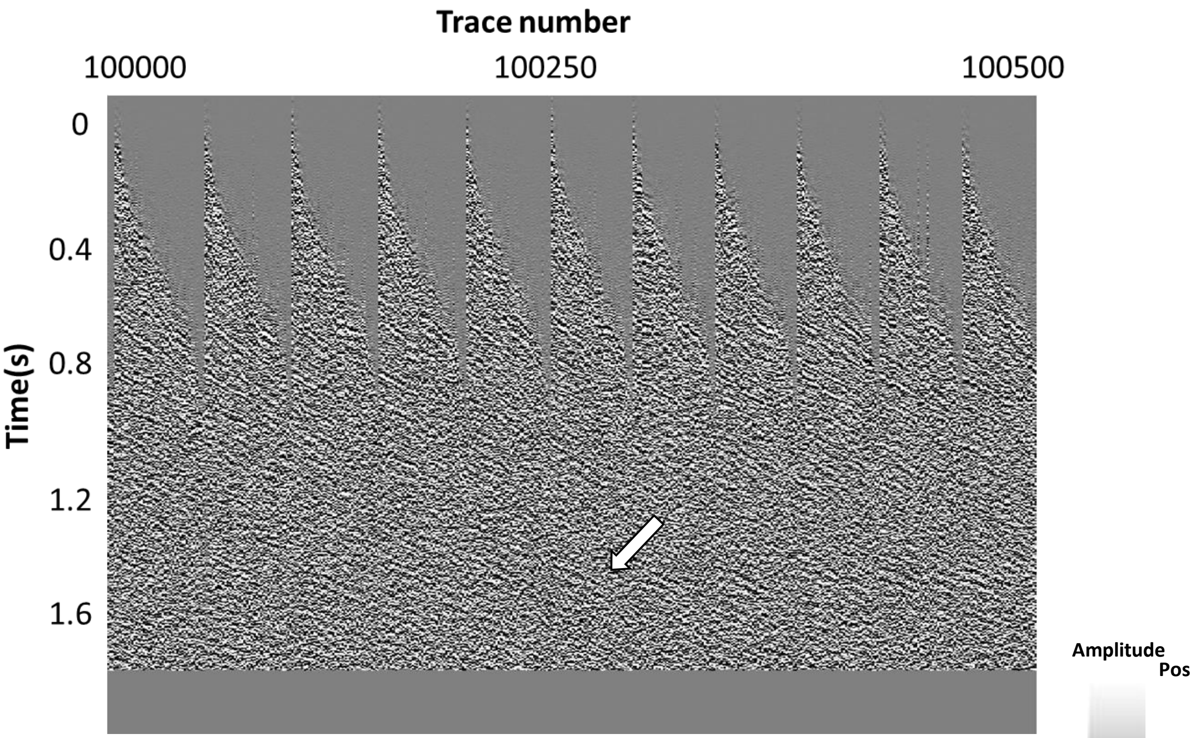

Figure 4.27. Representative traces from original seismic shot gathers data which was input to both conventional and the first iteration of PLSM migration.

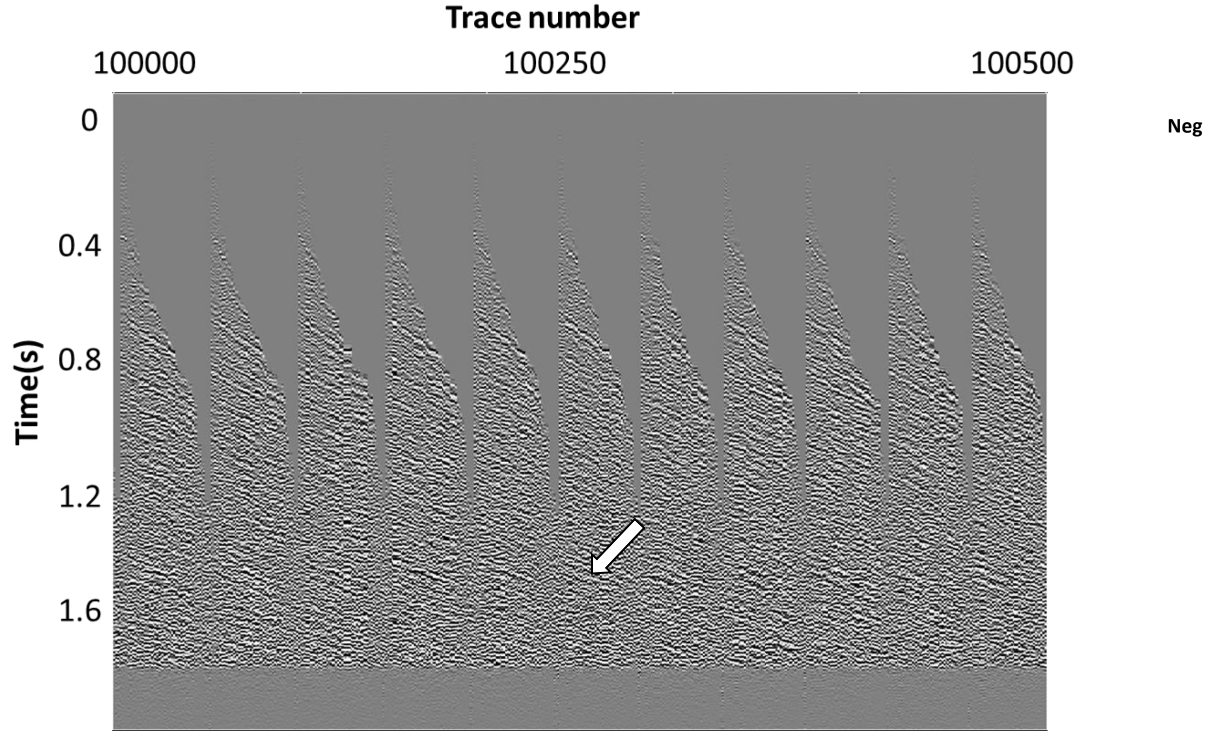

Figure 4.28. Representative traces from predicted (demigrated) gathers after conventional migration.

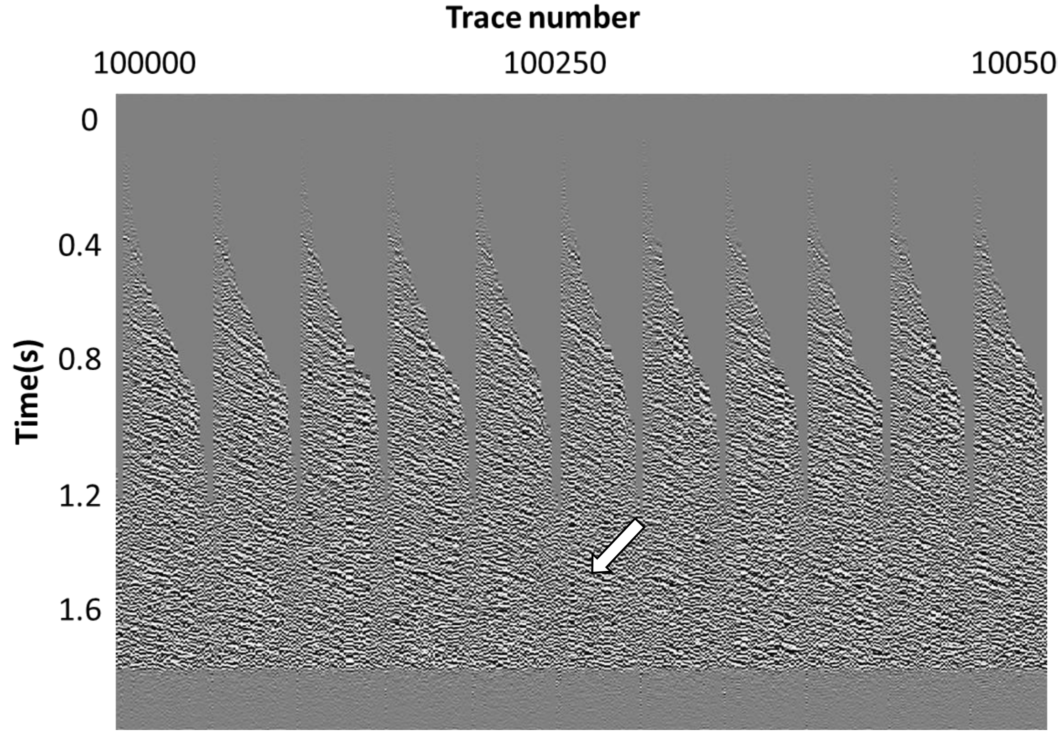

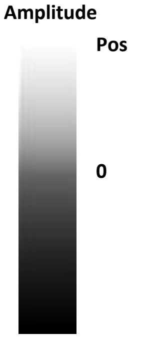

Figure 4.29. Representative traces from predicted (demigrated) gathers after two iterations of PLSM.

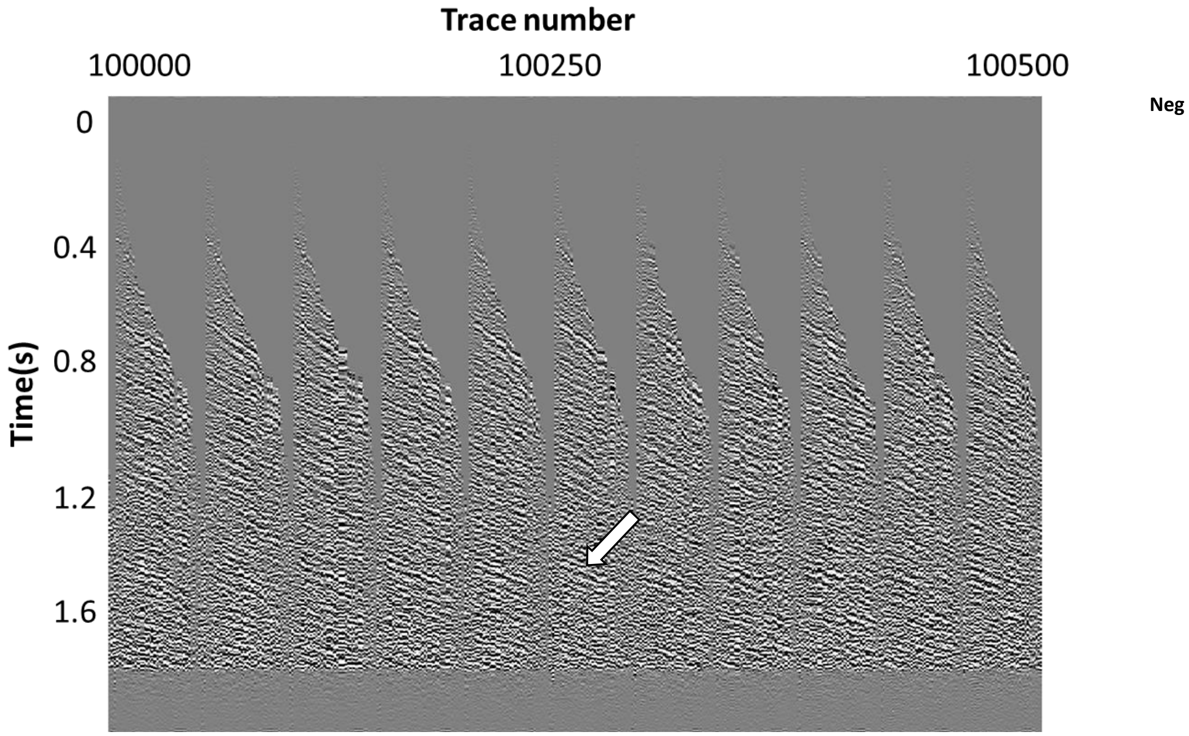

Figure 4.30. Representative traces from predicted (demigrated) gathers after three iterations of PLSM. Note the scale bar for the demigrated conventional gathers are different from the original input data.

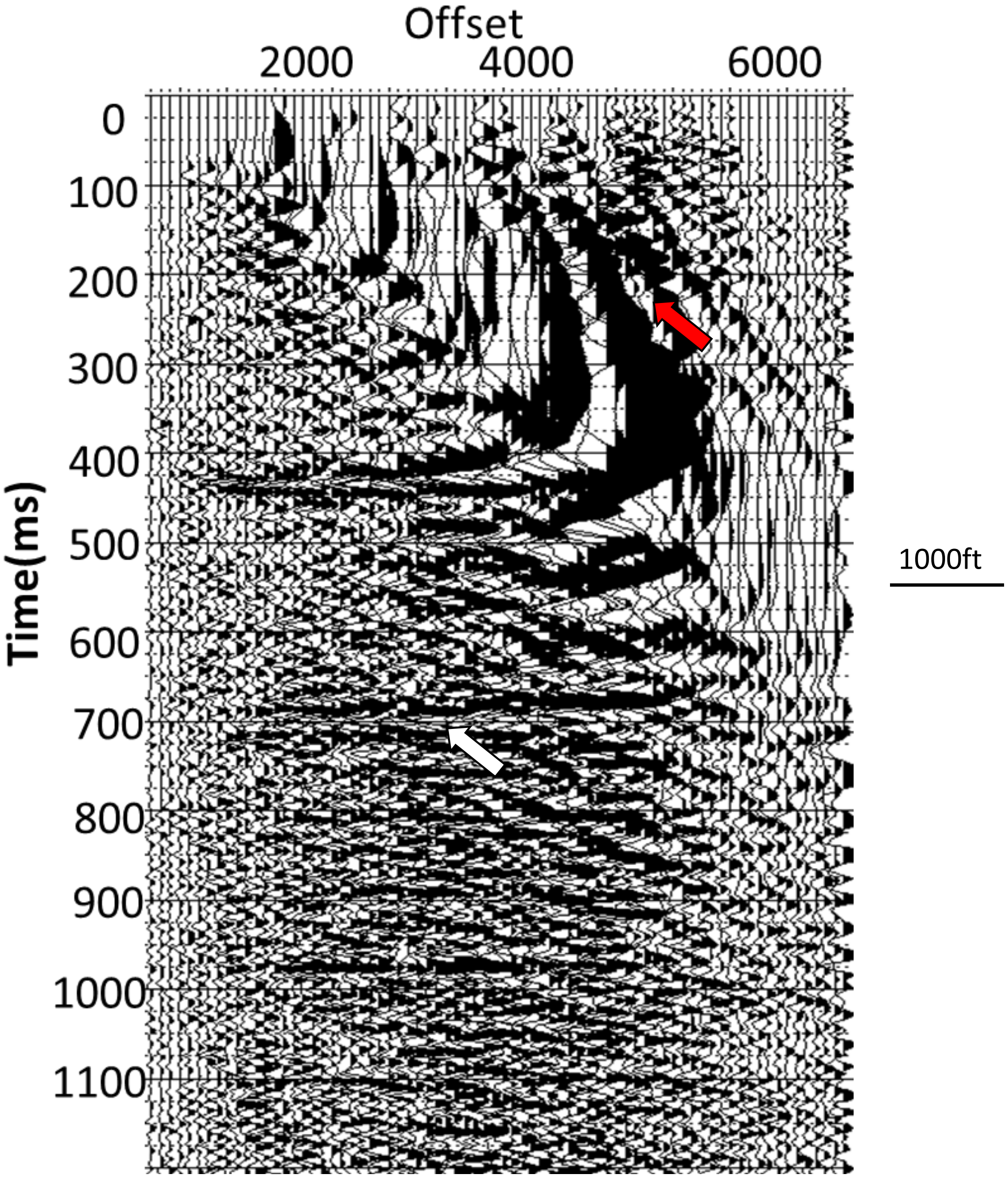

Figure 4.31. A representative conventionally migrated CRP gathers before muting. The red block arrow indicates migration stretch. The white block arrow indicates noise

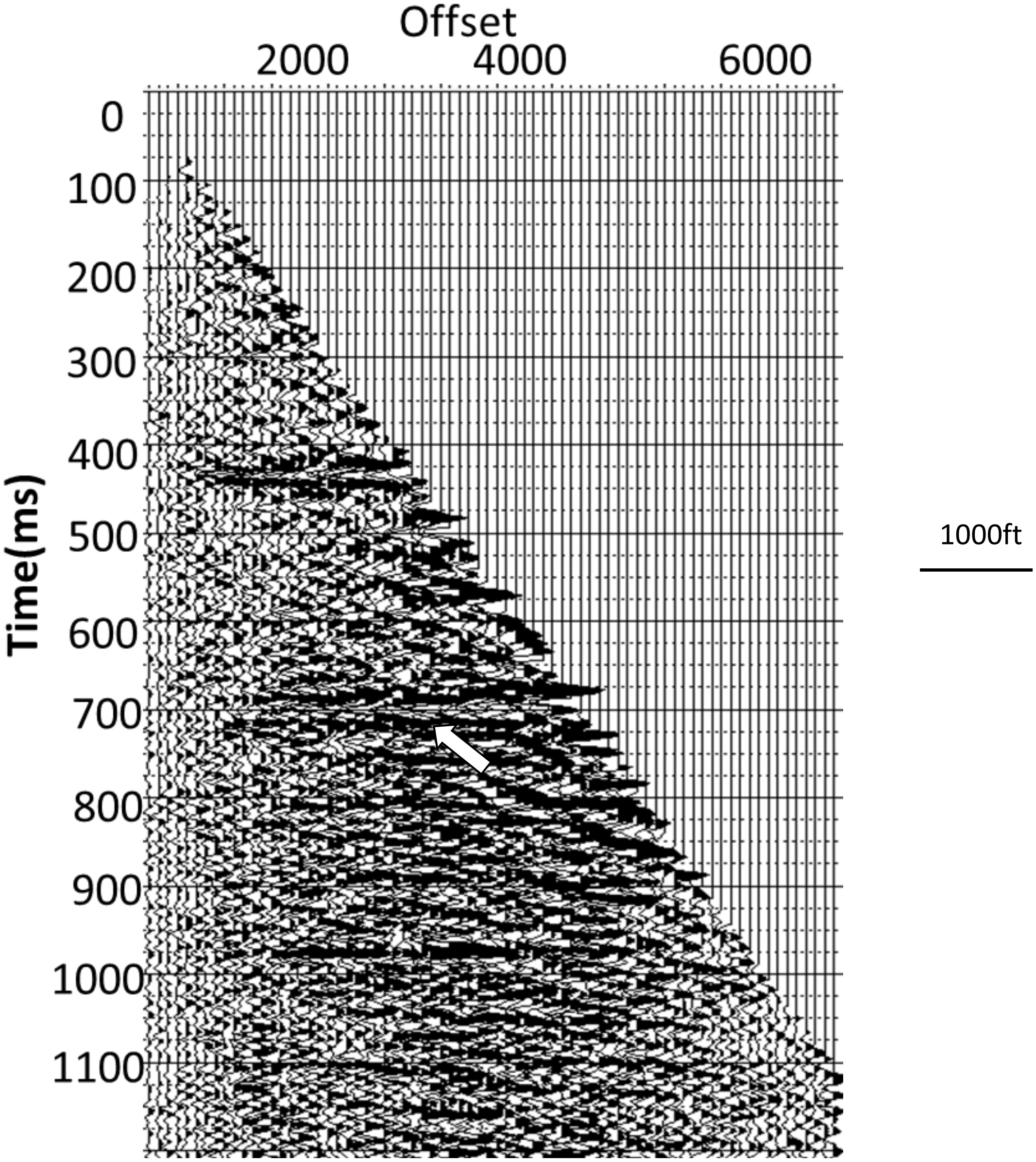

Figure 4.32. A representative conventionally migrated CRP gathers after muting. The white block arrow indicates noise

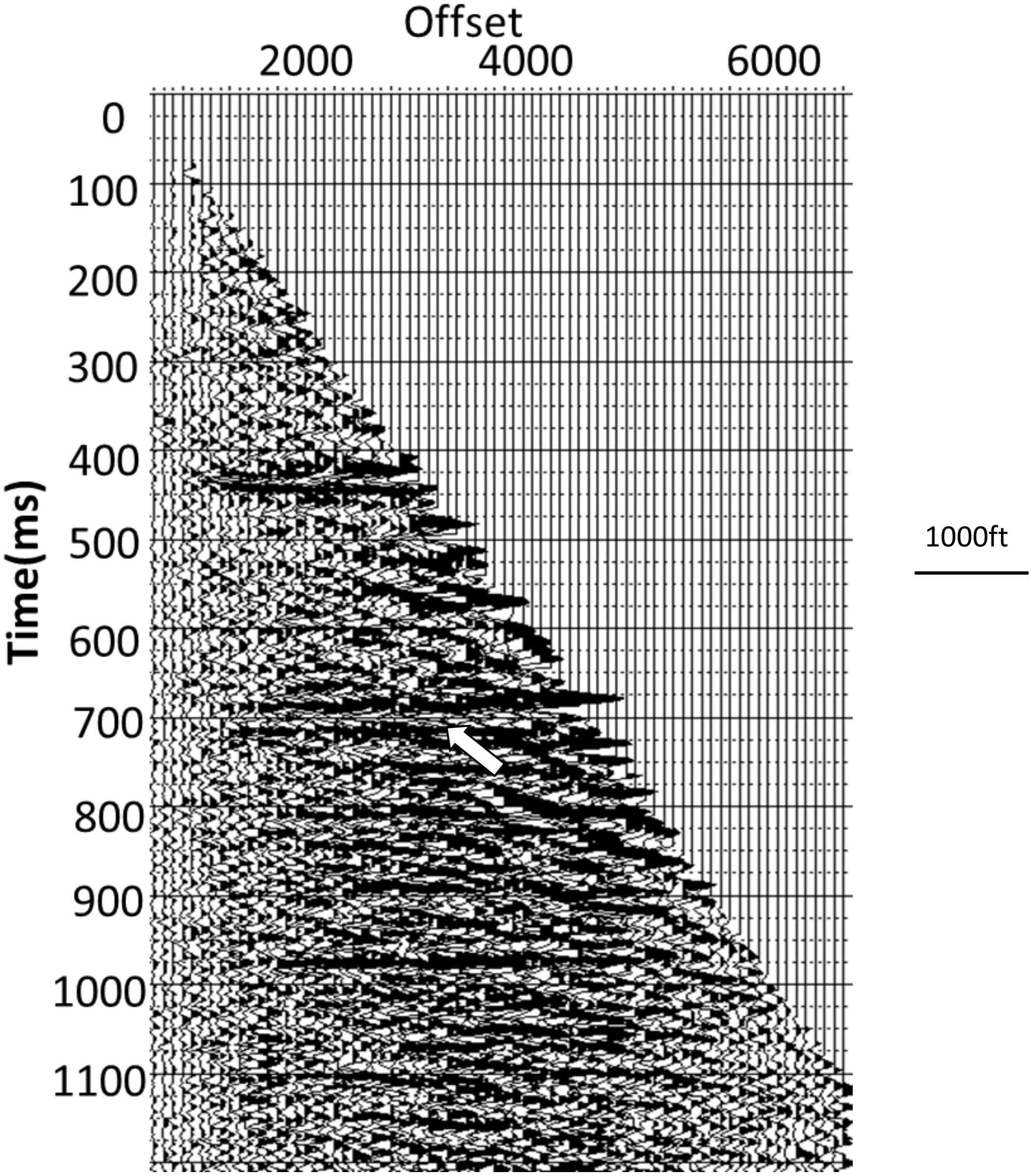

Figure 4.33. A representative conventionally migrated CRP gathers after two iterations of PLSM. The white block arrow indicates noise that has been attenuated using PLSM.

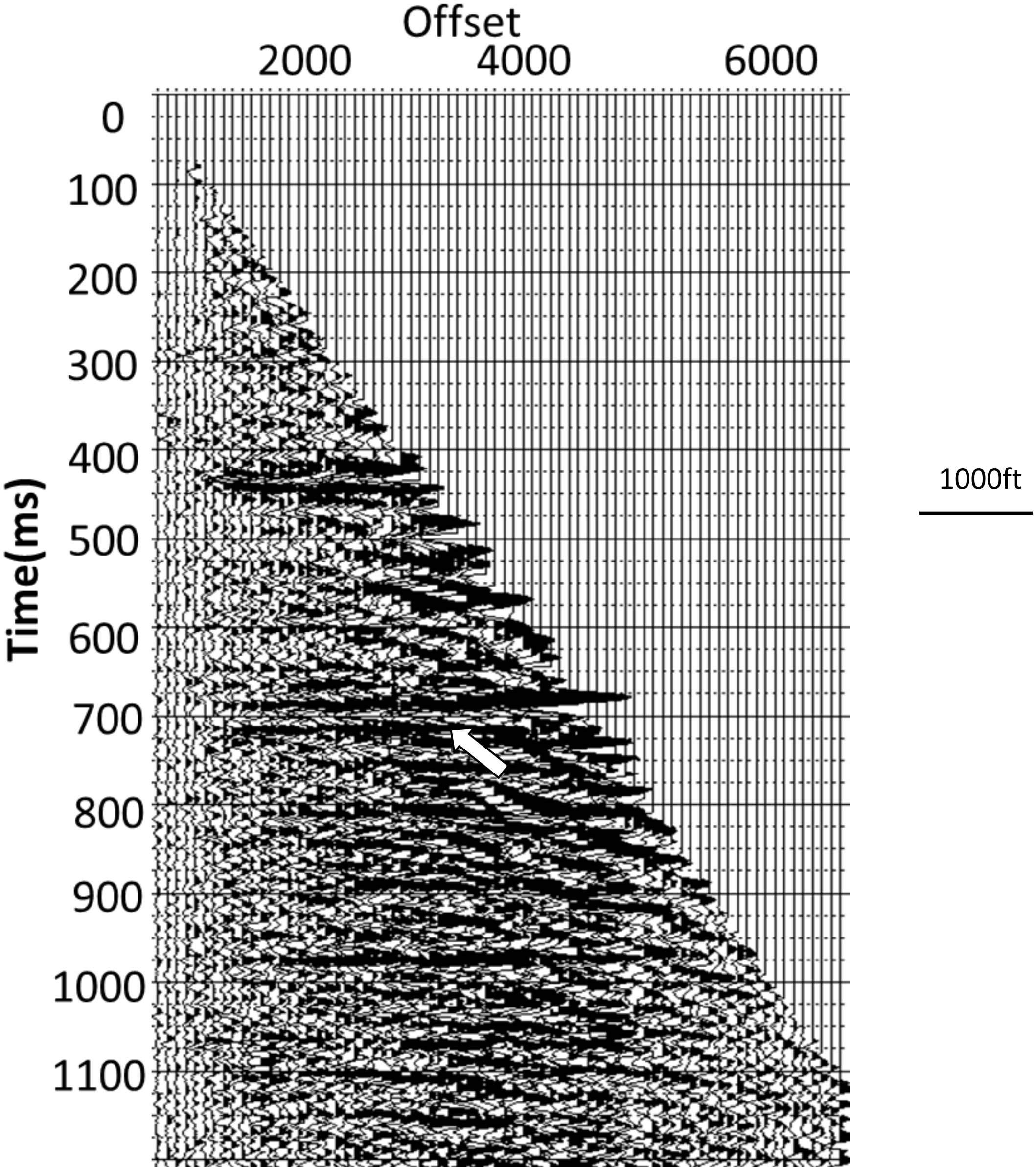

Figure 4.34. A representative conventionally migrated CRP gathers after three iterations of PLSM. The white block arrow indicates noise that has been attenuated using PLSM.

Chapter 5

PLSM of 3D data acquired over Osage County Field, Spyglass Co., Ok

5.1 Field introduction

The Mississippian chert is formed at the unconformity between the Pennsylvanian sandstone and Mississippian limestone in north-central Oklahoma and south-central Kansas. Rogers and Longman (2001) analysis of Mississippi chert core shows the chert have low density and high porosity, exhibiting vugs, nodules, and fractures with little remnant of the original depositional fabric. These properties make the Mississippian chert a good unconventional reservoir rock. The reservoir in Osage County has produced approximately 47 million barrels of oil and 40 Bcf (billion cubic feet**)** of gas within the study area over last decades.

Tectonic activity and subsequent erosion created a pre-Pennsylvanian unconformity along the Nemaha uplift, in parts of Kay, Osage, Pawnee, Noble, Garfield, and Grant counties in Oklahoma and northward into Kansas. The major unconformity separates Mississippian strata from overlying (Desmoinesian) Pennsylvanian deposits in this area. Whether deposited as detrital material or weathered-in-place, the material found at the unconformity is of Mississippian limestone origin and was reworked sometime between the mid-Mississippian and the Desmoinesian. The time interval provided opportunity for weathering, erosion, and redeposition at the unconformity (Rogers, 2001).

Yenugu used geometric attributes with impedance estimates to understand the distribution of fractures. Figure 5.1 shows major geologic provinces of Oklahoma.

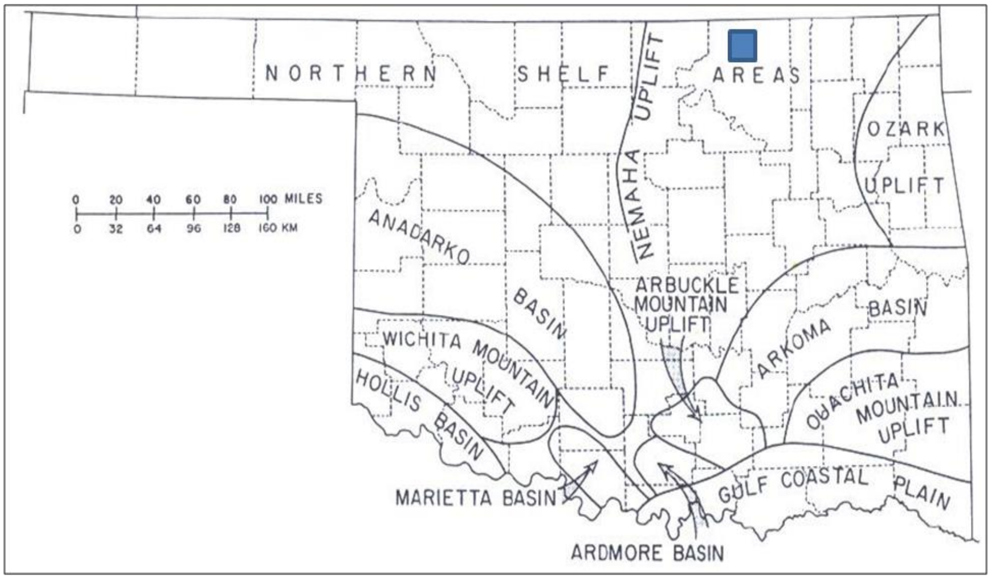

Figure 5.1. Major geologic provinces of Oklahoma. (After Yenugu, 2010).

The Mississippian chert was formed from Osagean (Mississippian) chert limestone during the exposure of those limestones at the unconformity as shown in Figure 5.2a. The chert is a diagenetically altered interval of Osagean cherty limestone that was uplifted, eroded, and weathered on and around the Nemaha uplift and the Cherokee platform in central Oklahoma. The rock unit is a weathered and detrital, highly porous chert, and serves as a significant hydrocarbon reservoir rock in north central Oklahoma in Figure 5.2b. Trapping mechanisms for hydrocarbons in the chert reservoirs are faults, structural closures, and porosity pinch outs caused by truncation and diagenesis on the flank of structural highs (Rogers, 2001).

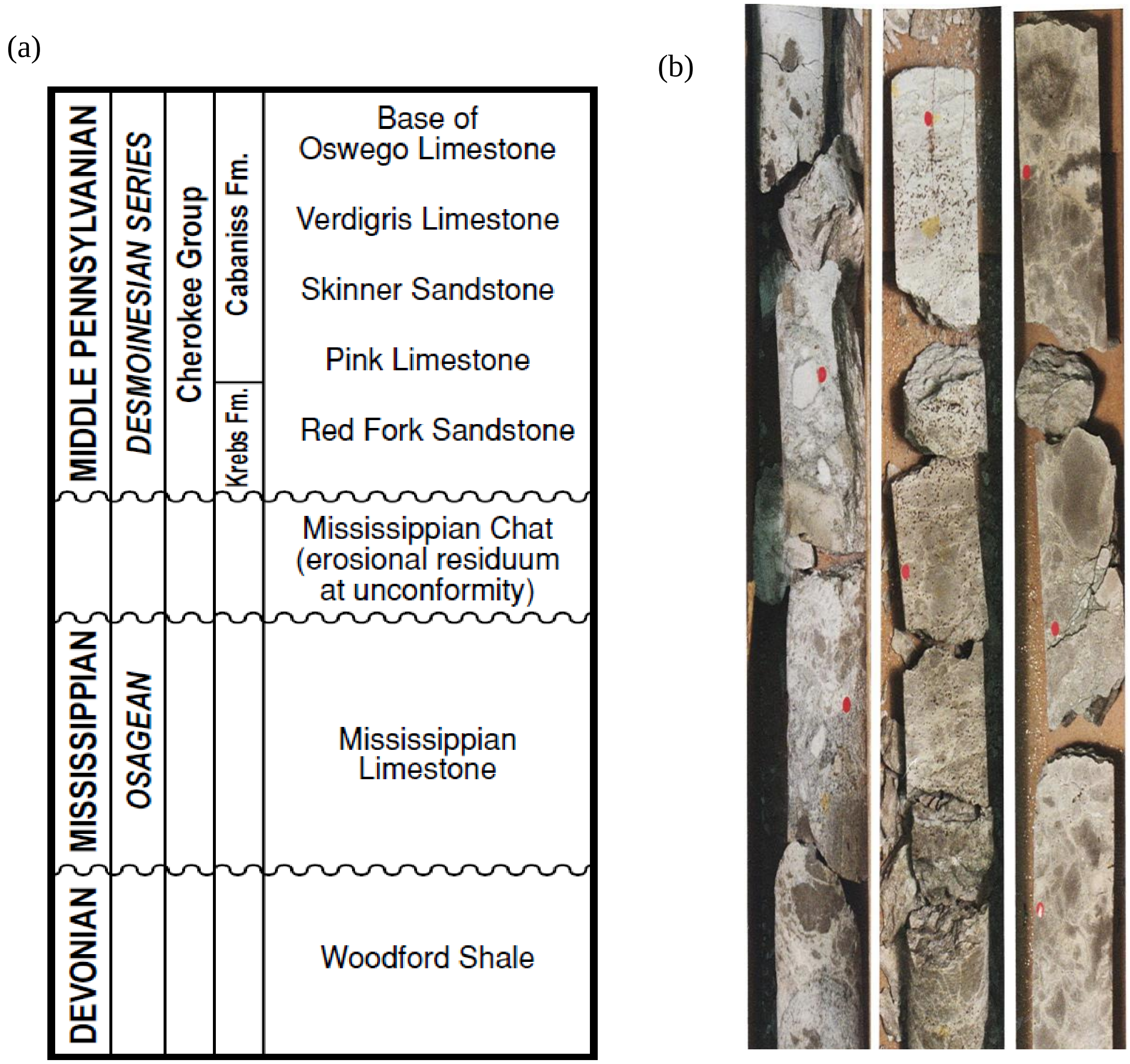

Figure 5.2. (a): Stratigraphic column of Osage County, Oklahoma. (b): Clasts of chert are visible as angular discolored forms in these typical core samples from the chert. Samples are from the middle of the zone and suggest small-scale debris flow textures. (After Rogers, 2001).

5.2 Results analysis and comparison

Figure 5.3a shows the time structure map on top of Mississippian Chert interpreted from the conventional migrated seismic data volume. White block arrows denote the fault lineaments. Figure 5.3b shows source receiver pair map. Vertical slices through seismic amplitude along profiles CC' are shown in Figures 5.3c. White block arrows indicate three structurally low features, because their lateral extent represents diagenetically altered fractures or faults. The green pick denotes the top of the Mississippian Chert.

Figure 5.4 shows a vertical slice through the stacked volume after conventional migration. Random noise and footprint obscures interpretation of subtle geological features. Figure 5.5 shows the stacked volume after two iterations of PLSM. Note the random noise is attenuated and geological features show up with higher illumination. After three iterations of PLSM (Figure 5.6), noise is further suppressed, which helps to better delineate the diagenetically-altered fractures.

Figure 5.7 shows time slice at t=0.6s through the stacked volume after conventional migration. The white block arrow indicates the footprint, which interferes with the reflection signal, and masks underlying geological features. After two and three iterations of PLSM (Figure 5.8 and 5.9), PLSM suppresses most of the footprint.

Figure 5.10a shows the common reflection point (CPR) prestack gathers from conventional migration. The noise as white block arrow shown can interfere the AVO gradient implement and elastic inversion. After the two iterations and three iterations after PLSM in Figure 5.10b and Figure 5.10c, these events show more continuation and less noise contamination, so the application of PLSM can make the AVO analysis and elastic inversion more accurate.

Figure 5.11 shows horizon slices along the Mississippian Chert through coherence volumes computed from conventional migration. High coherence zone highlights faults lineaments as white block arrows shown. Figure 5.12 and 5.13 shows the same two-attributes after two and three iterations of PLSM. Better illumination for fault lineaments occurs because of attenuation of random noise.

Figure 5.14 shows co-rendered horizon slices along the Mississippian Chert through coherence co-render with most negative curvature volume computed from conventional migration. Red block arrows highlight good correlation of high coherence and negative curvature in the fractures and faults zone. Figure 5.15 and 5.16 shows the same two-attributes after two and three iterations of PLSM. Higher correlation of high coherence and negative curvature provide better illumination for the faults and fracture zone and more geological lineaments begin show up. PLSM can give rise to more accurate interpretation and provide reliable guidance of drilling. Figure 5.17 shows the vertical slice through CC' of same attributes volume computed three iterations of PLSM, note the high correlation zone as the red block arrows shown.

Figure 5.18 shows co-rendered horizon slices along the Mississippian Chert through coherence co-rendered with RMS amplitude volume computed from three iterations of PLSM. Note the faults and fracture zone is highlighted by high coherence and relatively high RMS amplitude. There is high correlation between these two attributes, which is consistent with the previous multi-attribute interpretation shown in Figure 5.16.

Figure 5.19 shows co-rendered horizon slices along the Mississippian Chert through coherence co-rendered with inline gradient volume computed from three iterations of

PLSM. Gradient energy gradient is a robust tool for delineating fault as it denotes the derivative of the coherent energy. Note the high correlation between relatively high coherent energy and gradient low in fracture and faults zone.

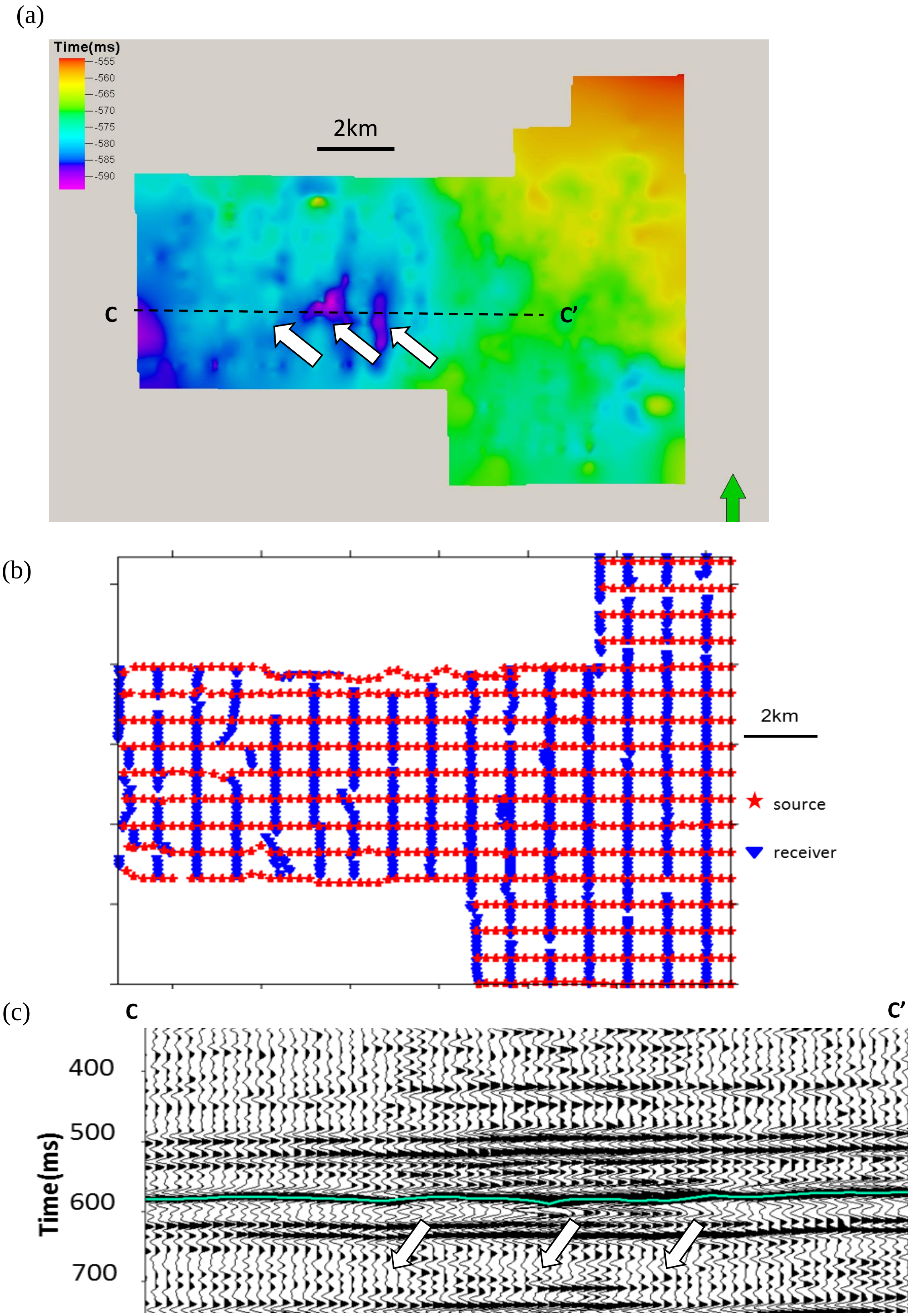

Figure 5.3. (a) is the Time-structure map of the top of Mississippian Chert horizon, (b) source receiver pair map. (c) Stacked volume through seismic amplitude along profiles CC’, white block arrows show collapsed features.

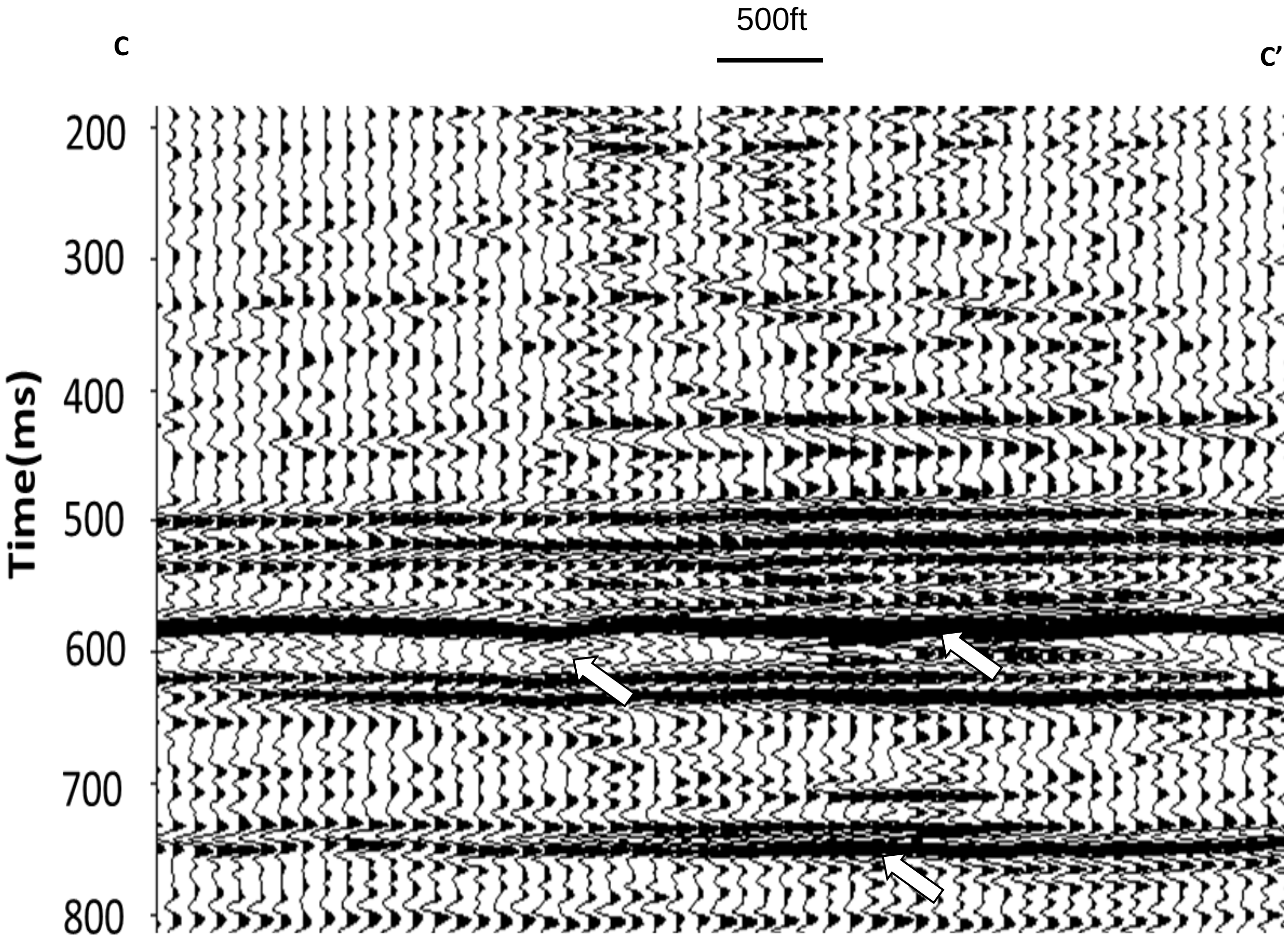

Figure 5.4. Stacked volume through seismic amplitude along profile CC' as shown in Figure5.3 ausing conventional migration, white block arrows show diagenetically altered fractures or faults.

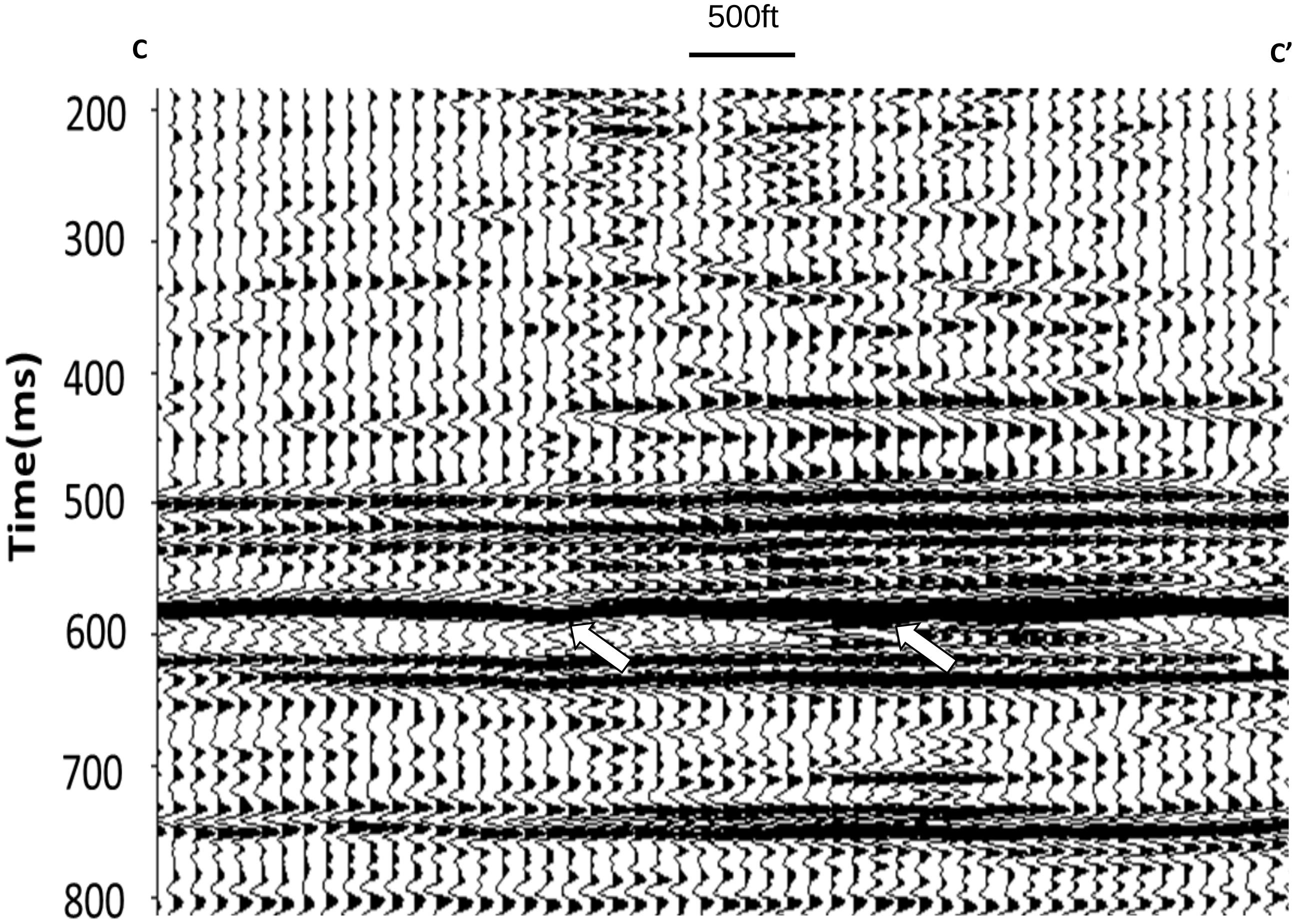

Figure 5.5. Stacked volume through seismic amplitude along profile CC’ as shown in Figure5.3a after two iterations of PLSM, white block arrows show diagenetically altered fractures or faults.

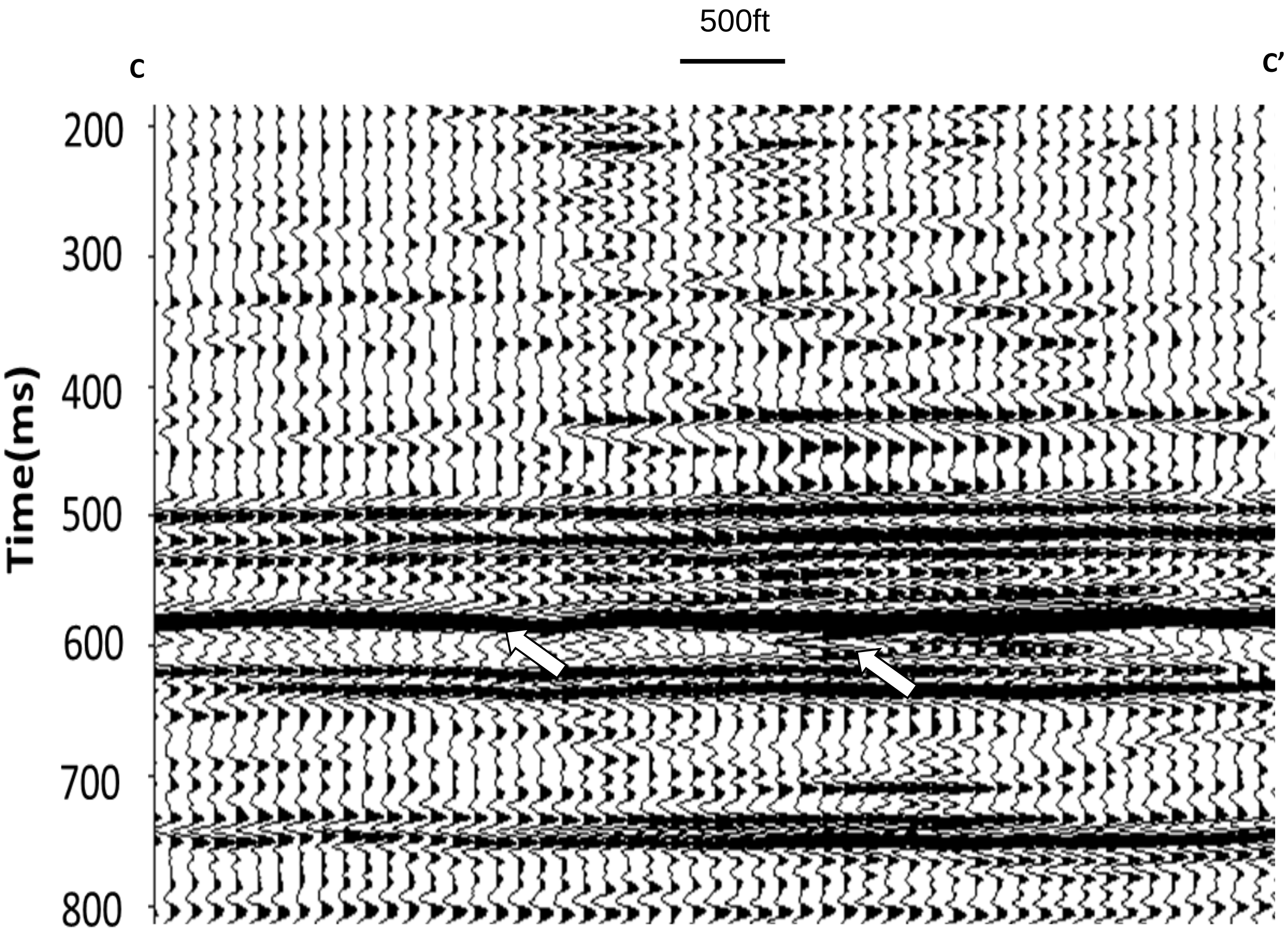

Figure 5.6. Stacked volume through seismic amplitude along profile CC' as shown in Figure5.3a after three iterations of PLSM, white block arrows show diagenetically altered fractures or faults.

Figure 5.7. Time slice at *t*=0.6 s through stacked amplitude volumes conventional migration. The white block arrow indicates the footprint, which impedes the interpretation

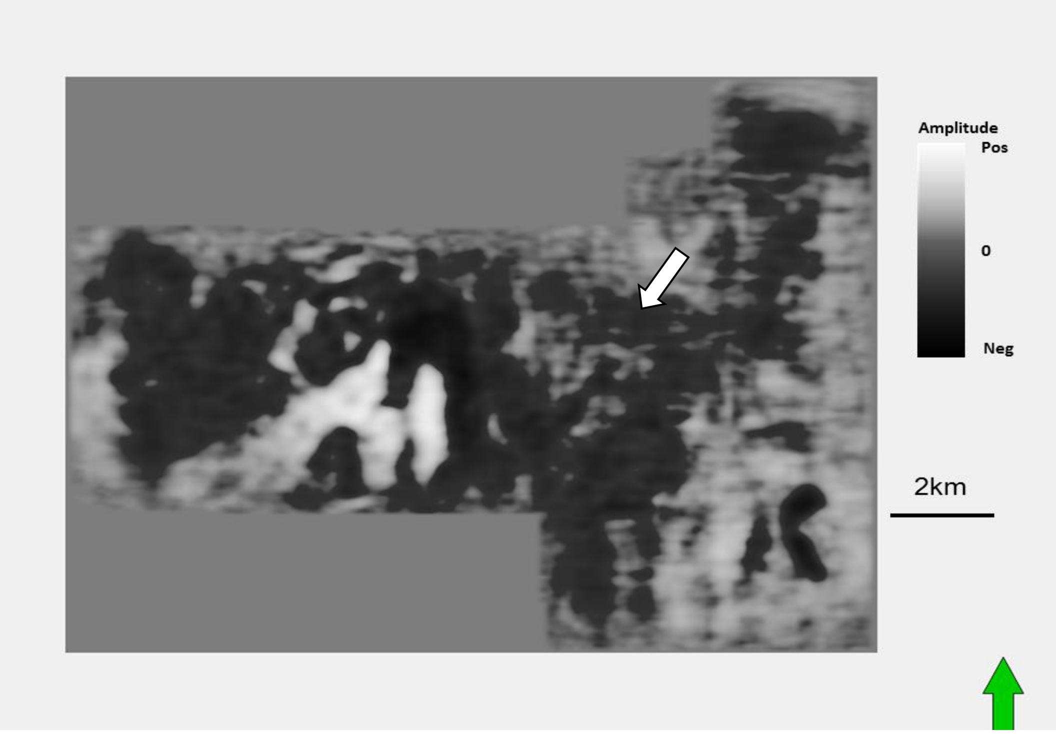

Figure 5.8. Time slice at *t*=0.6 s through stacked amplitude after two iterations of PLSM. The white block arrow indicates area where the footprint is attenuated.

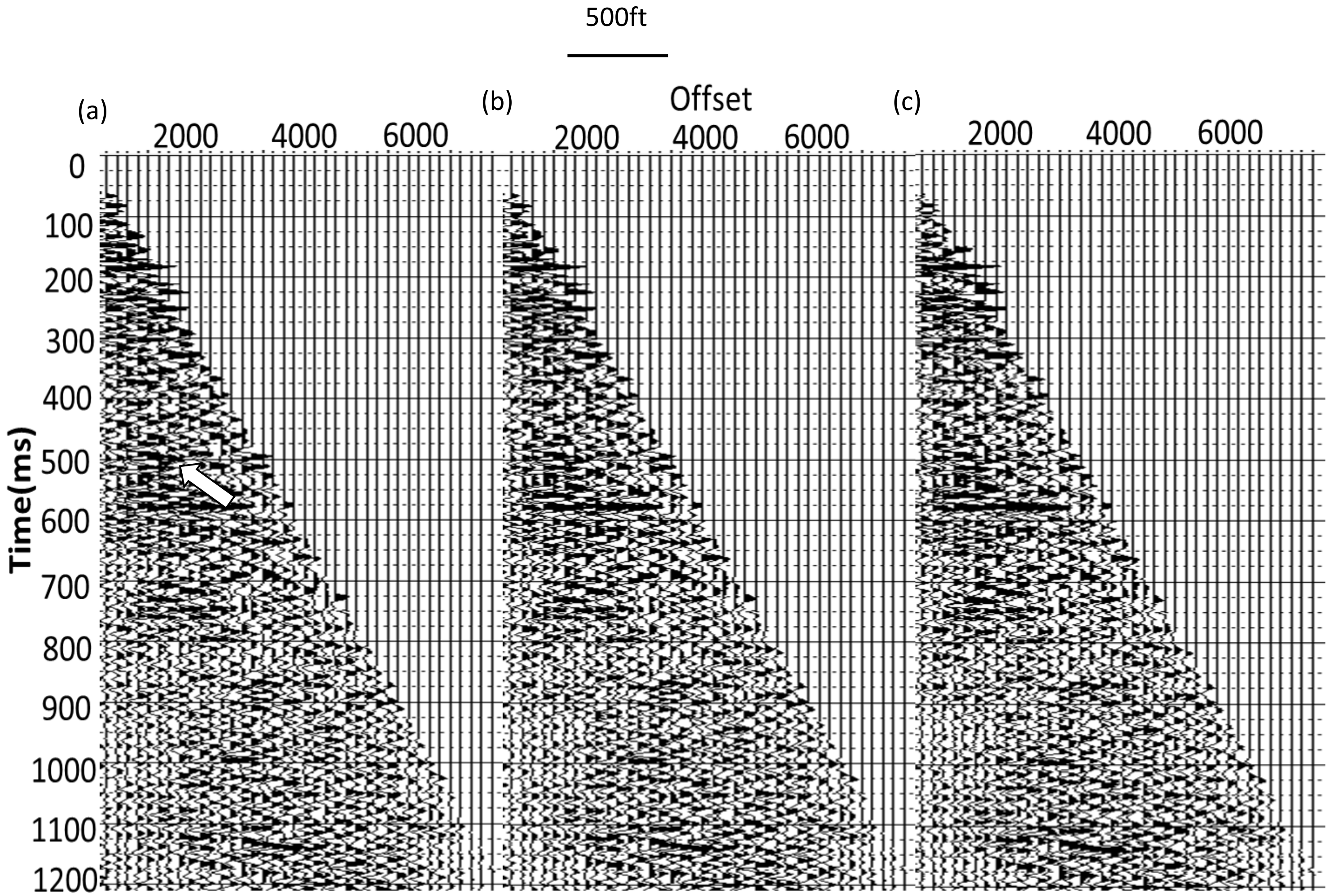

Figure 5.10. A representative conventionally migrated CRP gathers after (a) conventional migration and after (b) two, and (c) three iterations of PLSM. The white block arrow indicates noise that has been attenuated using PLSM..

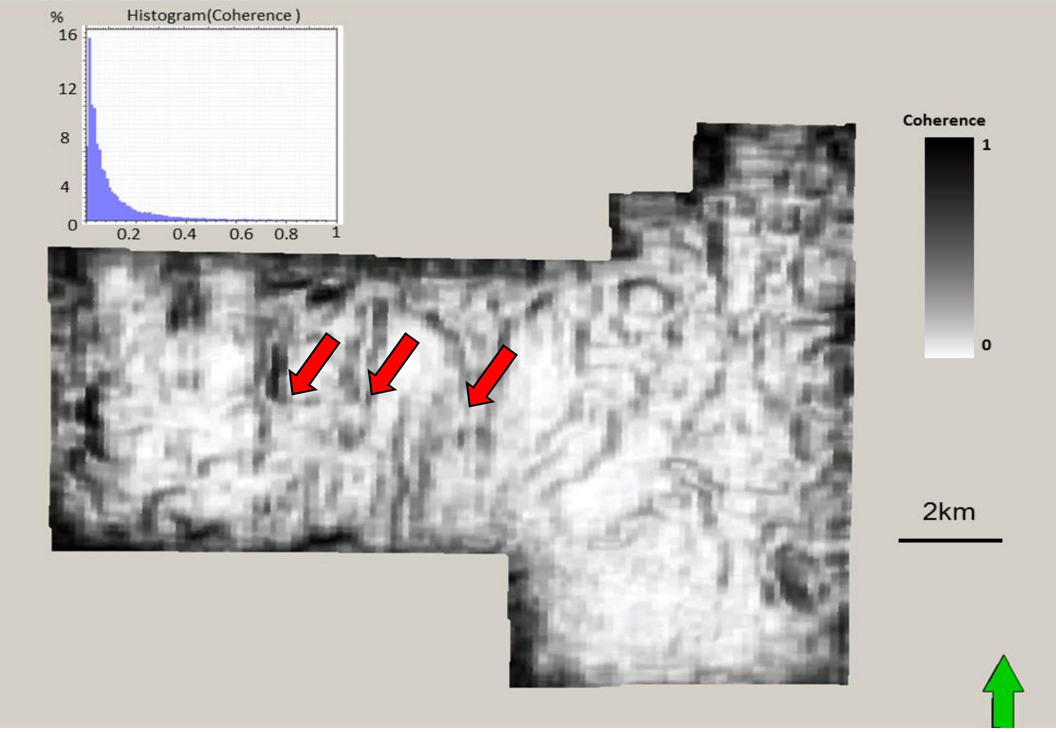

Figure 5.11. Horizon slices along the Mississippian Chert through coherence volumes computed from seismic amplitude using conventional migration. Red block arrows in indicate fractures lineaments.

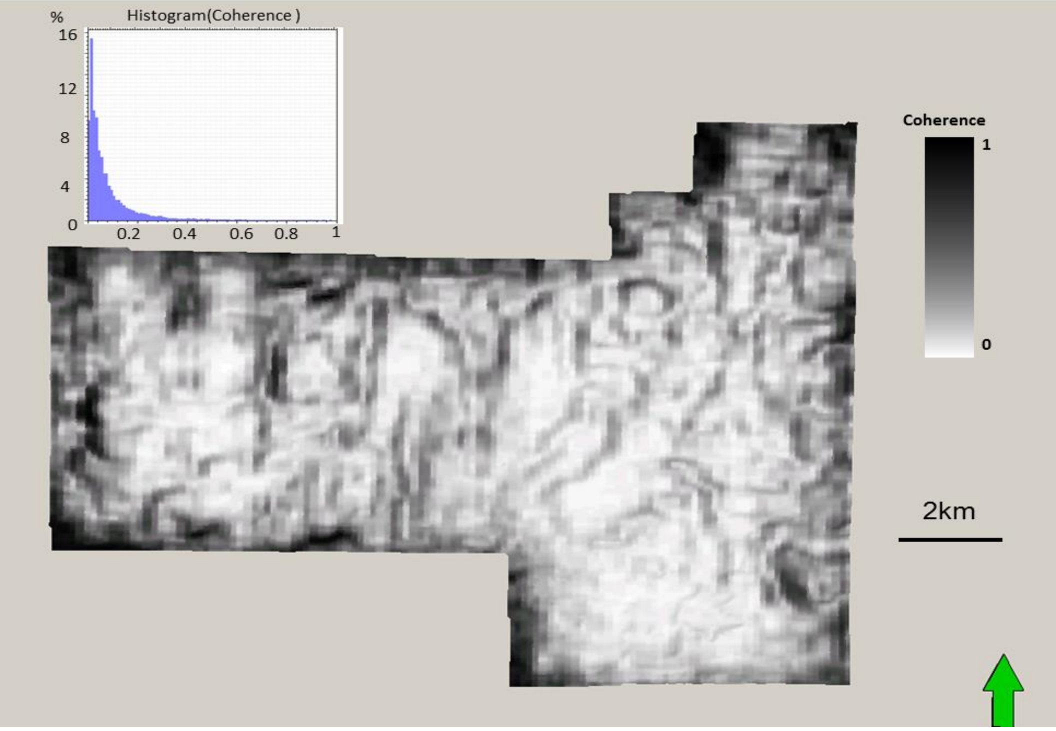

Figure 5.12. Horizon slices along the Mississippian Chert through coherence volumes computed from seismic amplitude after two iterations of PLSM. Red block arrows in indicate fractures lineaments.

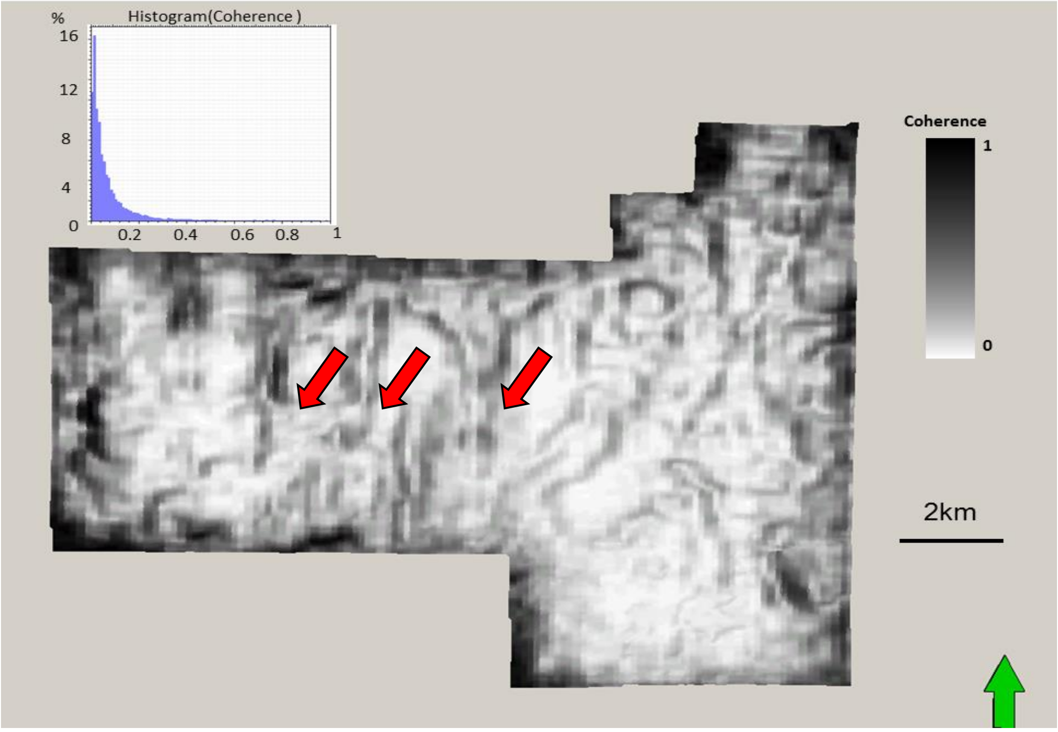

Figure 5.13. Horizon slices along the Mississippian Chert through coherence volumes computed from seismic amplitude after three iterations of PLSM. Red block arrows in indicate fractures lineaments.

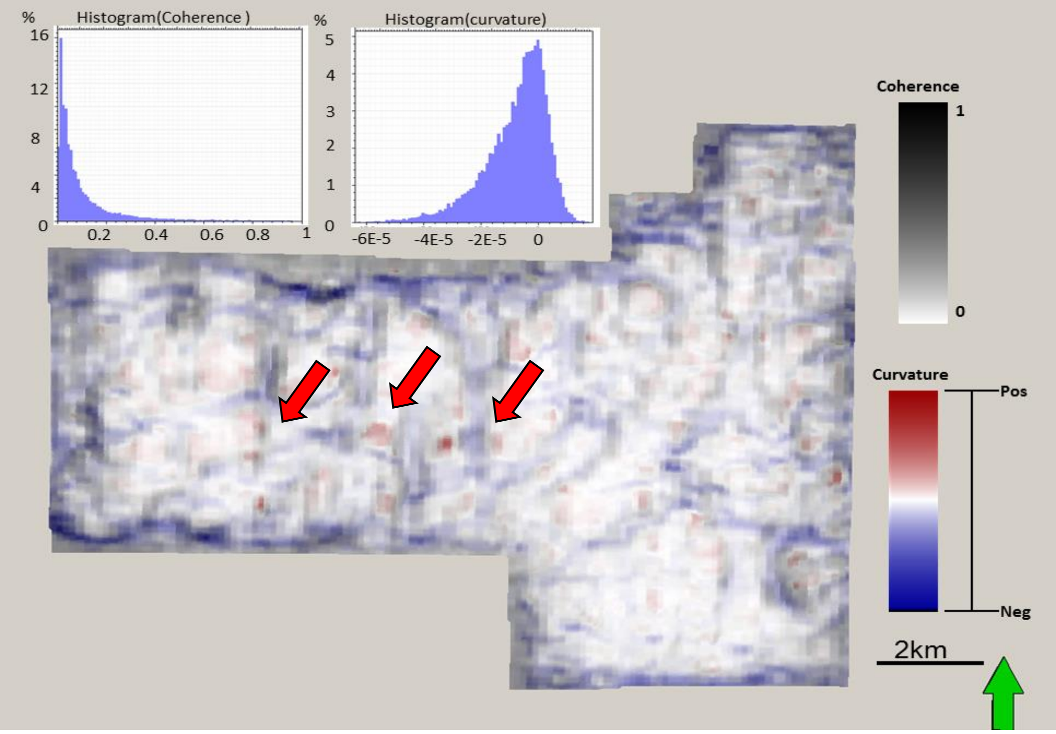

Figure 5.14. Horizon slices along the Mississippian Chert through coherence co-rendered with most negative curvature volumes computed from conventional migration. Red block arrows in indicate the fractures lineament.

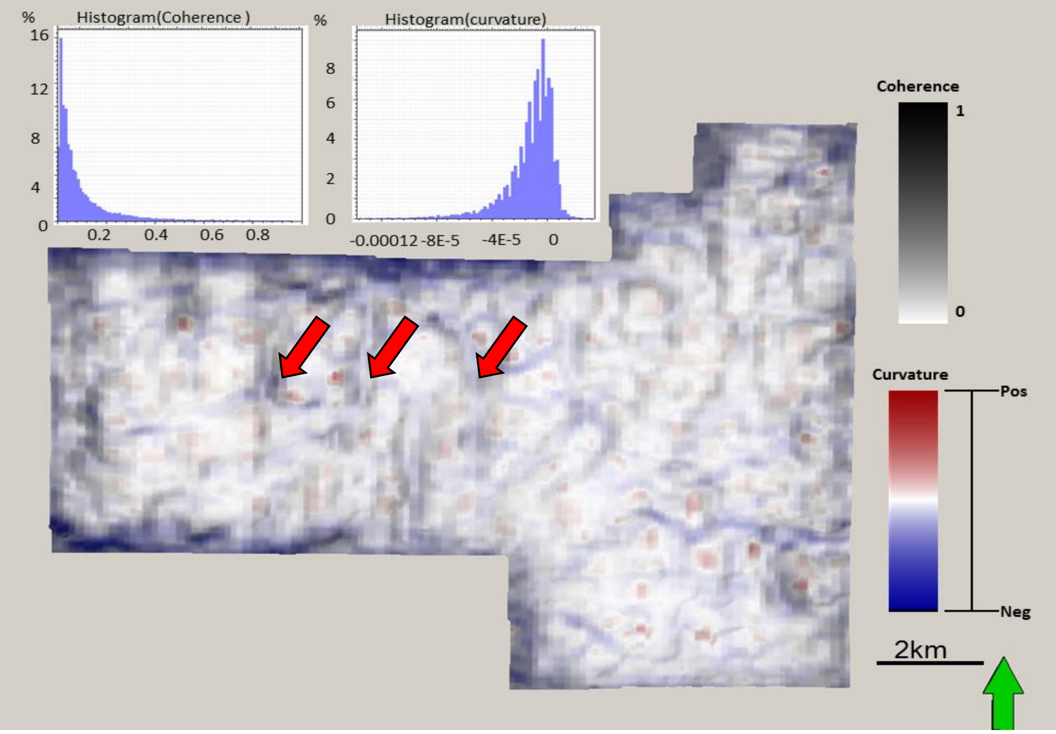

Figure 5.15. Horizon slices along the Mississippian Chert through coherence co-rendered with most negative curvature volumes computed from two iterations of PLSM . Red block arrows in indicate the fractures lineament.

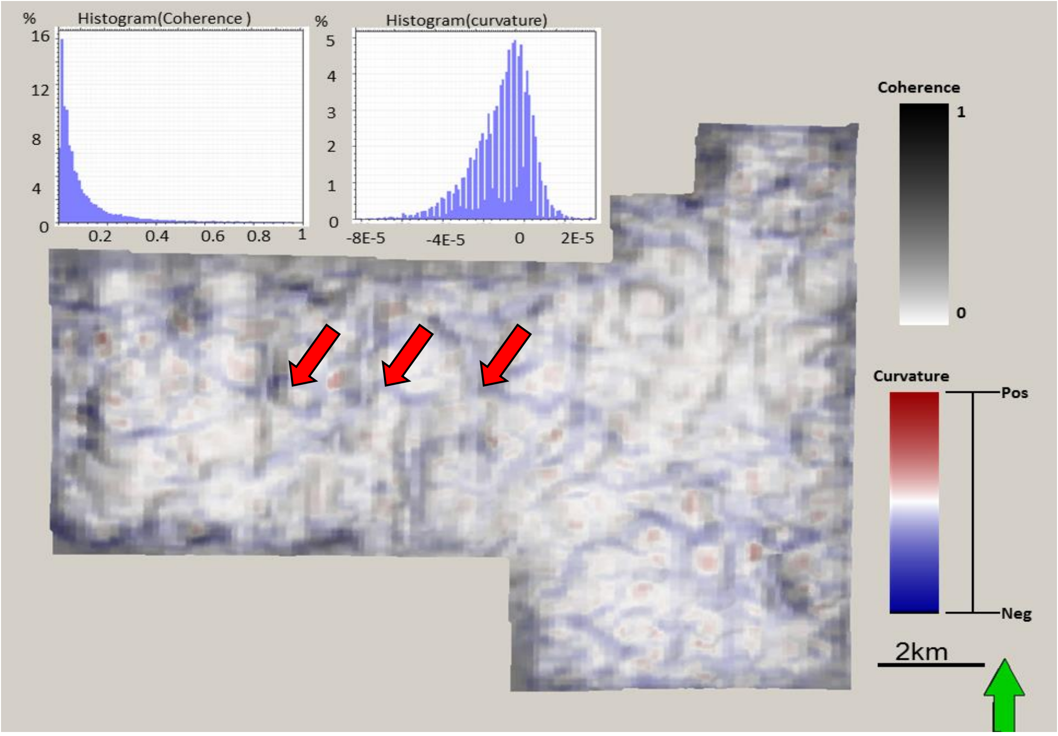

Figure 5.16. Horizon slices along the Mississippian Chert through coherence co-rendered with most negative curvature volumes computed from three iterations of PLSM. . Red block arrows in indicate the fractures lineament.

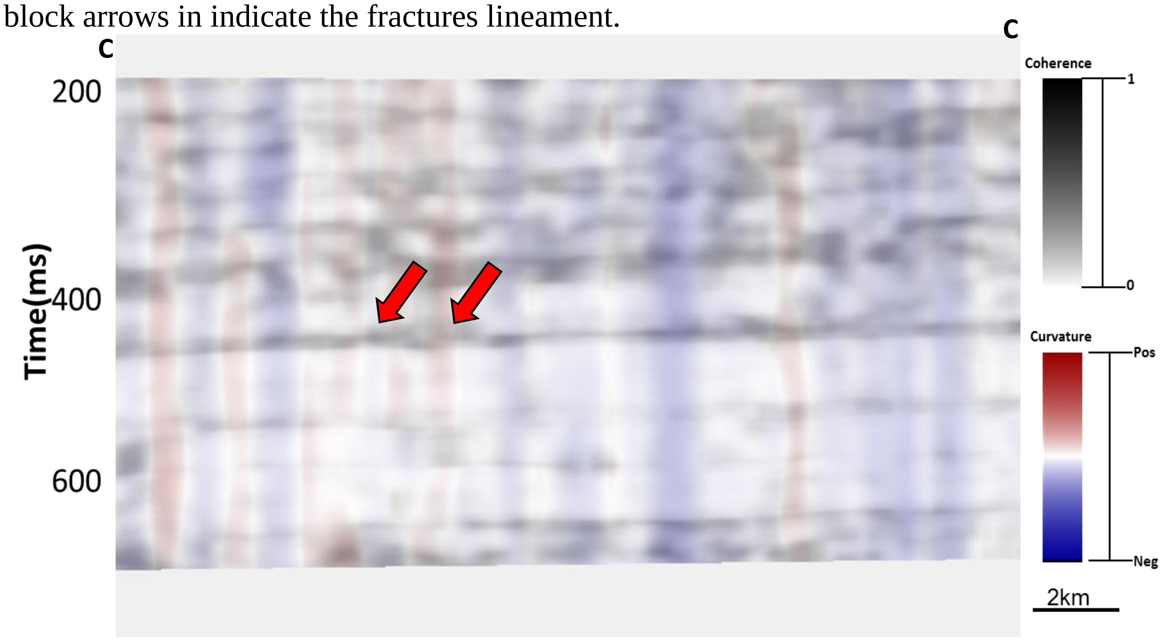

Figure 5.17. Vertical slice through CC' of same attributes after three iterations of PLSM. Red block arrows in indicate the fractures lineament. After PLSM is applied, there is higher correlation between the most negative curvature and low coherence.

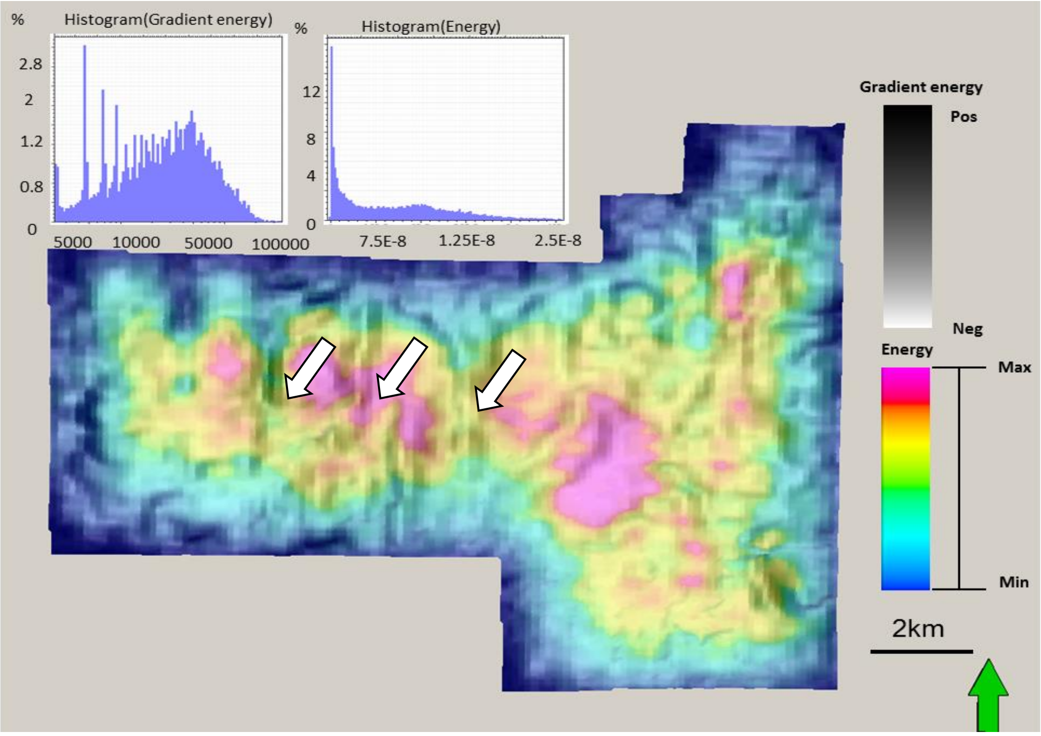

Figure 5.18. Horizon slices along the Mississippian Chert through coherence co-rendered with RMS amplitude volumes computed from seismic amplitude after three iterations of PLSM.

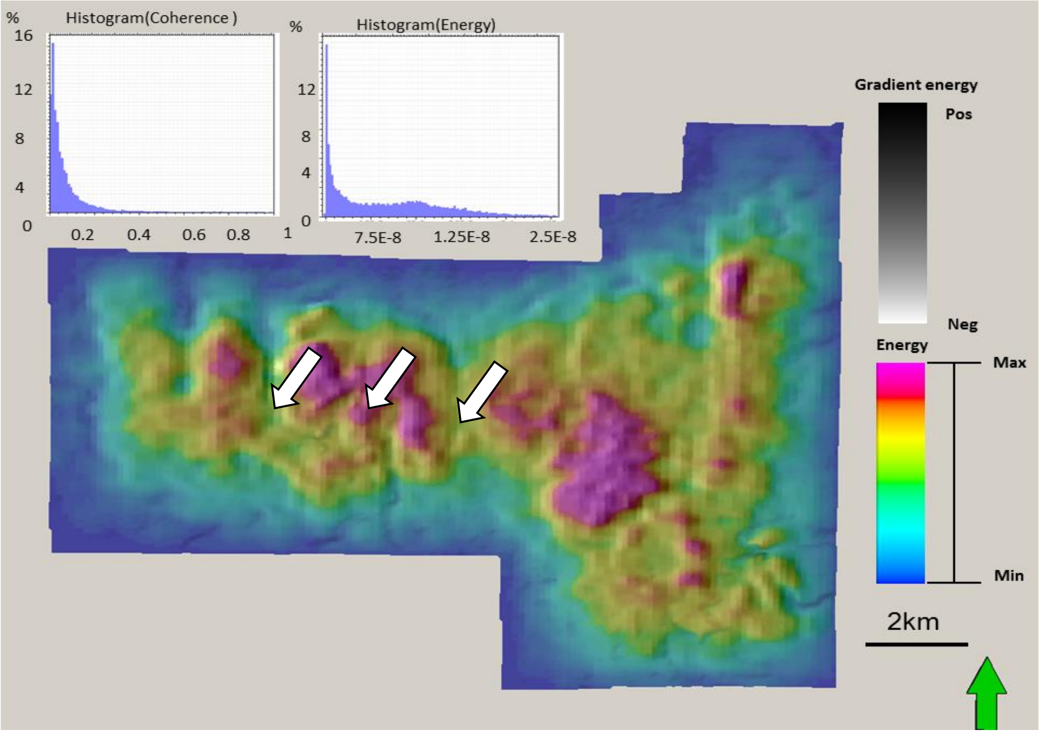

Figure 5.19. Horizon slices along the Mississippian Chert through inline gradient co-rendered with RMS amplitude volumes computed from seismic amplitude after three iterations of PLSM.

Chapter 6

Discussion and conclusion

PLSM worked effectively for removing aliasing artifacts arise from decimated Dickman survey from west Kansas. By comparing with the residual convergence rate of LSM, the structure-oriented median filter served as constraint in PLSM.

Application of PLSM to the undecimated Dickman dataset from west Kansas showed rapid improvement of signal-to-noise ratio for CRP gathers and significant attenuation of footprint and random noise, which impeded interpretation from conventional migration. Moreover, PLSM brought significant improvement for seismic attributes illumination. PLSM made multiple attributes better illuminate karst collapse features on Gilmore City horizon. In addition, PLSM worked well for eliminating the random noise in prestack gathers, and the outcome of constrained least-squares migration better represents the seismic amplitudes of earth reflectivity. At last, PLSM allowed better prediction of the original gathers while enhance coherent events.

Finally, I applied PLSM on the Osage County dataset. PLSM also showed it could be robust tool for random noise reduction and footprint elimination. PLSM allowed better attributes illumination for fractures lineaments on top of Mississippian Chert.

In the future, I would apply the PLSM on diffraction images. Because it provides a means that can accurately demigrate the subsurface data, PLSM images can be filtered to demigrate the specular reflection component of the surface-recorded data, leaving the diffractions (and residual noise) for subsequent diffraction imaging.

Admittedly, the PLSM is computer time intensive, as it is needed to run for several iterations. Although I applied constraints and MPI in the program, it still takes a lot of computing resource when it comes to bigger dataset. Perhaps for my next step I will work a little more on the efficiency of transferring data on the MPI for prestack time migration.

References

Aoki, N., and G. Schuster, 2009, Fast least-squares migration with a deblurring filter: Geophysics, **74**, WCA83-WCA93.

Biondi, B., 2001, Kirchhoff imaging beyond aliasing: Geophysics, **66**, 654-666.

Biondi, B., 2006, 3D seismic imaging: Society of Exploration Geophysicists, 27-29.

Cabrales Vargas, A., 2011, Suppression of aliasing artifacts on 3D land data via constrained least-squares migration: M.Sc. thesis, Univ. of Oklahoma.

Chavent, G. and R.- E. Plessix, 1996, A time-domain derivation of optimal and suboptimal Kirchhoff quantitative migrations via a least-squares approach. National Institute for Research in Computer Science and Control, 3-38

Claerbout, J. F., 1992, Earth soundings analysis: Processing versus inversion: Blackwell Scientific, 144-145.

Corrao, A., M. Fervari, and M. Galbiati, 2011, Hewett Plattendolomite: Reservoir Characterization by Resolution Enhanced Seismic data: GCSSEPM.

Davogustto-Cataldo, O., 2011, Removing footprint from legacy seismic data volumes: M.Sc. Thesis, University of Oklahoma.

Fehmers, G., and F. W. Höecker, Fast structural interpretation with structure-oriented filtering: Geophysics, **68**, 1286-1293.

Falconer, S., and K. J. Marfurt, 2008, Attribute-driven footprint suppression: SEG Expanded Abstracts, **27**, 2667-2671.

Jovanovic, K., 2004, P and SV polarization filtering of a multicomponent vector VSP: M.S. thesis, Univ. of Houston.

Kwiatkowski, J. T. and K. J. Marfurt, 2011, Data conditioning of Legacy pre-stack time migrated gathers from the Mid-Continent: 2011 AAPG Mid-Continent Section Meeting.

Kuwahara, M., K. Hachimura, S. Eiho, and M. Kinoshita, 1976, Digital processing of biomedical images: Plenum Press, 187–203.

Luo, Y., S. al-Dossary, and M. Marhoon, 2002, Edge-preserving smoothing and applications: The Leading Edge, **21**, 136–158.

Nemeth, T., 1996, Imaging and filtering by least-squares migration: Ph. D. dissertation, Univ. of Utah.

Nemeth, T., C. Wu, and G. Schuster, 1999, Least-squares migration of incomplete reflection data: Geophysics, **64**, 208-221.

Nissen S.E., T.R. Carr, K.J. Marfurt, and E. C. Sullivan, 2009, Using 3-D seismic volumetric curvature attributes to identify fracture trends in a depleted Mississippian carbonate reservoir: Implications for assessing candidates for CO2 sequestration: AAPG Studies in Geology, **59**, 297–319.

Perez, G., and K. J. Marfurt, 2008, New azimuthal binning for improved delineation of faults and fractures: Geophysics, **73**, S7–S15.

Rogers, J. P., and Mark W. Longman, 2001, An introduction to chert reservoirs of North America, AAPG Bulletin, **85**, No.1, 1-5.

Rogers, S. M., 2001, Deposition and diagenesis of Mississippian chat reservoirs, north-central Oklahoma, , AAPG Bulletin, **85**, No.1, 115-129.

Schuster, G. T., 1993, Least-squares crosswell migration: 64th International Exposition and Annual Meeting, Expanded Abstract, 110-113.

Schuster, G. T., 1997, Acquisition footprint removal by least-squares migration: 1997 Annual UTAM Report, 73-99.

Wang, J., and M. Sacchi, 2009, Structure constrained least-squares migration: SEG 2009 International Exposition and Annual Meeting, 2763-2767.

Wei, D., and Schuster, G. T., 2011, Least-squares migration of multisource data with a deblurring filter: Geophysics, **76**, 135-146.

Yenugu, M., Angelo, M., and K.J. Marfurt, 2010, Seismic attribute analysis of a Mississippian Chat, Osage County, Northeast Oklahoma: 2010 AAPG Annual Convention & Exhibition, New Orleans.

Zhang, Y., M. Karazincir, C. Notfors, J. Sun, and B. Hung, 2002, Amplitude preserving v(z) prestack Kirchhoff migration, demigration and modeling: 64th EAGE Annual Conference, 27-30.